

*AB INITIO* CALCULATIONS OF MECHANICAL, THERMODYNAMIC AND  
ELECTRONIC STRUCTURE PROPERTIES OF MULLITE,  
IOTA-ALUMINA AND BORON CARBIDE

A DISSERTATION IN  
Physics  
and  
Geosciences

Presented to the Faculty of the University  
of Missouri-Kansas City in partial fulfillment of  
the requirements for the degree

DOCTOR OF PHILOSOPHY

by  
SITA RAM ARYAL

M.Sc, Tribhuban University, Kathmandu, Nepal, 1996  
M.S., University of Missouri - Kansas City, 2008

Kansas City, Missouri  
2012

© 2012

SITA RAM ARYAL

ALL RIGHTS RESERVED

*AB INITIO* CALCULATIONS OF MECHANICAL, THERMODYNAMIC AND  
ELECTRONIC STRUCTURE PROPERTIES OF MULLITE,  
IOTA-ALUMINA AND BORON CARBIDE

Sita Ram Aryal, Candidate for the Doctor of Philosophy Degree  
University of Missouri-Kansas City, 2012

ABSTRACT

The alumino-silicate solid solution series ( $Al_{4+2x}Si_{2-2x}O_{10-x}$ ) is an important class of ceramics. Except for the end member ( $x=0$ ),  $Al_2SiO_5$  the crystal structures of the other phases, called mullite, have partially occupied sites. Stoichiometric supercell models for the four mullite phases  $3Al_2O_3 \bullet 2SiO_2$ ,  $2Al_2O_3 \bullet SiO_2$ ,  $4Al_2O_3 \bullet SiO_2$ ,  $9Al_2O_3 \bullet SiO_2$ , and  $\iota-Al_2O_3$  (iota-alumina) are constructed starting from experimentally reported crystal structures. A large number of models were built for each phase and relaxed using the Vienna *ab initio* simulation package (VASP) program. The model with the lowest total energy for a given  $x$  was chosen as the representative structure for that phase. Electronic structure and mechanical properties of mullite phases were studied via first-principles calculations.

Of the various phases of transition alumina,  $\iota-Al_2O_3$  is the least well known. In addition structural details have not, until now, been available. It is the end member of the aluminosilicate solid solution series with  $x=1$ . Based on a high alumina content mullite phase, a structural model for  $\iota-Al_2O_3$  is constructed. The simulated x-ray diffraction (XRD) pattern of this model agrees well with a measured XRD pattern. The  $\iota-Al_2O_3$

is a highly disordered ultra-low-density phase of alumina with a theoretical density of  $2854 \text{ kg/m}^3$ . Using this theoretically constructed model, elastic, thermodynamic, electronic, and spectroscopic properties of  $\iota\text{-Al}_2\text{O}_3$  have been calculated and compared it with those of  $\alpha\text{-Al}_2\text{O}_3$  and  $\gamma\text{-Al}_2\text{O}_3$ .

Boron carbide ( $B_4C$ ) undergoes an amorphization under high velocity impacts. The mechanism of amorphization is not clear. *Ab initio* methods are used to carry out large-scale uniaxial compression simulations on two polytypes of stoichiometric boron carbide ( $B_4C$ ),  $B_{11}C\text{-CBC}$ , and  $B_{12}\text{-CCC}$  where  $B_{11}C$  or  $B_{12}$  is the 12-atom icosahedron and  $CBC$  or  $CCC$  is the three-atom chain. The simulations were performed on large supercells of 180 atoms. Simulated results indicate bending of the three-atom chain leads to the amorphization of the  $B_{11}C\text{-CBC}(B_{12}\text{-CCC})$  at a uniaxial strain  $s=0.23$  (0.22) and with a maximum stress of 168 (151) GPa. The mechanism of amorphization is analyzed with radial pair distribution function (RPDF), total density of states (TDOS), and the distribution of effective charges on atoms.

## APPROVAL PAGE

The faculty listed below, appointed by the Dean of the School of Graduate Studies have examined a dissertation titled “*Ab Initio* Calculations of Mechanical, Thermodynamic and Electronic Structure Properties of Mullite, Iota-alumina and Boron Carbide,” presented by Sita Ram Aryal, candidate for the Doctor of Philosophy degree, and certify that in their opinion it is worthy of acceptance.

### Supervisory Committee

Wai-Yim Ching, Ph.D., Committee Chair  
Department of Physics

Michael Kruger, Ph.D.  
Department of Physics

Jerzy Wrobel, Ph.D.  
Department of Physics

Raymond M. Coveney Jr., Ph.D.  
Department of Geosciences

Jejung Lee, Ph.D.  
Department of Geosciences

## CONTENTS

ABSTRACT . . . . .	ii
LIST OF ILLUSTRATIONS . . . . .	viii
LIST OF TABLES . . . . .	xiii
ACKNOWLEDGMENTS . . . . .	xiv
Chapter	
1. INTRODUCTION . . . . .	1
2. THEORETICAL BACKGROUND . . . . .	6
3. SIMULATION PACKAGES AND METHODS USED . . . . .	14
3.1. Vienna <i>ab initio</i> Simulation Package (VASP) . . . . .	14
3.2. Orthogonalized Linear Combination of Atomic Orbitals (OLCAO) . . . . .	17
3.3. Elastic and Mechanical Properties Calculations . . . . .	25
3.4. Phonon and Thermodynamic Properties Calculations . . . . .	27
4. MECHANICAL AND ELECTRONIC STRUCTURE PROPERTIES OF MULLITE . . . . .	33
4.1. Introduction . . . . .	33
4.2. Structural Modeling of the Mullite Phases . . . . .	36
4.2.1. Construction of Supercell Models . . . . .	36
4.2.2. Analysis of Mullite Models . . . . .	40
4.3. Mechanical Properties of the Mullite Phases . . . . .	45
4.3.1. Elastic Stiffness Constants and Bulk Mechanical Properties . . . . .	45
4.3.2. Sound Velocity in Different Planes . . . . .	52
4.4. Electronic Structure of Mullite Phases . . . . .	56

4.4.1.	Band Structure and Density of States . . . . .	56
4.4.2.	Effective Charges and Bond Orders . . . . .	59
4.4.3.	Optical Properties of Mullite . . . . .	63
4.5.	Summary and Conclusions . . . . .	67
5.	STRUCTURE AND PROPERTIES OF IOTA-ALUMINA ( $\iota$ - $Al_2O_3$ ) . . . . .	70
5.1.	Introduction . . . . .	70
5.2.	Structural Modeling of $\iota$ - $Al_2O_3$ . . . . .	72
5.2.1.	Construction of Model . . . . .	72
5.2.2.	Structural Analysis . . . . .	74
5.2.3.	X-ray Diffraction Pattern . . . . .	78
5.3.	Results and Discussions . . . . .	79
5.3.1.	Total Energy and Density . . . . .	79
5.3.2.	Elastic Properties . . . . .	81
5.3.3.	Phonon Dispersion . . . . .	82
5.3.4.	Thermodynamic Properties . . . . .	85
5.3.5.	Electronic Structure . . . . .	87
5.3.6.	Effective Charge . . . . .	91
5.3.7.	Optical Properties . . . . .	93
5.3.8.	XANES/ELNES Spectra . . . . .	94
5.4.	Summary and Conclusions . . . . .	99
6.	AMORPHISATION OF BORON CARBIDE ( $B_4C$ ) . . . . .	102
6.1.	Introduction . . . . .	102
6.2.	Methods and Procedures of Simulations . . . . .	106
6.3.	Results and Discussion . . . . .	110
6.3.1.	Results on Hydrostatic Compression . . . . .	110

6.3.2. Results on Uniaxial Compression . . . . .	110
6.3.3. Strain-Dependent Elastic Coefficients . . . . .	114
6.3.4. Structural Analysis of Supercell Models . . . . .	117
6.3.5. Evidence of Amorphization: Radial Pair Distribution . . . . .	121
6.3.6. Evidence of Amorphization: Electronic Structure . . . . .	124
6.3.7. Summary and Conclusions . . . . .	133
7. FUTURE WORKS . . . . .	136
APPENDIX . . . . .	139
BIBLIOGRAPHY . . . . .	143
VITA . . . . .	158

## ILLUSTRATIONS

Figure	Page
1. Relaxed supercell models of mullite phases including sillimanite and $\iota$ - $Al_2O_3$ . . . . .	39
2. Radial pair distribution function (RPDF) of Al-O, Al-Al, O-O, Si-O, Si-Si, and Al-Si pairs in mullite phases including sillimanite and iota-alumina. All the RPDF values are normalised to same area . . . . .	41
3. Variation of lattice constants (a) and volume (b) with x in the mullite series. Lines joining data points illustrate the general trend with x. . . . .	45
4. Calculated elastic constants of mullite phases in GPa. Scattered symbols represent $C_{ij}$ data for a particular phase and lines joining them show a general trend. . . . .	46
5. Calculated mechanical bulk properties of mullite phases in GPa . . . . .	49
6. Calculated Poisson's ratios of mullite phases. . . . .	50
7. Calculated sound velocities (m/s) in 3/2 mullite in: (a) (001) plane; (b) (100) plane; (c) (010) plane. . . . .	54
8. Calculated maximum and minimum sound velocity (m/s) in mullite phases in: (a) (001) plane; (b) (100) plane; and (c) (010) plane. T for the transverse modes and L for the longitudinal mode. . . . .	55
9. Calculated band structures of mullite along the high symmetry points in the Brillouin zone: (a) Sillimanite; (b) 3/2 mullite; (c) 2/1 mullite; (d) 4/1 mullite; (e) 9/1 mullite; (f) $\iota$ - $Al_2O_3$ . . . . .	57

10. Variation of calculated band gap (eV) with x in the mullite phases including sillimanite and $\iota$ - $Al_2O_3$ . . . . .	58
11. Calculated total density of states (TDOS) of mullite phases. The vertical line represents the top of valance band set at 0.0 eV. . . . .	60
12. Average effective charge $Q^*$ distribution in mullite phases. . . . .	61
13. Variation of the bond order density in mullite phases with x. . . . .	62
14. Calculated real and imaginary parts of the dielectric functions. . . . .	64
15. Variation of calculated refractive index n with x in the mullite phases including sillimanite and $\iota$ - $Al_2O_3$ . . . . .	66
16. Relaxed supercell model of $\iota$ - $Al_2O_3$ . . . . .	75
17. Radial pair distributions function of $\iota$ - $Al_2O_3$ . . . . .	77
18. Simulated x-ray diffraction pattern of $\iota$ - $Al_2O_3$ as compared to measured ones . . . . .	79
19. Calculated total energy vs. volume of $\alpha$ - $Al_2O_3$ , $\gamma$ - $Al_2O_3$ , and $\iota$ - $Al_2O_3$ . . . . .	80
20. Phonon dispersion along high symmetry lines. . . . .	83
21. Phonon density of states of $\iota$ - $Al_2O_3$ . Top panel: total DOS, middle panel: Al PDOS, and bottom panel: O PDOS. . . . .	84
22. Zone center frequency modes of $\iota$ - $Al_2O_3$ plotted against the localization index (LI). . . . .	85
23. Temperature dependent specific heat capacity at constant volume ( $C_V$ ) for $\iota$ - $Al_2O_3$ . . . . .	86
24. Isothermal bulk modulus of $\iota$ - $Al_2O_3$ as a function of pressure at 295 K. . . . .	87
25. Gibbs free energy G(P, T) of $\iota$ - $Al_2O_3$ in eV. . . . .	88
26. Difference in G(P, T) between $\gamma$ - $Al_2O_3$ and $\iota$ - $Al_2O_3$ in eV. . . . .	89

27. Calculated band structure of $\iota$ - $Al_2O_3$ along high symmetry points of the BZ.	90
28. Calculated total, Al partial, and O partial electron density of states of $\iota$ - $Al_2O_3$ . Orbital components are as indicated.	91
29. Distribution of effective charge $Q^*$ of individual atoms in $\iota$ - $Al_2O_3$ .	92
30. Calculated frequency dependent dielectric functions of $\iota$ - $Al_2O_3$ .	94
31. Calculated Al-K edges in $\iota$ - $Al_2O_3$ . Top panel: averaged Al-K spectra. Bottom panels: average spectra of different groups.	97
32. Calculated Al-L3 edges in $\iota$ - $Al_2O_3$ . Top panel: averaged Al-L3 spectra. Bottom panels: average spectra of different groups.	98
33. Calculated O-K edges in $\iota$ - $Al_2O_3$ . Top panel: averaged O-K spectra. Bottom panels: average spectra of different groups	99
34. $B_{11}C$ - $CBC$ structure in the rhombohedral lattice. The small balls in the figures are C atoms and a large ball in the middle of C-B-C chain is B atom	103
35. $B_{12}$ - $CCC$ structure in the rhombohedral lattice. The balls in the figures are C atoms in $CCC$ chain.	103
36. 180-atom supercell model of $B_{11}C$ - $CBC$ in the hexagonal lattice. The figure is slightly rotated about the c- and a-axes in clockwise direction.	108
37. Supercell model of $B_{11}C$ - $CBC$ in a-b plane.	108
38. Hydrostatic pressure and total energy vs. hydrostatic strain $(V-V_0)/V_0$ in $B_{11}C$ - $CBC$ .	111
39. Hydrostatic pressure and total energy vs. hydrostatic strain $(V-V_0)/V_0$ in $B_{12}$ - $CCC$ .	112
40. Uniaxial stress vs. uniaxial strain along the crystallographic c-axis in $B_{11}C$ - $CBC$ and $B_{12}$ - $CCC$ models.	113

41. Calculated $C_{ij}$ values at different uniaxial strains along the crystallographic c-axis in $B_{11}C-CBC$ . . . . .	115
42. Calculated $C_{ij}$ values at different uniaxial strains along the crystallographic c-axis in $B_{12}-CCC$ . . . . .	116
43. Average bond length in CBC chain vs. uniaxial strain ( $\epsilon$ ) in $B_{11}C-CBC$ . . . . .	118
44. Average CBC chain angle vs. uniaxial strain ( $\epsilon$ ) in $B_{11}C-CBC$ . . . . .	118
45. Atomic configurations in $B_{11}C-CBC$ model at different uniaxial strains. B atoms in the middle of chains are colored differently for easy visual distinction. (a) At strain 0.23; (b) at strain 0.24. (Pink=B in icosahedra; Grey=C; Dark Violet=B in chain) . . . . .	119
46. Average bond length in CBC chain vs. uniaxial strain ( $\epsilon$ ) in $B_{12}-CCC$ . . . . .	120
47. Average CBC chain angle vs. uniaxial strain ( $\epsilon$ ) in $B_{12}-CCC$ . . . . .	121
48. Atomic configurations in $B_{12}-CCC$ model at different uniaxial strains. (a) At $s = 0.22$ , (b) at $s = 0.23$ , (c) at $s = 0.24$ and (d) at $s = 0.25$ . (Pink=B; Grey=C) . . . . .	122
49. Change in volume and total energy with uniaxial strain along the crystallographic c-axis in $B_{11}C-CBC$ . . . . .	123
50. Change in volume and total energy with uniaxial strain along the crystallographic c-axis in $B_{12}-CCC$ . . . . .	124
51. RPDF plots of $B_{11}C-CBC$ model at different uniaxial strains ( $s$ ) along the crystallographic c-axis. . . . .	125
52. RPDF plots of $B_{12}-CCC$ model at different uniaxial strains ( $s$ ) along the crystallographic c-axis. . . . .	126

53. Distribution of effective charge  $Q^*$  at uniaxial strains ( $s$ ) of 0.00, 0.23, and 0.24 in  $B_{11}C$ - $CBC$  model. Horizontal lines at 3.0 and 4.0 represent the number of valence electrons in neutral B and C atoms respectively. . . . 128
54. Distribution of effective charge  $Q^*$  at uniaxial strains ( $s$ ) of 0.00, 0.22, 0.24, and 0.25 in  $B_{12}$ - $CCC$  model. Horizontal lines at 3.0 and 4.0 represent the number of valence electrons in neutral B and C atoms respectively. . . . 129
55. Calculated total density of states (TDOS) of  $B_{11}C$ - $CBC$  model at different strains ( $s$ ). Vertical line represents top of the VB which is set to zero eV . . 131
56. Calculated total density of states (TDOS) of  $B_{12}$ - $CCC$  model at different strains ( $s$ ). Vertical line represents top of the VB which is set to zero eV . . 132

## TABLES

Table	Page
1. Experimental Structural Data of 3/2 mullite . . . . .	37
2. Relaxed volume and lattice constants ( Å ) of mullite models scaled back to the unit cell. . . . .	44
3. Calculated elastic stiffness constants of mullite phases (GPa). . . . .	48
4. Calculated and measured bulk mechanical properties of mullite phases (GPa). .	50
5. Calculated refractive indices of mullite phases. . . . .	65
6. Experimental Structural Data of High Alumina Content Mullite Phase. . . . .	72
7. Initial idealized model of $\iota$ - $Al_2O_3$ derived from high alumina mullite phase. .	73
8. Al and O Groups in the Relaxed $\iota$ - $Al_2O_3$ Model. . . . .	76
9. Elastic constants and bulk moduli of $\iota$ - $Al_2O_3$ (GPa) . . . . .	82
10. Crystal structural data of $B_{11C}$ - $CBC$ and $B_{12}$ - $CCC$ supercell models. . . . .	107
11. Calculated elastic constants ( $C_{ij}$ ) of the equilibrium structure of $B_{11C}$ - $CBC$ and $B_{12}$ - $CCC$ models (in GPa). . . . .	115

## ACKNOWLEDGMENTS

I am truly indebted and thankful to my advisor Dr. Wai-Yim Ching for his encouragement, supervision and constant support throughout my research. This would not have been possible without his help.

I have been fortunate enough to have friendly and helpful members in electronic structure group. My special thanks goes to Dr. Paul Rulis for his help and support in my daily research works. I would like to thank to Dr. Lizhi Ouyang for his help and discussions on phonon and thermodynamic properties calculations.

I would like to thank all the members of my dissertation committee for their valuable comments to my work and kindly serving on my committee.

My parents have been the constant source of inspiration throughout my life and I would not be here without their sacrifice and unconditional love.

Finally I would like to thank University of Missouri-Kansas City , Department of Physics, Department of Geosciences and U. S. department of energy (DOE) for their support in many ways.

## DEDICATION

To my parents with love and appreciation

Life is movement from unknown to unknown.

J. KRISHNAMURTI

## CHAPTER 1

### INTRODUCTION

*Ab initio* simulations are becoming increasingly popular in scientific research especially in areas of material science and condensed matter physics. It has raised itself to be recognized as a third discipline bridging the theory and the experiments. Often calculations, which are the direct implementation of exact known theory, have the capacity to go into subtle details leading to a better and deeper understanding of materials under study.

In condensed matter physics, *ab initio* calculation is the process of solving exactly known quantum mechanical equations for systems of atoms which could be a simple crystal or a complex and disordered structures. However except for simple atoms, solving these equations is not that easy . When the number of particles in a system increases (number electrons and nuclei), solving Schrödinger's equations becomes almost impossible. This difficulty arises because of electron interactions and *ab initio* calculations were limited to simple atoms and simple molecules of few atoms.

Better techniques and methods are constantly developed and implemented to bring the real materials into realm of *ab initio* simulations. It is not easy as the real materials are complex and disordered. They have defects, impurities, interfaces and so on. Large structural models are required to include the defects, impurities and other structural complexities which adds tremendous amount of computational cost. Major development of *ab initio* methods with practical applications took place when many electron interactions in a system was possible to be approximated using a set of one electron equations (Hartree-Fock method) or using density functional theory (DFT) (to be discussed in next chapter). This development led the *ab initio* calculations flourish in physics and chemistry covering

many different materials.

A plethora of ceramic materials are important in traditional use and carry a number of possibilities to be useful in advanced technological applications as well. There is always a challenge to uncover those possibilities hidden in materials so the humanity get utmost benefit. In the past, the only way of exploring material properties was the experimental approach, a trial and error method, which often is difficult, time consuming, expensive and even dangerous. The experiments are important and cannot be avoided but in many cases, theoretical calculations can be useful in guiding experiments making them efficient and economic and also can help in analyzing measured results.

There are cases where experiments have limitations for maintaining right mechanical and thermodynamic conditions like very high pressure-temperature condition, very high electric and magnetic field gradients and so on. For example, it is almost impossible to experiment how a material will behave in an environment of the pressure and temperature of interior of the earth whereas in principle there is no such a limitation for calculations. However a key question is whether or not it accurately models the reality. Often it is difficult to prepare samples free from impurities and defects which adds uncertainties to the measured results. In such cases, the analysis of effect of impurities and defects on measured results can be facilitated using related calculated results.

Theoretical calculations are becoming increasingly efficient and capable of handling large systems containing impurities, defects, surfaces, interfaces and so on. Calculations on pure and ideal materials and those with impurities, defects can show changes in physical properties. A comprehensive theoretical study of materials, covering a wide range of physical properties, is possible within one setting and can present an overall picture of material properties. This could be an important guide for experimental setup and help to find an efficient way for tailoring the materials for specific use.

*Ab initio* calculations are also not free from limitations. It is always difficult to construct right models with impurities, defects, interfaces and so on that mimic real materials. Often experimental results are necessary to check the credibility of calculations and in many cases experimental samples and models used in calculations can be very different. Most of the *ab initio* calculations are the ground state properties of materials. Although it is important in understanding material properties, it may not represent accurately for the materials in their general applications. Further, distribution of defect and impurities could take place in many ways and it is not possible to construct models considering all of those possibilities.

With modern computing facilities and highly optimized density functional theory (DFT) based methods, *ab initio* calculations are possible on complex and disordered systems which used to be a dream in past few years. This dissertation work is such an adventure of *ab initio* calculations of complex and disordered systems. Primary simulation packages used for this works are Vienna *ab initio* simulation package (VASP) [1–3] and orthogonalized linear combinations of atomic orbitals (OLCAO) [4]. Both packages are based on density functional theory. The VASP is used for structural relaxation and geometry optimization. It is also used for force and stress related calculations. While, the OLCAO package, which is very suitable for complex and disordered system, is used for electronic structure and spectroscopic properties calculation.

One of the complex systems used in this dissertation works is mullite. Mullite has immense industrial importance and potential candidate for high end technological use. It has many phases with varying content of alumina ( $Al_2O_3$ ) and silica ( $SiO_2$ ) between the sillimanite, a perfect crystal with equal ratio of  $Al_2O_3$  and  $SiO_2$ , and  $\iota$ - $Al_2O_3$  a disordered alumina phase. As the alumina in the structure increases, the mullite structure becomes more and more disordered. It is important to know how mullite properties change with

changing its alumina content. Mullite applications, both traditional and modern, can be grouped as monolithic mullite ceramics, mullite coatings, and mullite matrix composites. Despite its wide application, very little theoretical results exist for mullite. One of the questions this dissertation work addresses is how the elastic and electronic properties of mullite change with variations in alumina content.

*Ab initio* simulations are not limited only in calculating the physical properties of known structures. One of the active parts in theoretical research is finding a way to model unknown structures. Though this predictive power of unknown structure is not fully achieved, present DFT can be exploited if the starting structure is available. The mullite-like phase of alumina,  $\iota$ - $Al_2O_3$ , although speculated since more than fifty years ago [5], is relatively unknown phase and structural details are not available. Measured x-ray diffraction patterns [6, 7] of it were found similar to that of mullite phases indicating structural similarity of  $\iota$ - $Al_2O_3$  with mullite. If we consider the aluminosilicate solid solution series, it makes sense to think that structure of  $\iota$ - $Al_2O_3$  is close to high alumina mullite phase. In this scenario, a better option to model the structure of  $\iota$ - $Al_2O_3$  is starting from the high alumina mullite structure. Using a theoretically constructed model of  $\iota$ - $Al_2O_3$ , a number of physical properties which includes elastic, thermodynamic, electronic and spectroscopic properties have been calculated.

Simulation of dynamic events is always interesting. Simulations can unravel microscopic as well macroscopic details in every step of the dynamic event. One such an simulation of dynamic event included in this dissertation is amorphisation of boron carbide. Boron carbide is a lightweight and very strong material [8]. It is a promising material for body armor but suffers catastrophic loss of resistance when impact pressure exceeds certain limit due to localized amorphisation. Despite many experimental and theoretical works, mechanism of amorphisation is still not clear.

The *ab initio* calculations presented in this dissertation works not only enhance knowledge of the materials undertaken but also show some of the techniques how modern DFT can be exploited for theoretical research. The *ab initio* calculations on mullite, which are presented in chapter four, are the first of this kind and also the first study of mullite properties in relation to its alumina content. It is hoped it will prove an important step in theoretical research in mullite. The comprehensive calculations on  $\iota$ - $Al_2O_3$  presented in chapter five brings it out from the realm of speculations after more than 50 years. This work could stir interest and curiosity in this relatively unknown phase of alumina. The *ab initio* simulation of failure mechanism of boron carbide, detailed in chapter six, shows how the structure leads to amorphisation under uniaxial compression. Many different techniques are used to conform the amorphisation of the structure and to analyze the failure mechanism under uniaxial compression.

## CHAPTER 2

### THEORETICAL BACKGROUND

The most fundamental understanding of physical properties of atoms, molecules and solids begins with solving many-atom many-electron Schrödinger's equation 2.1.

$$\left[ -\sum_j^N \frac{\hbar^2}{2M_j} \nabla_j^2 - \sum_i^n \frac{\hbar^2}{2m_i} \nabla_i^2 + \sum_j^N \sum_{p>j}^N \frac{Z_j Z_p}{|R_j - R_p|} - \sum_{i=1}^n \sum_{j=1}^N \frac{Z_j e}{|r_i - R_j|} + \sum_{i=1}^n \sum_{q>i}^n \frac{e^2}{|r_i - r_q|} \right] \psi(\mathbf{r}_1, \mathbf{r}_2, \dots, \mathbf{r}_N) = E\psi(\mathbf{r}_1, \mathbf{r}_2, \dots, \mathbf{r}_N) \quad (2.1)$$

Where,  $M$  and  $N$  are number of nuclei and electrons in the system respectively. The  $M$ ,  $Z$ , and  $R$  are mass, charge and spatial position of nucleus. The  $m$ ,  $e$ , and  $r$  are mass, charge and spatial position of electron. In above equation 2.1 the first term represents the kinetic energy of nuclei, the second term kinetic energy of electrons, the third term Coulomb repulsion arising from ion-ion repulsion, the fourth term Coulomb potential arising from ion-electron interaction and the last term represents electron-electron interaction.

In equation 2.1, everything is exactly known but it is too complicated to solve. In order to solve the many ions-many electrons Schrödinger's equation 2.1, a number of theories and approximations are implemented.

The first intelligent effort to simplify this complicated Schrödinger's equation 2.1 is Born-Oppenheimer approximation. This approximation is based on the fact that electrons and nuclei exhibit vastly different dynamics. The nuclei are more heavier than the electrons and the nuclei can be considered as stationary in comparison to electrons. In this approximation, electrons move within fixed external potential due to positive ions reduc-

ing many-ion many-electron problem to many-electron problem and can be expressed by following equation 2.2.

$$\left[ -\sum_i^n \frac{\hbar^2}{2m_i} \nabla_i^2 - \sum_{i=1}^n \sum_{j=1}^N \frac{Z_j e}{|r_i - R_j|} + \sum_{i=1}^n \sum_{q>i}^n \frac{e^2}{|r_i - r_q|} \right] \psi(\mathbf{r}_1, \mathbf{r}_2, \dots, \mathbf{r}_N) = E\psi(\mathbf{r}_1, \mathbf{r}_2, \dots, \mathbf{r}_N) \quad (2.2)$$

However, solving many-electron Schrodinger's equation 2.2 is still too complicated when the system at hand is not simple atoms or molecule of them. The many-electron wave function contains  $3N$  variables (from now on  $N$  is number of electrons and  $n$  is used for electron density ). Most of the physical problems of interest consists of a number of interacting electrons and ions leaving the equation 2.2 intractable.

Several theories and schemes are developed for solving the many-electron problem. One of the earliest notable scheme that was used to solve the many-electron problem is the Thomas-Fermi approximation [9, 10]. According to this model the total kinetic energy of the electrons can be obtained using only spatially varying electron density  $n(\mathbf{r})$ . With classical expressions of electron-nuclear and electron-electron interactions, the total energy of a system can be expressed as the equation 2.3.

$$\begin{aligned} E &= T + U_{e-Z} + U_{e-e} \\ &= C_F \int [n(\mathbf{r})]^{5/3} d^3r + \int n(\mathbf{r}) V_n(\mathbf{r}) d^3r + \frac{1}{2} e^2 \int \frac{n(\mathbf{r}) n(\mathbf{r}')}{|\mathbf{r} - \mathbf{r}'|} d^3r d^3r' \end{aligned} \quad (2.3)$$

Where

$$C_F = \frac{3\hbar^2}{10m_e} \left( \frac{3}{8\pi} \right)^{2/3} \quad (2.4)$$

In the right side of above equation 2.3, the first term is kinetic energy, the second term is

electron-nuclear interactions and the third term is electron-electron interaction.

The Thomas-Fermi model simplified the problem significantly using electron density which contains only three degrees of freedom but this model suffers from many inaccuracies particularly because of incorrect expression for kinetic energy. Further, this model does not include exchange energy which arise from the Pauli exclusion principle. However it is viewed as the precursor to the modern Density Functional Theory (DFT).

Another important step in solving many electron problem was from the Hartree and Fock . In Hartree and Fock method, many-electron problem is reduced to a set of single electron problem. In this approximation [11, 12] true N-electron wave function  $\psi$  is expressed as a single Slater determinant of N single particle wave function  $\psi_i(\mathbf{x}_i)$ .

$$\Psi(\mathbf{x}_1, \mathbf{x}_2, \mathbf{x}_3, \dots, \mathbf{x}_N) = \frac{1}{\sqrt{N!}} \begin{vmatrix} \psi_1(\mathbf{x}_1) & \psi_1(\mathbf{x}_2) & \dots & \psi_1(\mathbf{x}_N) \\ \psi_2(\mathbf{x}_1) & \psi_2(\mathbf{x}_2) & \dots & \psi_2(\mathbf{x}_N) \\ \cdot & \cdot & & \cdot \\ \cdot & \cdot & & \cdot \\ \cdot & \cdot & & \cdot \\ \psi_N(\mathbf{x}_1) & \psi_N(\mathbf{x}_2) & \dots & \psi_N(\mathbf{x}_N) \end{vmatrix} \quad (2.5)$$

Where  $\psi_i(\mathbf{x}_i)$  is the product of  $\phi_i(\mathbf{r}_i)$  spatial orbital function and  $\sigma(s)$  electron spin functions expressed as  $\psi_i(\mathbf{x}_i) = \phi_i(\mathbf{r}_i)\sigma(s)$ .

The exchange of two particles (electrons) is equivalent to exchange of two columns in Slater determinant in equation 2.5. This changes the sign of the determinant and satisfies anti symmetric nature of the wave function. When any two rows of the Slater determinant are equal, the determinant becomes equal to zero. So for a non-zero Slater determinant, all  $\psi_i$ 's should be different which satisfy the Pauli exclusion principle. The Hartree-Fock energy can be determined using the Slater determinant 2.5 as follows.

$$\begin{aligned}
E_{HF} &= \langle \psi_{HF} | \hat{H} | \psi_{HF} \rangle \\
&= \sum_i^N \int \psi_i^*(\mathbf{x}) \left[ -\frac{1}{2} \nabla^2 + v(\mathbf{x}) \right] \psi_i(\mathbf{x}) d\mathbf{x} \\
&+ \frac{1}{2} \sum_i^N \sum_j^N \int \int \frac{|\psi_i(\mathbf{x})|^2 |\psi_j(\mathbf{x}')|^2}{|\mathbf{x} - \mathbf{x}'|} d\mathbf{x} d\mathbf{x}' \\
&- \frac{1}{2} \sum_i^N \sum_j^N \int \int \frac{\psi_i^*(\mathbf{x}) \psi_i(\mathbf{x}') \psi_j^*(\mathbf{x}') \psi_j(\mathbf{x})}{|\mathbf{x} - \mathbf{x}'|} \delta_{s_i s_j} d\mathbf{x} d\mathbf{x}'
\end{aligned} \tag{2.6}$$

The first and second term in the right side of the equation 2.6 are simply the contributions as kinetic energy and electron-ion potential energy. The third term arises from the distribution of charge of N electrons. When  $s_i \neq s_j$ , where  $s_i$  is the spin of  $i^{th}$  electron and  $s_j$  is the spin of  $j^{th}$  electron, the last term in above equation 2.6 vanishes as demanded by the Pauli principle. This last term is called as exchange energy.

Although the Hartree-Fock model calculates exchange energy exactly it neglects correlation between electrons and it can lead to a large deviation from experimentally observed results. To account for the limitation of Hartree-Fock model, a number of developments are made on it which are called post Hartree-Fock methods . These post Hartree-Fock methods [13–15] overcome some of the limitations in Hartree-Fock method but results in a dramatic increase in computational cost.

A different and better method is density functional theory (DFT) which includes both exchange and correlation energies. The DFT is a powerful quantum mechanical theory used to calculate electronic structure of many-body problem using spatially varying electron density  $n(\mathbf{r})$ . DFT appears as the revival of Thomas-Fermi model [9, 10] but it is based on the Hohenberg-Kohn theorems [16]. The two Hohenberg-Kohn theorem which are very important in development of DFT are as follows.

Theorem 1.

*The external potential ( $V_{ext}$ ) is a unique functional of the electron density  $n(\mathbf{r})$ .*

Theorem 2.

*For a density  $n(\mathbf{r})$  such that  $n(\mathbf{r}) \geq 0$  and  $\int n(\mathbf{r})d\mathbf{r} = N$ ;  $E_0 \leq E[n]$ .*

*Where  $E[n]$  is energy functional and  $N$  is total number of electrons in the system.*

The first Hohenberg-Kohn theorem implies that the electron density also determines total energy and hence wave function of the system. The energy functional of a system can be written in terms of external potential as the following equation 2.7.

$$E[n(\mathbf{r})] = \int n(\mathbf{r})V_{ext}(\mathbf{r})d\mathbf{r} + F[n(\mathbf{r})] \quad (2.7)$$

In equation 2.7, the  $F[n(\mathbf{r})]$  is unknown but it is the functional of the electron density. It does not depend on the system so it is also called universal functional.

These two Hohenberg-Kohn theorems give theoretical justifications for the modern density functional theory whereas the Kohn and Sham [17] derived a set of equations laying practical approach in solving actual Schrödinger's equation. In Kohn and Sham formulation, a system of  $N$  interacting electrons is treated as a fictitious system of non-interactive electrons with a density  $n(\mathbf{r})$  with a constraint  $\int n(\mathbf{r})d\mathbf{r} = N$ . The energy functional  $E[n(\mathbf{r})]$  in Kohn and Sham approach, where electrons move within an effective potential  $V_{eff}(\mathbf{r})$ , can be expressed as the following equation 2.8.

$$E[n(\mathbf{r})] = E_k[n(\mathbf{r})] + E_{e-e}[n(\mathbf{r})] + U_{e-i}[n(\mathbf{r})] + E_{XC}[n(\mathbf{r})] \quad (2.8)$$

Where  $E_k[n(\mathbf{r})]$  is kinetic energy of the electrons,  $E_{e-e}[n(\mathbf{r})]$  is electron-electron energy,  $U_{e-i}[n(\mathbf{r})]$  electron-ion interaction potential and  $E_{XC}[n(\mathbf{r})]$  is exchange-correlation energy resulting from Pauli exclusion principle and other factors which are not exactly known.

$$E_k[n(\mathbf{r})] = -\frac{1}{2} \sum_{i=1}^N \int \psi_i^*(\mathbf{r}) \nabla^2 \psi_i(\mathbf{r}) d\mathbf{r} \quad (2.9)$$

$$E_{e-e}[n(\mathbf{r})] = \frac{1}{2} \int \int \frac{n(\mathbf{r})n'(\mathbf{r}')}{|\mathbf{r} - \mathbf{r}'|} d\mathbf{r}d\mathbf{r}' \quad (2.10)$$

$$U_{e-i}[n(\mathbf{r})] = \int v_{ext}n(\mathbf{r})d(\mathbf{r}) \quad (2.11)$$

The second Hohenberg-Kohn theorem is about the minimization of total energy through the electron density. It is desired to minimize the energy functional  $E[n(\mathbf{r})]$  for a given external potential keeping the number of electrons  $N$  fixed. For this case minimizing the  $E[n(\mathbf{r})] - \mu N$ , which is a method of Lagrange multipliers, we get,

$$\begin{aligned} \frac{\delta}{\delta n(\mathbf{r})} \left[ E[n(\mathbf{r})] - \mu \int n(\mathbf{r})d(\mathbf{r}) \right] &= 0 \\ \Rightarrow \mu &= \frac{\delta E[n(\mathbf{r})]}{\delta n(\mathbf{r})} \end{aligned} \quad (2.12)$$

where  $\mu$  is the Lagrange multiplier with constraint  $\int n(\mathbf{r})d\mathbf{r} = N$ . Using equation 2.12 in equation 2.8 we get,

$$\left[ \frac{\delta E_k[n(\mathbf{r})]}{\delta n(\mathbf{r})} + \frac{\delta E_{e-e}[n(\mathbf{r})]}{\delta n(\mathbf{r})} + \frac{\delta U_{e-i}[n(\mathbf{r})]}{\delta n(\mathbf{r})} + \frac{\delta E_{XC}[n(\mathbf{r})]}{\delta n(\mathbf{r})} \right] = \mu \quad (2.13)$$

Above equation 2.13 can be expressed in simple form using the effective potential  $V_{eff}$  as,

$$\frac{\delta E_k[n(\mathbf{r})]}{\delta n(\mathbf{r})} + V_{eff}(\mathbf{r}) = \mu \quad (2.14)$$

where,

$$V_{eff}(\mathbf{r}) = V_{ext}(\mathbf{r}) + \int \frac{n(\mathbf{r}')}{|\mathbf{r} - \mathbf{r}'|} d(\mathbf{r}') + V_{XC}(\mathbf{r}) \quad (2.15)$$

and

$$V_{XC}(\mathbf{r}) = \frac{\delta E_{XC}[n(\mathbf{r})]}{\delta n(\mathbf{r})} \quad (2.16)$$

Now, we can write one-electron Schrödinger's equations as follows.

$$\left[ -\frac{1}{2} \nabla^2 + V_{eff}(\mathbf{r}) \right] \psi_i(\mathbf{r}) = \varepsilon_i \psi_i(\mathbf{r}) \quad (2.17)$$

By solving equation 2.17 self consistently for N electrons and the density calculated using following equation,

$$n(\mathbf{r}) = \sum_i^N |\psi_i(\mathbf{r})|^2 \quad (2.18)$$

the ground state energy  $E_0$  and the ground state density  $n_0(\mathbf{r})$  can be obtained. In theory, Kohn-Sham approach is exact but in reality the exchange-correlation functional  $E_{XC}[n(\mathbf{r})]$  is unknown. Finding accurate approximation to  $E_{XC}[n(\mathbf{r})]$  is the biggest challenge in Kohn-Sham DFT.

One of the approximation used to address exchange-correlation energy functional is local density approximation (LDA) as shown in equation 2.19.

$$E_{XC}[n] = \int \varepsilon_{XC}[n(\mathbf{r})] n(\mathbf{r}) d\mathbf{r} \quad (2.19)$$

In this approximation,  $\varepsilon_{XC}$  is the exchange-correlation energy of an electron in an homogeneous electron gas of density  $n(\mathbf{r})$ . Many ground state properties are well described by LDA. This surprising success of LDA is partially attributed to systematic error cancellation [18] that is LDA overestimates exchange part and underestimates correlation part resulting in unexpected accuracy of  $E_{XC}$ . For many years, the LDA has been used in solid state physics and it is still one of the most popular choice. However, it also has limitations in many areas. Since LDA approximates energy of a system of the true density by local constant density, it suffers when there is rapid change in density such as in atoms, molecules,

surfaces, etcetera.

Various techniques are implemented to improve the LDA in quest to address its limitations. They do not always show the improvement in LDA so one should be always careful while choosing them. In LDA, one considers only the local electron density at a point  $\mathbf{r}$ . A real system is always spatially inhomogeneous and the LDA ignores varying nature of electron density. So, an obvious technique to improve LDA is to include the rate of spatial variation of electron density in exchange-correlation energy functional  $E_{XC}$ .

Numerous schemes are developed to include the rate of spatial variation of electron density in LDA. The exchange-correlation functional that includes the rate of spatial variation of electron density are of the form

$$E_{XC}^G GA[n(\mathbf{r})] = \int d\mathbf{r} f(n(\mathbf{r}), \nabla n(\mathbf{r})) \quad (2.20)$$

and are known as generalized gradient approximation (GGA) [19]. In above equation 2.20,  $f(n(\mathbf{r}), \nabla n(\mathbf{r}))$  is the function of local density  $n(\mathbf{r})$  and gradient of  $n(\mathbf{r})$ ,  $\nabla n(\mathbf{r})$ . There are many GGA based methods employed to construct  $f(n(\mathbf{r}), \nabla n(\mathbf{r}))$  and they could be very different from one another. Nowadays, the most popular GGAs are PBE by Perdew, Burke and Ernzerhof [20] and BLYP, a combination of Becke's exchange functional [21] and with the correlation functional of Lee, Yang and Parr [22]. The PBE is popular in physics community where as BLYP is in chemistry. Finding better and more accurate exchange-correlation functional is an active area of theoretical research.

## CHAPTER 3

### SIMULATION PACKAGES AND METHODS USED

Density Functional Theory (DFT) is the most popular and efficient method for solving the many body problem in condensed matter physics and is implemented in various simulation packages. Differences among these packages could be basis functions used in constructing Bloch functions and methods employed to solve Kohn-Sham equations. No single method and simulation package is perfect and they have their own advantages and disadvantages. In this study, two simulation packages Vienna *ab initio* simulation package (VASP) [1–3] and orthogonalized linear combination of atomic orbitals (OLCAO) [4] are the primary tools. They use different basis sets and the combination of these two packages is well suited and successfully demonstrated in many recent publications [23–31].

#### **3.1 Vienna *ab initio* Simulation Package (VASP)**

Vienna *ab initio* simulation package (VASP) is a package of computer programs used for electronic structure calculations and quantum mechanical molecular dynamics. It has a flexibility of using either density functional theory or Hartree-Fock approximation while computing solutions of Schrödinger's equation. Further, hybrid functionals, Green functions method and many-body perturbations theory are also available in VASP. VASP uses plane wave basis set and interactions between electrons and ions are addressed using ultrasoft pseudo potentials (USPP) [32, 33] or projector augmented wave (PAW) [34, 35] method.

VAPS uses efficient iterative matrix diagonalization techniques, blocked Davidson algorithm and residual minimization with direct inversion of the iterative subspace (RMM-

DIIS), to calculate ground state energy. Either of them or combination of both can be used usually considering size of the system. The blocked Davidson algorithm is stable but slow whereas RMM-DIIS is significantly faster. A combination of both, in which first steps in iteration uses blocked Davidson algorithm and RMM-DIIS afterwards, can be the best choice for the large systems. VASP uses highly efficient Broyden and Pulay density mixing schemes which help to speed up the self-consistency cycle.

VASP is accurate and efficient for relaxation and geometry optimization. VASP has few choices in controlling how the ions are updated and moved in the process of relaxation. A quasi-Newton (or variable metric) algorithm, which use forces and stress tensor to search directions to equilibrium positions, is faster but can lead to wrong results if the structure is approximate and far from the equilibrium. On the other hand, conjugate-gradient approximations is slower but is better choice for approximate structures which are far from the equilibrium.

Along with relaxation and geometry optimization of the structures, VASP has also been used for force and stress related calculations. While calculating total energy, one of the important parameters is ISMEAR . In VASP, ISMEAR determines how the partial occupancies are set for each wave function. For total energy and force related calculations, tetrahedron method with Blöchl corrections is the best for insulators and semiconductors. But this also demands higher number of k-points. Computational cost scales linearly with number of k-points. So, for a large system, a Gaussian smearing with gamma point calculation appears right choice particularly while calculating force constant matrix of complex and large crystals to be used in calculating phonon dispersion.

Generally, the projector augmented wave (PAW) method is superior to ultra-soft pseudo-potential (USPP). The PAW potential is an all electron method with frozen core and computationally comparable to pseudo potentials. PAW method has been used for all the

calculations as supplied in the VASP distribution package. For better result of exchange-correlation functional, a gradient correction as developed by Perdew, Burke and Ernzerhof (PBE) [20] has been used. The PBE gradient correction is the best GGA available in VASP but in some cases LDA may be better since it is faster than PBE and results may not be much different from that of PBE.

VASP has both serial and parallel codes. VASP parallel version is very competent and works well in highly parallelized computer clusters and supercomputers. VASP provides parallelization over the band or over the plane wave coefficients or a combination of both. When parallelization is set over the plane wave coefficients only, then all the computer cores will work on every band. This setting results in very slow computing. If the parallelization is only over the bands then each core will work on individual band. Although this is faster but leads to memory problem for larger systems. Parallelization over both bands and plane wave coefficients is best option for large systems as it faster and usually does not lead to memory problem.

With highly efficient parallel VASP code in conjunction with massively parallelized and optimized computer clusters and supercomputers, it is possible to perform accurate DFT calculations in large, complex and disordered systems. The complex and disordered systems included in this dissertation work are mullite and  $\iota$ - $Al_2O_3$ . The other system included is supercell structure of boron carbide. Although the boron carbide is perfect and small crystal, a large supercell of it used in this work is for simulation of amorphization at high compression in which structure ultimately becomes highly complex and disordered. So in all three cases, similar VASP parameters and techniques are used.

VASP needs a minimum of four input files named as INCAR, KPOINTS, POTCAR and POSCAR. The POTCAR file contains the pseudopotential for each atomic species used in calculations. If there are two or more than two atomic species, then the pseudopoten-

tials of atomic species are simply concatenated in POTCAR file. The order of the atomic species should be according to the POSCAR file. The POSCAR file consists of lattice vector and fractional coordinates of atomic positions of the system to be used in calculations. The KPOINTS file contains k-points used in calculations. The INCAR file is very important file and determines what and how to calculate. It consists of relatively large number of parameters and one always should be careful while assigning them. The most of the parameters have adequate default values so, in most cases, only a few of them need to be addressed in INCAR file. A typical sample INCAR, KPOINTS and POSCAR files are presented in appendix A.

In plane wave method, the number of basis functions (number of plane waves included in calculations) are solely determined by cutoff energy. When volume of the structure changes, reciprocal lattice vectors also changes. While modeling the models of mullite phases and iota-alumina, a large change in volume is expected. Similarly, in compression simulation of boron carbide, in both hydrostatic and uniaxial, a large change in volume is expected when the structure undergoes amorphization. To ensure high accuracy and considering the changes in volume in the structure, a high cutoff energy of 700 eV is used. A relatively high accuracy for the ground state electronic convergence limit ( $10^{-7}$  eV) and a small tolerance for the ionic relaxation convergence ( $10^{-5}$  eV) were implemented. A different set of gamma centered k-points mesh is used depending on the size of the structure and type of calculations.

### **3.2 Orthogonalized Linear Combination of Atomic Orbitals (OLCAO)**

The OLCAO is also a density functional theory based all electron method. It is very powerful and efficient for electronic and spectroscopic properties calculations for both crystals and amorphous solids. The details of the OLCAO method are published in many

past publications especially in Ching (1990) [4] and in Ching and Rulis [36].

The root of the OLCAO method can be traced back to the early days when different methods were being developed to solve the Schrödinger's wave equation for many electron systems. As atomic electronic configurations are best described by the atomic orbitals, it was natural phenomenon to use linear combination of atomic orbitals (LCAO) to construct wave function of a many electron systems. The Conyers Herring [37] developed orthogonalized plane wave (OPW) method, a method considered to be the first capable method of band structure calculation. The OPW method, with its conceptual roots to LACO method, helped to improve LCAO method which finally led to modern OLCAO method. The OLCAO method is very efficient and powerful in calculating electronic structure and spectroscopic properties of solids. It is particularly suited to large, complex systems both crystalline and noncrystalline alike.

In OLCAO method, the solid state wave function  $\Psi_{nk}(\mathbf{r})$  is expanded in terms of Bloch functions  $b_{i\gamma}$  as shown in following equation 3.1.

$$\Psi_{i\gamma}(\mathbf{r}) = \sum_{i,\gamma} C_{i\gamma}^n(\mathbf{k}) b_{i\gamma}(\mathbf{k}, \mathbf{r}) \quad (3.1)$$

Where  $\gamma$  represents nonequivalent atoms (different types of atoms as well as different type of the same type) in the cell and  $i$  is the orbital quantum number ( $l, m$ ).

The Bloch functions  $b_{i\gamma}(\mathbf{k}, \mathbf{r})$  are expanded as the linear combination of atom centered atomic orbitals  $u_i(\mathbf{r})$ .

$$b_{nk} = \frac{1}{\sqrt{N}} \sum_v e^{i\mathbf{k}\cdot\mathbf{r}} u_i(\mathbf{r} - \mathbf{t}_\gamma - \mathbf{R}_v) \quad (3.2)$$

Where  $t_\gamma$  is the position of the  $\gamma^{th}$  atom in the cell and  $R_v$  represents the lattice.

The atomic orbitals  $u_i(\mathbf{r} - \mathbf{t}_\gamma - \mathbf{R}_v)$  are made up of two parts, radial and angular.

The radial parts of the atomic orbitals are expanded as the linear combination of Gaussian type of orbitals (GTO). For angular parts, spherical harmonics  $Y_{lm}(\theta, \phi)$  are used. Using GTOs for atomic orbitals brings all the multi-center interaction integrals into analytic forms which are easier and faster to solve.

$$u_i(\mathbf{r}) = \left[ \sum_j^N C_j r^{n-1} e^{(-\alpha_j r^2)} \right] \bullet Y_{lm}(\theta, \phi) \quad (3.3)$$

In above equation 3.3,  $i$  represents the quantum numbers  $n, l$ , and  $m$ . The  $N$  is number of GTOs and the set  $\alpha_j$  are predefined usually guided by past experience and are distributed in geometric series ranging from  $\alpha_{min}$  to  $\alpha_{max}$ . The wave functions of the same atoms can share the same set of exponentials ( $\alpha_j$ ). This practice has a great benefit in reducing computational cost significantly specially for atoms with a large number of orbitals.

In OLCAO method, the charge density  $n(\mathbf{r})$  and the one-electron potential  $V_{cry}(\mathbf{r})$  are expressed as the atom centered Gaussian functions.

$$n_{cry}(\mathbf{r}) = \sum_A \sum_{j=1}^N B_j e^{-\beta_j r^2} (\mathbf{r} - \mathbf{t}_A) \quad (3.4)$$

$$V_{coul}(\mathbf{r}) = \sum_A \left[ -\frac{Z_z}{(\mathbf{r})} e^{-\xi r^2} - \sum_{j=1}^N D_j e^{-\beta_j r^2} \right] (\mathbf{r} - \mathbf{t}_A) \quad (3.5)$$

$$V_{XC}(\mathbf{r}) = \sum_A \sum_{j=1}^N F_j e^{-\beta_j r^2} (\mathbf{r} - \mathbf{t}_A) \quad (3.6)$$

$$V_{cry}(\mathbf{r}) = \sum_A (V_C(\mathbf{r}) + V_X(\mathbf{r})) (\mathbf{r} - \mathbf{t}_A) \quad (3.7)$$

Where  $Z_A$  is the mass number of the atom at the site. The first term in the right side of the equation 3.5 represents the potential near the nucleus. The  $\beta_j$  are predetermined for each atom whereas coefficients  $B_j, D_j, and F_j$  are updated at each self consistent cal-

culations. This is an important practice since if carefully constructed, site specific atom centered potential functions are transferable. Which means self consistent potentials resulted from the calculations of simple systems can be used for more complicated systems.

The charge density calculated using equation 3.4 is very important and should be as close as to true charge density. The set of  $\beta_j$  are also range between a minimum and a maximum values and the number terms between them are fitted in geometric series. The minimum and maximum values of  $\beta_j$  and number of terms in  $\beta_j$  depends on  $Z$  and system.

One of the important features of the OLCAO method is core-orthogonalization. In this process core orbitals are removed from the secular equations 3.8.

$$|H_{i\gamma,j\delta}(\mathbf{k}) - S_{i\gamma,j\delta}(\mathbf{k})E(\mathbf{k})| = 0 \quad (3.8)$$

Where,  $H_{i\gamma,j\delta}(\mathbf{k})$  and  $S_{i\gamma,j\delta}(\mathbf{k})$  are Hamiltonian and overlap matrix respectively. The overlap matrix is given by

$$S_{i\gamma,j\delta}(\mathbf{k}) = \langle b_{i\gamma}(\mathbf{k}) | b_{j\delta}(\mathbf{k}) \rangle \quad (3.9)$$

Suppose, the Bloch sum which consists of core orbitals is  $b_{j\beta}^c(\mathbf{k},\mathbf{r})$  and that of valence orbitals is  $b_{i\alpha}^v(\mathbf{k},\mathbf{r})$ . Now, the orthogonalized valence Bloch sum  $b_{i\alpha}^{v'}(\mathbf{k},\mathbf{r})$  can be expressed as.

$$b_{i\alpha}^{v'}(\mathbf{k},\mathbf{r}) = b_{i\alpha}^v(\mathbf{k},\mathbf{r}) + \sum_{j,\gamma} C_{j\gamma}^{i\alpha} b_{i\alpha}^c(\mathbf{k},\mathbf{r}) \quad (3.10)$$

Where the expansion coefficients in equation 3.10 are given by:

$$C_{j\gamma}^{i\alpha} = -\langle b_{j\gamma}^c(\mathbf{k},\mathbf{r}) | b_{i\alpha}^v(\mathbf{k},\mathbf{r}) \rangle$$

$$C_{j\gamma}^{i\alpha*} = -\langle b_{i\alpha}^v(\mathbf{k},\mathbf{r}) | b_{j\beta}^c(\mathbf{k},\mathbf{r}) \rangle$$

Now the core orthogonalization can be expressed as

$$\langle b_{j\beta}^c(\mathbf{k},\mathbf{r})|b_{i\alpha}^{v'}(\mathbf{k},\mathbf{r})\rangle = \langle b_{j\beta}^{v'}(\mathbf{k},\mathbf{r})|b_{i\alpha}^c(\mathbf{k},\mathbf{r})\rangle = 0$$

There is no standard way to identify the core orbitals from valence orbitals. In OLCAO method, the orbitals deeper than oxygen 2s orbital are treated as core orbitals (i. e. The orbitals which has energy less than that of O 2s orbital). In this orthogonalization process, the non-diagonal elements of Hamiltonian and overlap matrix vanish and resulting matrix consists of blocks of core orbitals and valence orbitals. These separate blocks can be solved separately. This process reduces dimension of secular equations significantly making OLCAO very suitable for large and complex systems.

Another very important feature in OLCAO is flexibility in use of basis set. Different sets of basis expansion (set of orbitals) are used for different purposes. For example, minimal basis, which consist of core and valence atomic orbitals, are used for calculation of effective charge ( $Q^*$ ) and bond order (BO) using Mulliken scheme [38]. It is because effective charge of an atoms and bond order which measures relative strength of a bond between two atoms are relatively localized physical properties.

On the other hand, full basis (FB) consists of one more shell in MB and is used for band structure and density of states (DOS) calculations. Optical and spectroscopic calculations are more accurate when more unoccupied orbitals are included in the basis set. It is why extended basis (EB) which includes one more shell in FB is used for optical and spectroscopic calculations. Orthogonalization of core orbitals to valence orbitals and use of different basis set for different purposes make OLCAO package very efficient and versatile for electronic and spectroscopic calculations.

The OLCAO method is used to calculate various electronic properties which in-

clude band structure, total and partial density of states (DOS), effective charge and bond order (BO) and spectroscopic properties. Spectroscopic properties include optical properties and x-ray absorption near edge structure (XANES) or electron loss near edge structure (ELNES) spectra.

Band structure is one of the basic calculation OLCAO is used for. It is a plot of energy eigen values as a function of k-points in reciprocal space. The k-points are chosen specifically along the high symmetry points of crystal. The band gap between the top of the valence band (VB) and bottom of the conduction band (CB) in band structure shows whether the crystal is metal, semiconductor or insulator.

Density of states (DOS) represent the number of states available for electron to occupy at each energy level in the unit cell. The density of states  $G(E)$  can be expressed as:

$$\begin{aligned} G(E) &= \frac{\Omega}{(2\pi)^3} \frac{d}{dE} \int_{BZ} d\mathbf{k} \\ &= \frac{\Omega}{(2\pi)^3} \int \frac{dS}{|\nabla E|} \end{aligned} \quad (3.11)$$

Where,  $\Omega$  is volume of the unit cell and integral is over the constant energy surface in Brillouin Zone (BZ). The DOS can be resolved into partial DOS (PDOS) for atoms and orbitals.

Effective charge ( $Q^*$ ) is the number of electronic charge associated with an atom. It shows about the charge transfer between the cation and anion in the crystal. The  $Q^*$  is calculated using the Mulliken scheme [38]. In Mulliken scheme, the fractional charge  $\rho_{i\alpha}^{nk}$  of the normalized state  $\psi_{n\mathbf{k}}(\mathbf{r})$  can be expressed using following equations 3.12 and 3.13.

$$1 = \int |\psi_{n\mathbf{k}}(\mathbf{r})|^2 d\mathbf{r} = \sum_{i\alpha} \rho_{i\alpha}^{nk} \quad (3.12)$$

$$\rho_{i\alpha}^{nk} = \sum_{j\beta} C_{i\alpha}^{mk*} C_{i\alpha}^{mk} S_{i\alpha,j\beta} \quad (3.13)$$

Where, the  $i^{th}$  is orbital of the  $\alpha^{th}$  atom.

Now from the fractional charge  $\rho_{i\alpha}^{nk}$ , the effective charge associated with an atom can be found using the following equation 3.14.

$$\begin{aligned} Q^* &= \sum_{n\mathbf{k},occ} \sum_i \rho_{i\alpha}^{nk} \\ &= \sum_{n\mathbf{k},occ} \sum_i \sum_{j\beta} C_{i\alpha}^{mk*} C_{i\alpha}^{mk} S_{i\alpha,j\beta} \end{aligned} \quad (3.14)$$

The another quantity calculated from the Mulliken population analysis is bond order (BO) which measures the relative strength of a bond between two atoms. The BO between atom  $\alpha$  and atom  $\beta$  is given by.

$$\rho_{\alpha\beta} = \sum_{n\mathbf{k},occ} \sum_{ij} C_{i\alpha}^{mk*} C_{i\alpha}^{mk} S_{i\alpha,j\beta} \quad (3.15)$$

In above equations 3.12 to 3.15, the  $C_{i\alpha}^{mk}$  are eigenvector coefficients of  $n^{th}$  band of  $j^{th}$  orbital of atom  $\alpha$ . The  $S_{i\alpha,j\beta}$  are the overlap integrals between the  $i^{th}$  orbital of  $\alpha^{th}$  atom and  $j^{th}$  orbital of the  $\beta^{th}$  atom.

The optical properties of solids are calculated based on the inter band optical absorption theory in random phase approximation. The optical results are important and can be compared with experiments. The frequency dependent optical conductivity  $\sigma_1(\hbar\omega)$  can be calculated using the Kubo-Greenwood formula [39].

$$\sigma_1(\hbar\omega) = \frac{2\pi e\hbar^2}{3m^2\omega\Omega} \sum_{n,m} |\langle \psi_n(\mathbf{k}, \mathbf{r}) | \mathbf{P} | \psi_m(\mathbf{k}, \mathbf{r}) \rangle|^2 f_m(\mathbf{k}) [1 - f_n(\mathbf{k})] \delta(E_n(\mathbf{k}) - E_m(\mathbf{k}) - \hbar\omega) \quad (3.16)$$

Where  $f(\mathbf{k})$  is the Fermi distribution function. The  $m$  is an occupied state and  $n$  is un-

occupied state. The imaginary part of dielectric function  $\varepsilon_2(\hbar\omega)$  can be obtained from the optical conductivity as the following equation 3.17.

$$\varepsilon_2(\omega) = 4\pi \frac{\sigma_1(\hbar\omega)}{\omega} \quad (3.17)$$

and real part of the dielectric function can be obtained from the imaginary part using Kramers-Kronig conversion relation.

$$\varepsilon_1(\omega) = 1 + \frac{2}{\pi} \int_0^\infty \frac{S\varepsilon_2(\hbar\omega)}{S^2 - \omega^2} dS \quad (3.18)$$

Once frequency dependent dielectric functions are calculated, optical constants and electron energy loss function (ELF) can easily be calculated. The static dielectric constant  $\varepsilon_0$  can be obtained as the zero frequency limit of  $\varepsilon_1(0)$ . The frequency dependent refractive index  $n(\omega)$  can be expressed as.

$$n(\omega) = \sqrt{\frac{\sqrt{\varepsilon_1^2(\omega) + \varepsilon_2^2(\omega)} + \varepsilon_1(\omega)}{2}} \quad (3.19)$$

Static refractive index,  $n$ , can be calculated from equation 3.19 with zero frequency limit. In zero frequency limit  $\omega \rightarrow 0$ ,  $\varepsilon_2^2(\omega) \rightarrow 0$  and leads to  $n = \sqrt{\varepsilon_1(0)}$ .

The energy loss function (ELF), which represents the collective response of electrons in the system, can be expressed as.

$$ELF = Im \left\{ -\frac{1}{\varepsilon(\omega)} \right\} = \frac{\varepsilon_2(\omega)}{[\varepsilon_1^2(\omega) + \varepsilon_2^2(\omega)]} \quad (3.20)$$

### 3.3 Elastic and Mechanical Properties Calculations

Materials show their response to stress (load) in many different ways depending on the type, magnitude and duration of the stress. Understanding material behavior under stress is crucial for material application and technological advancement. Elastic constants represent elastic nature of materials and enable calculations of other parameters related to mechanical properties of materials. Elastic constants help in understanding of many physical properties of materials such as interatomic interactions, mechanical stability, material strength, phase transition, and internal structure of the materials to name some.

Two approaches are used for *ab initio* calculations of the elastic properties of materials. One is based on the analysis of total energy of the crystal as a function of volume. The volume ( $V$ ) and strain dependent total energy  $E(V, \varepsilon)$  of a crystal can be expressed as:

$$E(V, \varepsilon) = E(V_0) + V \sum_{i=1}^6 \sigma_i \varepsilon_i + \frac{V}{2} \sum_{i,j=1}^6 C_{ij} \varepsilon_i \varepsilon_j + \dots \quad (3.21)$$

In above equation 3.21,  $\varepsilon_i$  are strain components,  $\sigma_i$  are stress components and  $C_{ij}$  is elastic tensor.

The second is to use strain-stress analysis approach [40]. In this approach, the structure is first relaxed fully, allowing both volume of the structure and ionic position to adjust. Then a small strain is applied to each independent strain element in the fully relaxed structure. The six stress components ( $\sigma_{ij}$ ) are calculated for each strain  $\varepsilon_j$  applied to the structure. The elastic coefficients  $C_{ij}$  are calculated by solving a set of linear equations 3.22:

$$\sigma_{ij} = \sum_{ij} C_{ij} \varepsilon_j \quad (3.22)$$

The above equation is correct for linear relationship between stress and strain. For relation between stress and strain to be linear, applied strain should be small. But small

strain which also results into corresponding small stress may be influenced significantly by the calculation noise and approximations. Generally, strains of  $\pm 1\%$  is good enough in the most cases but in soft materials a little larger strain may be a better choice.

Bulk mechanical properties are clearly related to the elastic constants. However, there is no unique way to get mechanical bulk properties from elastic tensor. In general, there are three approaches commonly used to calculate mechanical bulk properties from elastic tensor. In Voigt's approach [41], bulk modulus ( $K_{Voigt}$ ) and shear modulus ( $G_{Voigt}$ ) are as follows:

$$K_{Voigt} = \frac{1}{9}(C_{11} + C_{22} + C_{33}) + \frac{2}{9}(C_{12} + C_{13} + C_{23}) \quad (3.23)$$

$$G_{Voigt} = \frac{1}{15}(C_{11} + C_{22} + C_{33} - C_{12} - C_{13} - C_{23}) + \frac{1}{5}(C_{44} + C_{55} + C_{66}) \quad (3.24)$$

And in Reuss approach [42]:

$$K_{Reuss} = \frac{1}{(S_{11} + S_{22} + S_{33}) + 2(S_{12} + S_{13} + S_{23})} \quad (3.25)$$

$$G_{Reuss} = \frac{15}{4(S_{11} + S_{22} + S_{33}) - 4(S_{12} + S_{13} + S_{23}) + 3(S_{44} + S_{55} + S_{66})} \quad (3.26)$$

Where  $C_{ij}$  are elastic tensor and  $S_{ij}$  are compliance tensor. Voigt and Reuss approximations give two limits while Hill [43] scheme is to find averages of Voigt and Reuss approximations. So, in Voigt-Reuss-Hill (VRH) approximation, mechanical bulk properties are as follows:

$$K = (K_{Voigt} + K_{Reuss})/2 \quad (3.27)$$

$$G = (G_{Voigt} + G_{Reuss})/2 \quad (3.28)$$

$$E = 9KG/(3K + G) \quad (3.29)$$

and

$$\eta = (3K - 2G)/2(3K + G) \quad (3.30)$$

Where  $E$  and  $\eta$  are Young's modulus and Poisson's ratio respectively.

Calculating  $C_{ij}$  using this technique is pretty simple and in most cases calculations can be completed without major problems. In this method there are two parts. One, the optimization part in which structure is relaxed with relatively higher accuracy allowing to adjust both ionic positions and geometry of the structure. Second part is the actual calculation of  $C_{ij}$ . As mentioned above different strains are applied in the equilibrium structure and then corresponding stress are calculated. How many calculations are needed depends on the symmetry of the structure. For a simple cubic crystal, only two calculations, one for a linear strain and another for a shear strain, are required. For a less symmetric crystal, a maximum of six calculations are needed. In each calculation there are two parts one for +ve strain (eg. +1%) and another for -ve strain (eg. -1%). For each negative and positive strain, corresponding stress tensor is calculated and an average of them is calculated which help improve accuracy by reducing numerical noise.

For a small crystal, the  $C_{ij}$  can be calculated one after another but in the case of large and complex system, this approach may need many days to finish the calculations. So, a parallel version in which calculations for all six strains can run simultaneously is suitable. It is particularly useful in supercomputers where wall clock time is usually limited to 24 hours.

### 3.4 Phonon and Thermodynamic Properties Calculations

Atoms in solids are constantly vibrating about their equilibrium positions under the influence of thermal energy or thermal gradient. This elastic vibration of atoms in solids is

usually referred to as lattice vibrations. The energy in lattice vibration is quantized and this quantum of energy is called phonon. Phonon plays an important role in thermal properties and electrical conductivity of solids and understanding phonon behavior is an important part of solid state physics.

Atoms in solids can vibrate in different ways, a coherent movement of atoms from their equilibrium positions or out of phase movements. The phonon because of a coherent movements of atoms from their equilibrium positions is called acoustic phonon. When the atoms vibrate along the direction of lattice wave propagation, movement of atoms resembles to sound propagation in air and called as longitudinal acoustic (LA). If the atoms vibrate in perpendicular direction to propagation direction then it is called transverse acoustic (TA).

The phonon because of the vibrations of atoms out of phase is called optical phonon. Optical phonon results when atoms are of different masses or charges. Electromagnetic wave (generally infrared) can induce this type of the vibrations in ionic crystals that is why the name optical phonon. The electric field in electromagnetic wave (infrared) move positive ions in the direction of field and the negative ions along the opposite direction giving rise to the out of phase movement of atoms. This is called infrared active phonon. The optical phonon which interact with light indirectly through Raman scattering process is called Raman active. If the atoms in optical phonon vibrate in the direction of lattice wave propagation then optical phonon is called longitudinal optic (LO) and if vibrations are in perpendicular to propagation then the optical phonon is called transverse optic (TO).

Small displacement and linear response [44] are two popular methods for calculating phonons in solids. Each of these two methods has its own advantages and disadvantages. Linear response method has natural ability for splitting of longitudinal and transverse optics (LO-TO splitting). Further, the linear response method does not need supercell

which makes it computationally cheap. On the other hand, the small displacement method is easier to understand. The small displacement method can be used in conjunction with other codes like Vienna *ab initio* simulation package (VASP) [1–3] and quantum espresso [45] which has ability of force matrix calculation. The small displacement method is based on the fact that force constant matrix uses the proportionality nature of force and displacements of atoms provided that displacement of atoms from their equilibrium positions is small. Small displacement method has inability of LO-TO splitting so it may be unsuitable in polar materials.

When atoms displace slightly from their equilibrium positions in a crystal at low temperature, the potential energy function of the crystal can be expanded as equation 3.31 below.

$$U = E_0 + \frac{1}{2} \sum_{i\alpha, jt\beta} \Phi_{i\alpha, jt\beta} u_{i\alpha} u_{jt\beta} \quad (3.31)$$

Where,  $i$  and  $j$  are unit cells,  $s$  and  $t$  are atoms, and  $\alpha$  and  $\beta$  are Cartesian directions. The  $\Phi_{i\alpha, jt\beta}$  is force constant matrix which represent the relationship of force between the atoms for a displacement of atom  $t$  as follows.

$$F_{i\alpha} = -\frac{\partial U}{\partial u_{i\alpha}} - \sum_{jt\beta} \phi_{i\alpha, jt\beta} u_{jt\beta} \quad (3.32)$$

and force constant matrix  $\Phi_{i\alpha, jt\beta}$  is given by:

$$\Phi_{i\alpha, jt\beta} = -\frac{\partial U}{\partial u_{i\alpha} \partial u_{jt\beta}} = \frac{F_{i\alpha}}{u_{jt\beta}} \quad (3.33)$$

From this force constant matrix  $\Phi_{i\alpha, jt\beta}$  a dynamical matrix  $D$  is constructed.

$$D_{s\alpha, t\beta}(\mathbf{q}) = \frac{1}{\sqrt{M_s M_t}} \sum_i \Phi_{i\alpha, jt\beta} e^{i\mathbf{q} \cdot (\mathbf{R}_j + \boldsymbol{\tau}_l - \mathbf{R}_i - \boldsymbol{\tau}_s)} \quad (3.34)$$

In above equation 3.34,  $M_s$  is mass of atom s and  $M_t$  is mass of atom t.  $\mathbf{R}$  represent vectors connecting unit cells (primitive cells) and  $\tau$  represents the position of atoms in a given unit cell. Once the dynamical matrix  $D$  is constructed, the phonon frequencies  $\omega_{qs}$  can be calculated at any wave vector  $\mathbf{q}$ .

In practice, a large enough supercell of relaxed primitive cells (or unit cells) is constructed so that component of forces, induced by slightly displaced atom, at the supercell boundary is negligible. After constructing the right supercell, a single atom t in cell j is displaced slightly along the Cartesian direction  $\beta$  keeping all the rest of atoms fixed in their equilibrium positions. Then the force induced in each atom in the supercell  $\Phi_{is\alpha}$  is calculated. This process is repeated for each non-equivalent atom along the each non-equivalent Cartesian direction. Once the complete set of forces  $\Phi_{is\alpha}$  has been calculated by displacing each non-equivalent atoms in each non-equivalent Cartesian direction, a force constant matrix  $\Phi_{is\alpha, jt\beta}$  is constructed. This force constant matrix  $\Phi_{is\alpha, jt\beta}$  is then used to construct the dynamical matrix as mentioned earlier. By solving dynamical matrix, one gets phonon frequencies at a given q points.

*Ab initio* phonon calculations enables calculations of thermodynamic properties of a solid. *Ab initio* phonon calculations with in the quasi-harmonic approximations (QHA) are computationally intensive, especially for complex crystals [46]. Phonon calculations on equilibrium volume as mentioned above enables thermodynamic variables at constant volume. When temperature is increased at constant volume, the pressure becomes an important factor in determining thermodynamic behavior of the material. Unfortunately, in this small displacement method, it is not possible to calculate temperature and pressure dependent thermodynamic properties from the single equilibrium volume calculation. In order to calculate pressure-temperature dependent thermodynamic properties, a set of phonon calculations on structures with different volume are needed.

In order to get phonon calculations at different volumes, three hydrostatically compressed and three hydrostatically expanded structures are constructed from the ground state equilibrium structure by scaling the lattice vectors by factors of 0.97 to 1.03 in increments of 0.01 increment. This gives seven structures with different volumes. Each structure is then fully optimized allowing for variation in cell shape and ionic positions but keeping the volume fixed. Once all the structures are optimized then *ab initio* phonon calculations are performed for all the seven structures as mentioned above, which can be a computationally very demanding task. The *ab initio* phonon calculation enables to obtain the Helmholtz free energy  $F_V(T)$  at constant volume. Within the Born-Oppenheimer approximation the Helmholtz free energy of a solid consists of the electronic part  $F_V^{el}(T)$  and the vibrational part  $F_V^{vib}(T)$ .

$$F_V(T) = F_V^{el}(T) + F_V^{vib}(T) \quad (3.35)$$

For insulators at ambient temperature, the thermal excitation energy and entropy contribution to  $F_V^{el}(T)$  is negligible. So,  $F_V^{el}(T)$  can be approximated as  $F_V^{el}(0)$  which is the ground state total energy for the electrons obtained from the electronic structure calculation based on density functional theory. The vibrational part of the free energy  $F_V^{vib}(T)$  and the vibrational entropy  $S_V^{vib}(T)$  at constant volume within the quasi-harmonic approximation (QHA) can be expressed as:

$$F_V^{vib}(T) = \sum_q^{BZ} \sum_i^{3N} \left\{ \frac{1}{2} \hbar \omega_i(V, \vec{q}) + \kappa_B T \ln \left( 1 - e^{-\frac{\hbar \omega_i(V, \vec{q})}{\kappa_B T}} \right) \right\} \quad (3.36)$$

$$S_V^{vib}(T) = \sum_q^{BZ} \sum_i^{3N} \left\{ \kappa_B \ln \left( 1 - e^{-\frac{\hbar \omega_i(V, \vec{q})}{\kappa_B T}} \right) + \frac{-\hbar \omega_i(V, \vec{q})}{T} \frac{e^{-\frac{\hbar \omega_i(V, \vec{q})}{\kappa_B T}}}{1 - e^{-\frac{\hbar \omega_i(V, \vec{q})}{\kappa_B T}}} \right\} \quad (3.37)$$

In equations 3.36 and 3.37,  $\omega_i(V, \vec{q})$  is the  $i^{th}$  branch phonon frequency at wave vector  $\vec{q}$

for volume  $V$ . Now the temperature-dependent Helmholtz free energy at constant volume  $F_V(T)$  can be expressed as.

$$F_V(T) = F_V^{vib}(T) + E^{el}(0) \quad (3.38)$$

When  $F_V(T)$  is calculated for each 7 different volume, the data set of  $F_V(T)$  and  $V$  are fitted with a fourth order polynomial. The pressure  $P(V, T)$  at any given temperature is extracted from the fitted data using equation 3.39.

$$P(V, T) = -\frac{\delta F}{\delta V} \quad (3.39)$$

From the set of  $F(V, T)$  and  $P(V, T)$  data, Gibb's free energy  $G(P, T)$  can be calculated according to the equation 3.40.

$$G(P, T) = F(V, T) + PV \quad (3.40)$$

Once  $G(P, T)$ ,  $F(V, T)$ ,  $S(V, T)$ , and  $P(V, T)$  are calculated, all other thermodynamic variables can be obtained using the standard thermodynamic relations.

## CHAPTER 4

### MECHANICAL AND ELECTRONIC STRUCTURE PROPERTIES OF MULLITE

#### 4.1 Introduction

Mullite has a long history as one of the most important ceramic materials that Robert B. Sosman coined as the ceramic phase par excellence [47]. Besides its traditional use as a clay product, for which it is credited with giving superior properties to the Hessian crucibles of the Middle Ages [48], it has become a strong candidate for use as an advanced structural, optical, and functional ceramic in recent years. This is mainly due to many of its outstanding properties such as low thermal expansion, low thermal and electric conductivity, high temperature strength, thermo-shock resistance, excellent creep resistance, and stability under harsh chemical environments [47, 49]. A fundamental understanding of the structures and properties of mullite is therefore an area of increasing importance and attraction to many researchers in the field of ceramic materials.

Mullite has many phases with varying alumina content which can be represented by the alumino-silicate solid solution series  $Al_{4+2x}Si_{2-2x}O_{10-x}$  ( $0 \leq x \leq 1$ ). For  $x = 0$ , the series corresponds to the  $Al_2SiO_5$  polymorphs, sillimanite, andalusite, and kyanite (1/1 mullite,  $Al_2O_3SiO_2$ ), which are ideal crystals. When  $x = 1$ , it leads to a silica-free phase, also known as iota-alumina or  $\iota$ - $Al_2O_3$  [50]. All the possible phases between these two ends members (including  $\iota$ - $Al_2O_3$ ) are collectively known as mullites. Theoretically any mullite composition between sillimanite and  $\iota$ - $Al_2O_3$  is possible [51] but mullite phases observed so far fall into the range  $0.18 \leq x \leq 0.88$  [52]. The most frequently referenced mullites are 3/2 mullite ( $3Al_2O_3 \cdot 2SiO_2$ ,  $x = 0.25$ ), 2/1 mullite ( $2Al_2O_3 \cdot SiO_2$ ,  $x = 0.40$ ), 4/1 mullite ( $4Al_2O_3 \cdot SiO_2$ ,  $x = 0.67$ ), and 9/1 mullite ( $9Al_2O_3 \cdot SiO_2$ ,  $x = 0.842$ ). The

name mullite can be traced to a footnote in the 1924 paper by Bowen and Creig on 3/2 mullite in this journal [53]. It was observed that 3/2 mullite was the only naturally occurring alumino-silicate compound discovered on the Isle of Mull in Scotland [49].

The structures of the mullite phases are complex and disordered although they have always been described using crystallographic semantics. This is primarily because they have structural similarity with sillimanite, the end member of the mullite series with  $x = 0$  which is a simple crystal. Sillimanite has an orthorhombic lattice (space group  $pbnm$ ) with two Al sites (octahedral  $Al_{oct}$  and tetrahedral  $Al_{tet}$ ), one Si tetrahedral site, and four O sites (labeled as O1 - O4) [54]. The Al octahedra are aligned along the crystallographic  $c$ -axis. This feature is somehow maintained in all mullite phases. In sillimanite, the chains of alternating Al/Si tetrahedra are aligned along the  $c$ -axis but in mullite phases this ordered pattern is not maintained. Of the four O sites, only O3 is two-fold coordinated. It connects two Al/Si tetrahedra and is important in understanding the structural pattern of the mullite phases. Starting with the sillimanite structure [8], the structures of the mullite phases can be considered as slight modifications with increased alumina content that is obtained by replacing Si with Al while maintaining the overall charge neutrality [47]. The charge neutral condition requires that some O atoms must be removed thereby introducing vacancies into the structure. This can be illustrated by the following equation.



For every two Si atoms replaced by two Al atoms, one O vacancy is created. The O atoms that are most likely to be removed are the O3 atoms [47]. This leads to the displacement of the tetrahedral Al/Si atoms that were previously connected to the O3 atoms. They move away from the O vacancy site and bond with other nearby O3 atoms. Hence, the original

ordered Al/Si tetrahedral chains in sillimanite become distorted, vacancies are introduced, and some of the O3 atoms become 3-fold bonded with  $Al_{tet}$  or  $Si_{tet}$  in the form of so-called  $T_3O$  triclusters (T stands for Al/Si in a tetrahedral configuration). In mullite phases with higher alumina content (or increasing x), the complexity of the structures increases with an increased number of  $T_3O$  triclusters and O vacancies. This is the reason that all reported data on the crystal structures of mullite phases have partially occupied sites.

Because of their wide range of applications, mullites have received considerable attention over the years [47, 49, 55]. A substantial body of work has covered processing [56–59], structure determination [52, 55, 60–67], characterization [64–66, 68–72], thermodynamics [71, 73], thermal [63, 66, 70, 74–81], mechanical [58, 68–70, 74–76, 78–83] and optical properties [58, 59, 84, 85]. Besides the popular monolithic use of mullites, mullite coatings, fibers, and matrix composites are also becoming increasingly popular in modern technology [59, 62, 77, 85, 86]. For structural applications, the mechanical and elastic properties, especially at high temperatures, are most important. Most published works on the bulk properties are on polycrystalline samples. These data vary widely depending upon their composition, impurities, and the porosity of the samples, and many of them are simply labeled as “mullite” without specifying the actual composition. More recent measurements on single crystals of  $2Al_2O_3SiO_2$  (2/1 mullite) and  $2.5Al_2O_3SiO_2$  (2.5/1 mullite or  $x = 0.5$ ), using either resonant ultrasound spectroscopy (RUS) [78, 81] or Brillouin spectroscopy [66, 79] have provided more reliable data. These single crystal data are in reasonable agreement with each other but fall within a very narrow range of x from 2/1 mullite to 2.5/1 mullite. The temperature dependent elastic stiffness constants show that they decrease linearly with increasing temperature. However, a systematic trend for the mechanical properties of the entire mullite series has not been established.

In spite of the many experimental works cited above, there have been very few

theoretical calculations on the bulk properties of the mullite phases or their underlying electronic structures. Electronic structure and spectroscopic properties of the three crystalline  $Al_2SiO_5$  phases were published a few years ago [87]. Very recently, Chen et al. used first principles methods to study the variations in lattice constants in mullite [88]. This scarcity of detailed theoretical work on mullite, especially on its mechanical properties is not surprising considering the complexity and the disordered nature of its structure. Large supercells are necessary to appropriately model the mullite structure to account for the partially occupied sites. This adds considerably to the computational costs when more accurate ab initio methods are used. In mullite phases, the increased alumina content, with the associated increase in oxygen vacancies, affects their elastic state. Their elastic properties depend on the interatomic interaction and bonding configuration. Understanding how elastic properties change with alumina content and how they relate to the fundamental electronic structure is a subject of great importance if increased applications of mullite beyond the traditional use are envisioned.

## 4.2 Structural Modeling of the Mullite Phases

### 4.2.1 Construction of Supercell Models

The reported structural data for mullite phases are always presented with a listing of partially occupied sites. These occur at the  $Al_{tet}$  and  $Si_{tet}$  sites as well as at certain O sites, particularly those that bridge two Al/Si tetrahedra. As an example, Table 1 shows the experimental structural data of 3/2 mullite [89]. All the octahedral Al sites ( $Al_{oct}$ , labeled Al) are fully occupied and the tetrahedral sites (labeled Al1 and Si1) are partially occupied. The Al2 and Si2 tetrahedral sites are also partially occupied but they are disordered because of the presence of O vacancies. For the oxygen ions, the O1 and O4 are fully occupied whereas O2 and O3 are partially occupied. In any ab initio theoretical calcula-

tion, every atomic site in the structure must be precisely known as there is no such thing as half of an atom. To circumvent this difficulty, supercells based on the experimentally reported structure must be used in which a portion of the atoms at partially occupied sites are removed as a way to account for the partial occupation. This obstacle has prevented detailed electronic structure calculation on mullite systems for some time. This approach was used to build supercell models of the mullite phases before calculating the mechanical properties and electronic structures. Taking the 3/2 mullite as an example, a  $2 \times 2 \times 2$

Table 1. Experimental Structural Data of 3/2 mullite [from ref. [89]].

Chemical formula $Al_{4.5}Si_{1.5}O_{9.5}$				
Space Group PBAM (55)				
$a = 7.54336$ , $b = 7.69176$ , $c = 2.88402$				
$\alpha = 90$ , $\beta = 90$ , $\gamma = 90$				
Fractional Coordinates of Atoms				
Atom	x	y	z	occupancy
Al	0.0000	0.0000	0.0000	1.000
Al1	0.1485	0.3407	0.5000	0.525
Si1	0.1485	0.3407	0.5000	0.342
Al2	0.2610	0.2073	0.5000	0.100
Si2	0.2610	0.2073	0.5000	0.033
O1	0.3577	0.4235	0.5000	1.000
O2	0.5000	0.0000	0.5000	0.475
O3	0.4635	0.0465	0.5000	0.198
O4	0.1265	0.2197	0.0000	1.000

supercell of the experimental structure listed in Table 1 was generated first. All fully occupied sites were retained and those with partial occupations had the appropriate number of atoms to be removed. O vacancies were created by removing some O atoms that were close together such that the supercell was stoichiometric and charge neutral. The resulting 126-atom supercell for 3/2 mullite consists of 36 Al, 12 Si, and 78 O atoms. There are a

number ways to remove atoms from the partially occupied sites. So, 20 such initial models with different possible atomic configurations were constructed. The same strategy was followed to construct the supercell models for the other mullite phases but with different sizes as demanded by the partial occupation factor and the stoichiometric molecular formula unit for that particular phase. For the 2/1 mullite model, a  $1 \times 1 \times 5$  supercell was used based on experimental data [90] and the supercell models consisted of 24 Al, 6 Si, and 48 O for a total of 78 atoms. As there is no measured structural data available for the 4/1 mullite so far, a  $2 \times 1 \times 3$  supercell of 2/1 mullite was used as the initial starting point and adjusted the number of each type of atom to remove to achieve the correct stoichiometric ratios. The supercell models of 4/1 mullite consisted of 32 Al, 4 Si, and 56 O for a total of 92 atoms. For the 9/1 mullite, a  $2 \times 2 \times 4$  supercell of experimental structural data of a phase with high alumina content [91] which is close to the 9/1 mullite was used. The supercell models of 9/1 mullite consist of 90 Al, 5 Si, and 145 O for a total of 240 atoms. All 20 supercell models for each mullite phase were fully relaxed (allowing atomic positions, volume and shape to adjust) using the Vienna ab initio simulation package (VASP) [1–3] with high accuracy. Projector augmented wave (PAW) potentials [34, 35] were used as supplied in the VASP package. A high cutoff energy of 700 eV was used to ensure the accuracy and also considering the change in the volume while relaxing the mullite models. A relatively high accuracy was set for the ground state electronic convergence limit ( $10^{-7}$  eV) and a small tolerance for the ionic relaxation convergence ( $10^{-5}$  eV/Å) was implemented. Mullite models with different alumina content have different cell sizes, so different sets of k points considering respective cell parameters were used. Out of the 20 supercell models, the model with the lowest total energy was taken as the representative model of that mullite phase and was subsequently used for calculation of the other physical properties. Fig. 1 shows the fully relaxed final representative model of the all four mullite

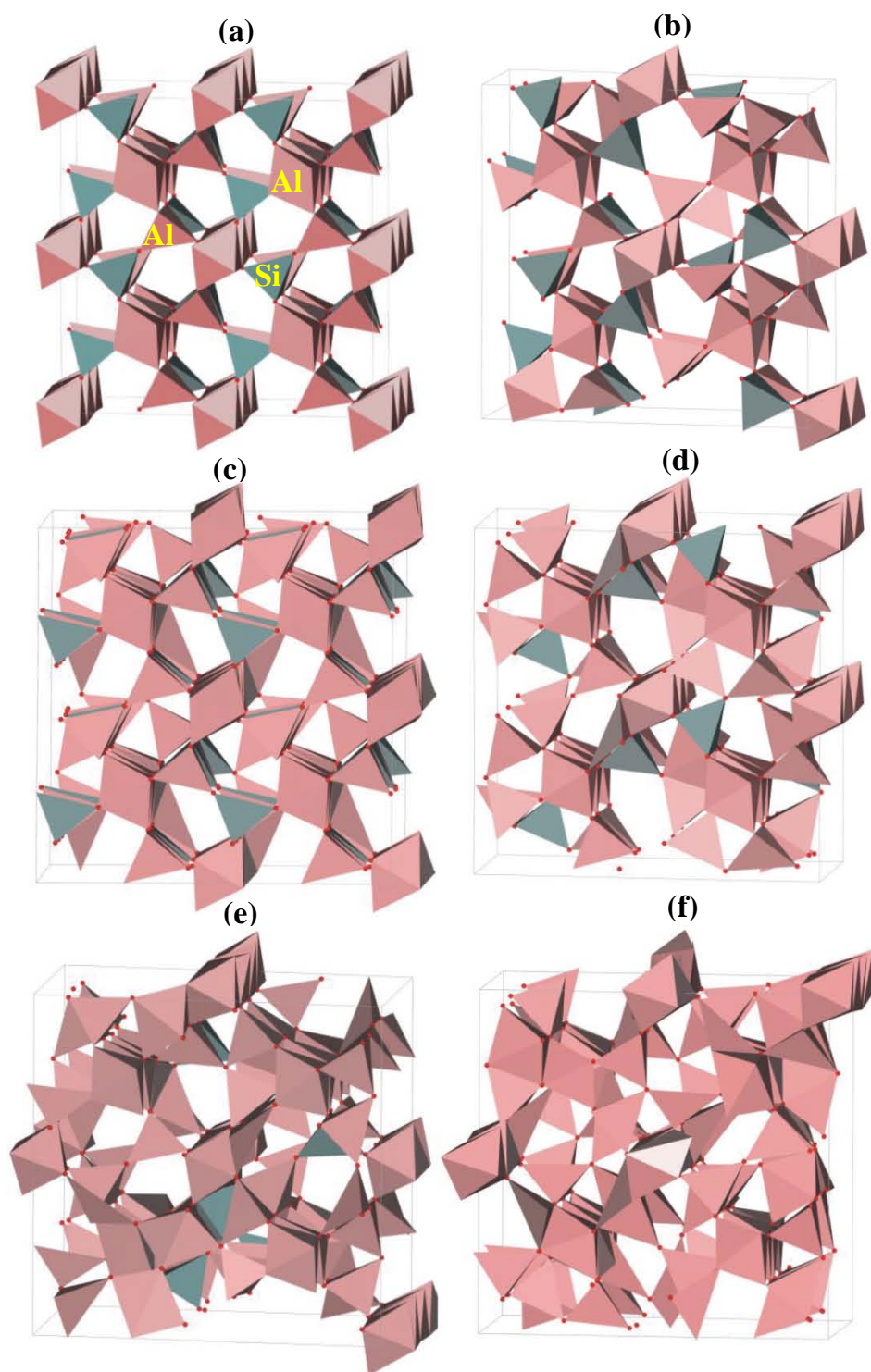


Figure 1. Relaxed supercell models of mullite phases including sillimanite and  $\iota$ - $Al_2O_3$ . (a) sillimanite, (b) 3/2 mullite, (c) 2/1 mullite, (d) 4/1 mullite, (e) 9/1 mullite and (f)  $\iota$ - $Al_2O_3$ . Al and Si polyhedra are presented with different shading.

phases. For comparison, the structures of a  $2 \times 2 \times$  supercell of sillimanite (128 atoms) and  $\iota$ - $Al_2O_3$  are also presented. As can be seen, the structures of the 3/2 mullite and sillimanite are quite similar.  $Al_{oct}$  in the 3/2 mullite are almost undisturbed and aligned along the c-axis as in sillimanite. Most of the Al/Si tetrahedral configurations are the same as in sillimanite whereas the rest, especially those close to the O vacancies are slightly displaced away from the vacancy site, thus breaking that particular alignment along the c-axis. Some of the O atoms in 3/2 mullite are bonded with three Al/Si tetrahedra (T) in the form of  $T_3O$  triclusters. As the x increases, the mullite structures as shown in figure 1 become more and more complex and disordered.

The end members of the mullite series, sillimanite ( $x = 0$ ) and  $\iota$ - $Al_2O_3$  ( $x = 1$ ), were handled differently. The measured structural data for sillimanite[54] was fully relaxed using the same computational parameters before any physical property calculations were done. For the case of  $\iota$ - $Al_2O_3$  however, it is a relatively unknown phase and no measured structural data were available even though multiple experiments have pointed to its existence; the earliest report was more than 50 years ago [5–7, 50, 92]. The some of the calculated results of  $\iota$ - $Al_2O_3$  presented here as part of the mullite is to study the trend of mullite physical properties in relation to two end members, sillimanite and  $\iota$ - $Al_2O_3$ . The details of  $\iota$ - $Al_2O_3$  will be discussed in chapter 5.

#### 4.2.2 Analysis of Mullite Models

The best way to examine the disorder in the structure of mullite is to analyze its radial pair distribution function (RPDF). Fig. 2 shows the calculated RPDF plots up to a radial distance of 8 between all pairs of atomic types in four mullite phases and the two end members sillimanite and  $\iota$ - $Al_2O_3$ . To minimize the effects of different supercell sizes in these phases, the intensities of all the plotted RPDF are normalized to the unit cell size.

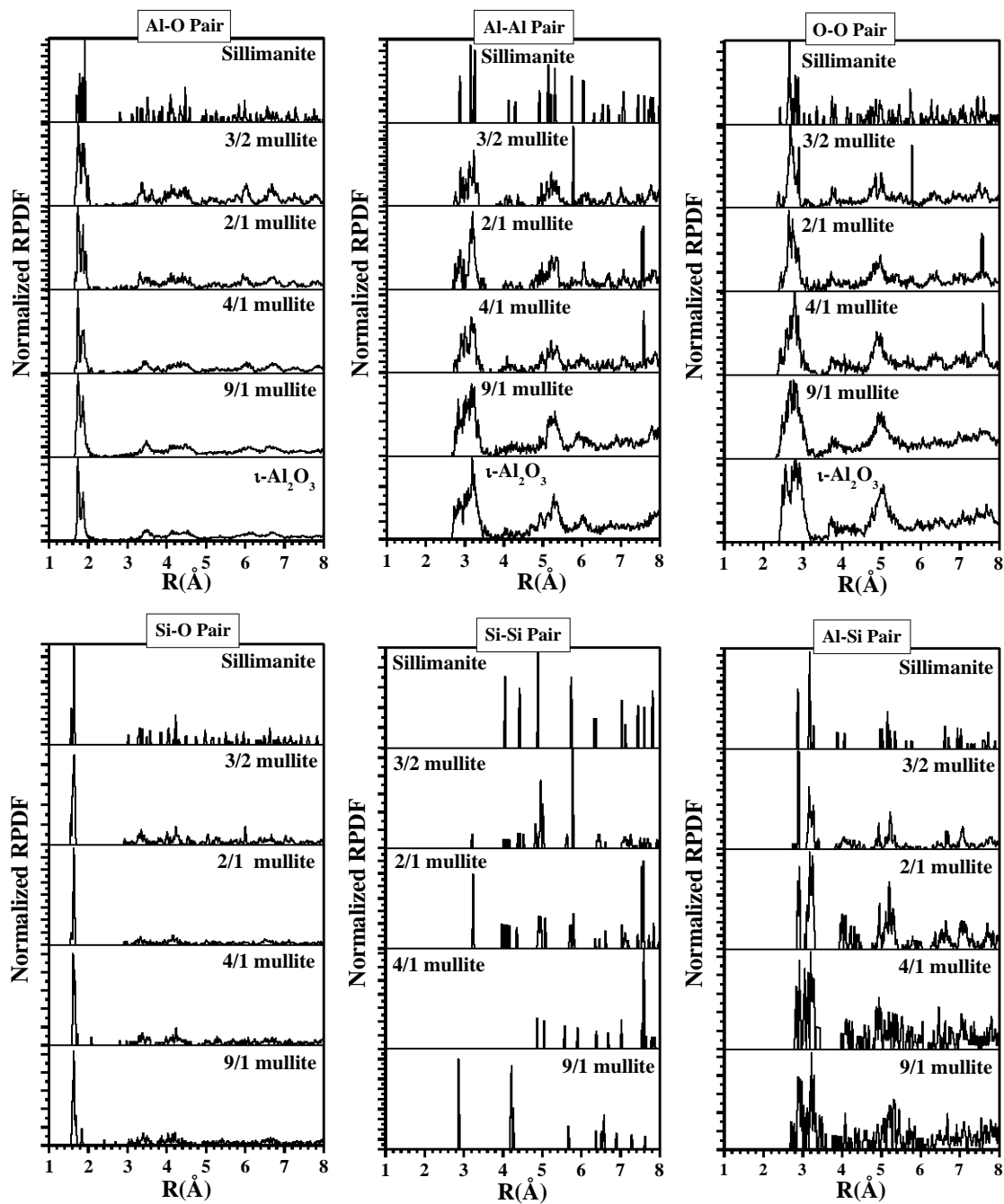


Figure 2. Radial pair distribution function (RPDF) of Al-O, Al-Al, O-O, Si-O, Si-Si, and Al-Si pairs in mullite phases including sillimanite and iota-alumina. All the RPDF values are normalised to same area

The peaks below 2.0 correspond to nearest neighbor (NN) pairs in the structure. As can be seen, sillimanite has distinct NN peaks in its RPDF reflecting its perfect crystallinity with Al-O at 1.71 Å, 1.79 Å, 1.86 Å, and 1.91 Å and Si-O bonds at 1.57 Å and 1.63 Å respectively. It should be noted that even in crystalline sillimanite the NN bond lengths for the octahedral and tetrahedral bonding are not all the same [87]. Therefore, the NN peaks for sillimanite in Fig. 2 correspond to the combination of  $Al_{tet}$ -O and  $Al_{oct}$ -O bond distances. In other mullite phases this crystalline short range order (SRO) becomes much weaker and the sharp peaks start to broaden. The first group of peaks representing the NN Al-O and Si-O bonds are the most important peak features. As the alumina content in the structure increases, the NN peaks start to broaden but still display distinct peak features showing the presence of SRO from Al octahedra and Al/Si tetrahedra. At the larger radial distance, the Al-O and Si-O RPDF are quite broadened with increased alumina content. This broadening is also present for the Al-Al and O-O pairs as well. They exhibit broad peak features similar to those in amorphous solids with no long range order. In the mullite phases, the Si-Si and Al-Si RPDF have some relatively sharp peaks, including those with high alumina content, indicating that certain longer range order persists in the distribution of Si tetrahedra. The RPDF for  $\iota$ - $Al_2O_3$  requires special comments. This is a silica free phase end member of the mullite series so only the RPDF for Al-O, Al-Al, and O-O are shown. Other than the NN Al-O peaks at 1.73 Å and 1.86 Å the Al-Al pairs have broad peaks centered at 2.83 Å, 3.19 Å, and 5.28 Å and the O-O pairs have broad peaks at 2.54 Å, 2.82 Å, and 5.01 Å. These features indicate that  $\iota$ - $Al_2O_3$  is even more disordered than the other mullite phases.

The increase in alumina content in the mullite structure is at the cost of silica. The Si-O bonds are shorter than the Al-O bonds, so increasing the number of Al tetrahedra causes an overall increase in the NN bond lengths which leads to changes in the lattice

parameters. It can be argued that changes in the lattice parameters due to increasing Al tetrahedra should have a definite pattern. But the presence of O vacancies and the displacement of the Al/Si tetrahedra from the vacancies makes it more complicated. The Table 2, consists of the lattice parameters, volume, and density of the relaxed mullite phase structures including the two end members, sillimanite and  $\iota$ - $Al_2O_3$ . These data are scaled back to the crystalline unit cell. The c axis magnitude in the mullite phases and  $\iota$ - $Al_2O_3$  are presented on equal footing with that of sillimanite. As can be seen, apart from sillimanite, none of the structures are perfectly orthorhombic. A slight distortion in the lattice is normal because mullite structures are complex and disordered. The variations in lattice constants a, b, and c in mullite are also displayed in Fig. 3 (a). Generally speaking, a increases with alumina content but in  $\iota$ - $Al_2O_3$  it is slightly smaller than in 9/1 mullite. The magnitude of b does not show any specific pattern. It decreases rapidly at 3/2 mullite and then increases slightly up to 4/1 mullite while sillimanite has the largest value for b overall. At 4/1 mullite, a and b are almost equal so that it appears as a pseudo tetragonal phase. In general, c increases slowly with increasing alumina content without any specific pattern. It decreases slightly at 4/1 mullite but increases afterwards. These trends are generally consistent with the early observations by Cameron [50]. It is instructive to compare some of these trends with the experimental observations. Fischer et al. (1994) [91] and Rehak et al. (1998) [65] plotted the lattice constants with molar percentage of alumina content in the mullite structure. Their data are similar to each other and show a linear increase in a with alumina content and a nonlinear decrease (increase) in b (c). These trends are qualitatively reproduced by simulated structures. The small difference between their data and the present calculation can be attributed to several factors. First, the present calculations are for mullite models at zero temperature and pressure, or the theoretical equilibrium structure, whereas the experimental data are usually at room temperature and under different

conditions. Second, the experimental samples are far more difficult to precisely characterize. Interestingly, their fitted magnitudes for a and b cross at 78% molar content of alumina which is close to the 4/1 mullite (80% molar alumina). For the 4/1 mullite, calculated a and b magnitudes are 7.6010 Å and 7.5989 Å respectively. The small difference in a and b indicates that the exact crossing could occur at a composition slightly preceding the 4/1 mullite, which is consistent with the measured data. Present calculated results also agree with the only other first-principles simulation on mullites in ref. [42] for  $x = 0.125, 0.250,$  and  $0.375$ . The calculated values for the volume and density of the mullite structures are

Table 2. Relaxed volume and lattice constants ( Å ) of mullite models scaled back to the unit cell.

Crystal	Volume(3)	a	b	c	$\alpha$	$\beta$	$\gamma$
Sillimanite	325.3389	7.4474	7.6014	5.7469	90.0000	90.0000	90.0000
3/2 mullite	329.6418	7.5385	7.5622	5.7824	90.0000	90.0000	89.9669
2/1 mullite	332.0738	7.5497	7.5812	5.8020	89.9456	89.7920	89.7836
4/1 mullite	334.4706	7.6010	7.5989	5.7911	89.9692	90.0425	90.5982
9/1 mullite	335.5752	7.6445	7.4532	5.8912	90.2536	90.0719	91.2518
$\iota$ - $Al_2O_3$	337.8136	7.6384	7.4781	5.9142	89.9468	89.9463	90.3470

listed Table 2 and are also plotted in Fig. 3 (b). The changes in volume and density with x are relatively smooth compared to the changes in the lattice constants. The density vs. x curve is almost linear from sillimanite to 9/1 mullite before there is a much larger decrease from 9/1 mullite to  $\iota$ - $Al_2O_3$ , the ultra-low density phase of alumina.

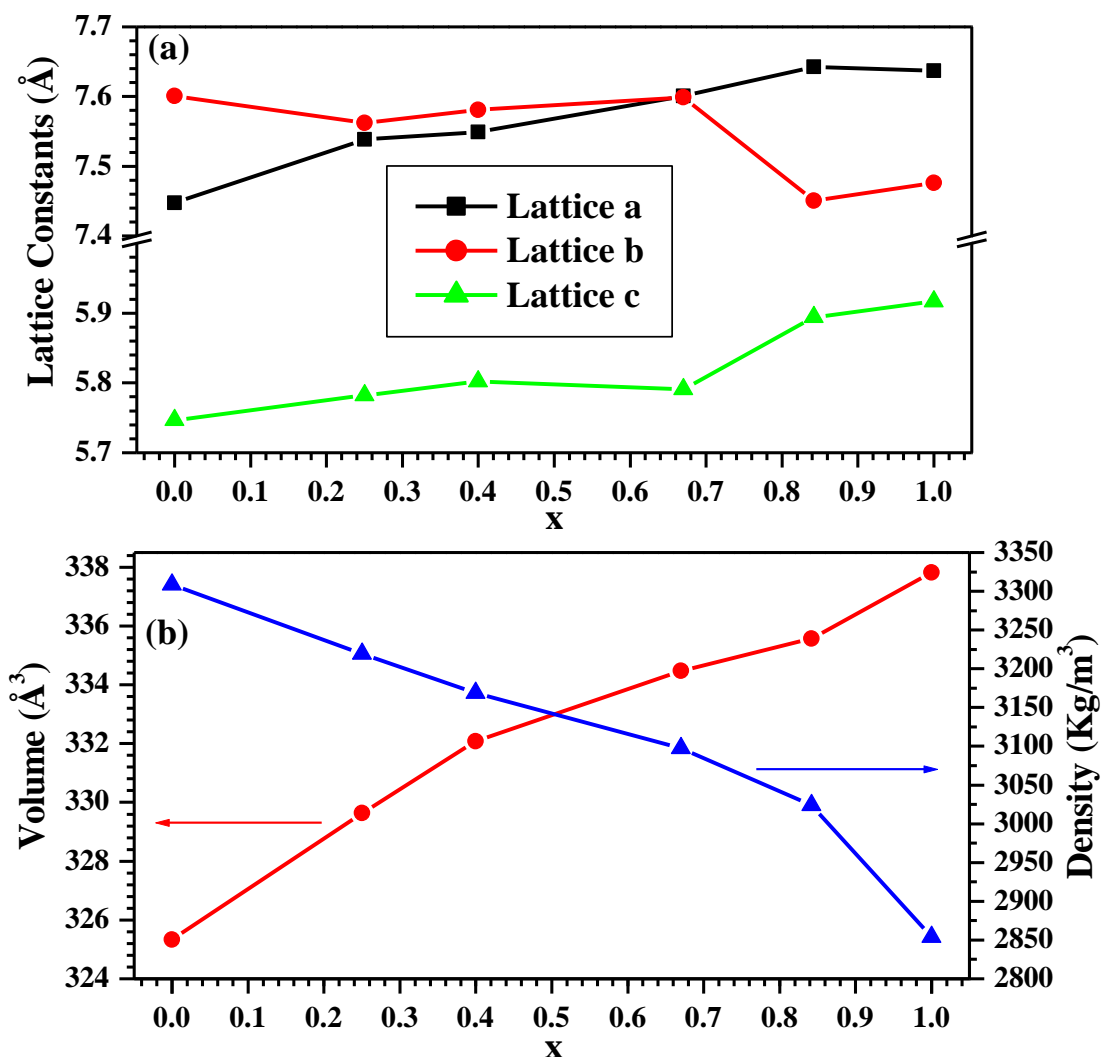


Figure 3. Variation of lattice constants (a) and volume (b) with  $x$  in the mullite series. Lines joining data points illustrate the general trend with  $x$ .

### 4.3 Mechanical Properties of the Mullite Phases

#### 4.3.1 Elastic Stiffness Constants and Bulk Mechanical Properties

Understanding the elastic properties of technologically relevant materials is important for their application and advancement. Elastic stiffness constants are critical for assessing how a solid responds under strain within the elastic limit. The elastic tensor enables the evaluation of bulk mechanical properties and sound velocities in different directions

which can be directly checked with laboratory measurements. The propagation of acoustic phonons and the measurement of minerals in geological deposits on Earth are subjects of great importance in the study of seismic activities [93]. In the present study for elastic properties calculation of mullite, the strain-stress analysis approach has been used on the supercell models that were constructed. The method of  $C_{ij}$  calculations and derivations of polycrystalline bulk properties are described already in chapter 3.

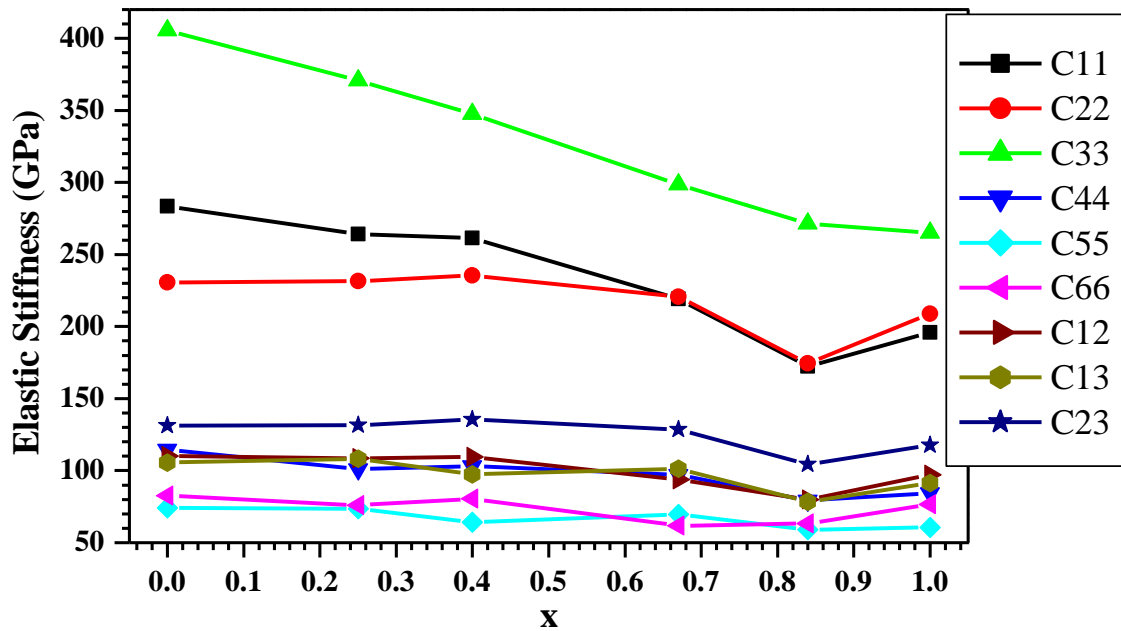


Figure 4. Calculated elastic constants of mullite phases in GPa. Scattered symbols represent  $C_{ij}$  data for a particular phase and lines joining them show a general trend.

Calculated elastic stiffness constants for the mullite phases, including sillimanite and  $\iota$ - $Al_2O_3$ , are listed in Table 3. The same data are plotted in Fig. 4 for visual analysis of the trends and for easy comparison among different mullite phases. Calculated elastic tensor data shows that the mullite structural models are elastically anisotropic, which can

be explained by simple geometric considerations. The significantly larger  $C_{33}$  is derived from the fact that the  $Al_{oct}$  and Al/Si tetrahedral chains are aligned along the c-axis. As alumina content in the mullite series increases, the stiffer Si tetrahedra are progressively replaced by Al tetrahedra, thereby reducing the structure's stiffness. Furthermore, because some Al/Si tetrahedra deviate slightly from the site of an O vacancy the alignment of the Al/Si tetrahedra chain along the c-axis is broken. This pattern increases in proportion to the alumina content and is the main reason for the almost linear decrease in  $C_{33}$  with x. The longer  $Al_{oct}$ -O bonds which lie in the (001) plane are tilted towards the [010] direction; and the two shorter  $Al_{oct}$ -O (O1 and O2) bonds are tilted towards the [100] direction resulting in a larger  $C_{11}$  than  $C_{22}$ . The tetrahedral Al/Si units have two relatively shorter bonds with O in the (001) plane. One bond is tilted towards the [100] direction and the other is slightly tilted towards [010]. The remaining two longer tetrahedral Al/SiO bonds have only a very small component in the (001) plane. Therefore, on average, Al/Si tetrahedra also tend to make the [100] direction stiffer than the [010] direction. As alumina content increases, the bond orientations in the Al octahedra do not change much, but its effect on the Al/Si tetrahedral bonding pattern can be quite significant. When an Al atom replaces a Si atom, the average bond length to the O atoms increases. The increased O3 vacancy also increases the disordered pattern of Al/Si tetrahedra and thus the orientations of some bonds change. All these geometric rearrangements in the structure result in the decrease of  $C_{11}$  with only a slight change in  $C_{22}$ . For 4/1 mullite, where the structure is pseudo-tetragonal,  $C_{11}$  is almost equal to  $C_{22}$  as expected. Beyond 4/1 mullite at higher values of x,  $C_{22}$  is larger than  $C_{11}$  in line with changes in the lattice constants. For 9/1 mullite  $C_{22}$  is slightly larger than  $C_{11}$  and this difference increases at  $\iota$ - $Al_2O_3$ . Fig. 4 shows the trends for the other elastic coefficients and they are much smaller than  $C_{11}$ ,  $C_{22}$  and  $C_{33}$ . Among the shear stiffness constants  $C_{44}$ ,  $C_{55}$ , and  $C_{66}$ , the value of  $C_{44}$  is

Table 3. Calculated elastic stiffness constants of mullite phases (GPa).

Crystal		$C_{11}$	$C_{22}$	$C_{33}$	$C_{44}$	$C_{55}$	$C_{66}$	$C_{12}$	$C_{13}$	$C_{23}$
Sillimanite		283.5	230.7	405.4	114.5	74.2	82.6	110.1	105.6	131.3
3/2 mullite		265.3	233.8	373.6	104.3	73.6	82.3	106.9	115.9	138.8
2/1 mullite		261.4	235.5	347.5	103.2	64.3	80.6	109.4	97.6	135.3
4/1 mullite		219.2	220.7	298.6	97.1	69.5	61.8	93.9	101.2	128.5
9/1 mullite		172.3	174.6	271.3	79.3	59.2	63.3	79.9	78.5	104.2
$\iota$ - $Al_2O_3$		196.0	208.8	264.9	84.3	60.6	76.6	97.0	91.4	117.7
Measured data from literatures.										
2/1	a	279.5	234.9	360.6	109.6	74.94	79.9	103.1	96.1	135.6
mullite	b	291.2	232.9	352.1	110.3	77.4	79.9	112.9	96.1	121.9
2.5/1	c	281.9	244.2	263.6	111.7	78.2	79.2	105.1	100.3	142.3
mullite	d	280.0	245.0	362.0	111.0	78.1	79.0	105.0	99.2	135.0

a Ref. [81]; b Ref. [78]; c Ref [79]; d Ref. [66].

distinctively larger in all mullite phases including sillimanite and  $\iota$ - $Al_2O_3$ . This can be explained by viewing the atomic structures of the supercell projected on three different planes. The atomic arrangement in the (100) plane appears to be more uniform than in the (010) and (001) planes. This uniform distribution of atoms gives rise to a relatively higher stability in the (100) plane. When alumina content and O vacancies increase in the structure, this uniformity is somewhat distorted resulting in a modest decrease of  $C_{44}$  with x. Furthermore,  $C_{66}$  is larger than  $C_{55}$  in all phases except in 4/1 mullite. So the (001) plane should be more stable under shear deformation than the (010) plane. Supercell projection on the (010) plane reveals that the atoms form layered structures parallel to the c-axis, which could result in a smaller  $C_{55}$ . In addition, Al octahedra stabilized by Al/Si tetrahedra also contribute to a larger  $C_{66}$  than  $C_{55}$ . The 4/1 mullite appears to be an exception although the difference between  $C_{55}$  and  $C_{66}$  is quite small. Among the group of off diagonal elastic coefficients ( $C_{12}$ ,  $C_{13}$ , and  $C_{23}$ )  $C_{23}$  is significantly larger than the other two in all mullite phases. The larger value of  $C_{23}$  implies that the atomic configuration and bonding in directions [010] and [001] are more strongly interrelated than

in the other two cases ( $C_{12}$  and  $C_{13}$ ). Interestingly,  $C_{12}$  and  $C_{13}$  are almost equal in all cases and there is no particular trend observed with increasing  $x$ . There are reported

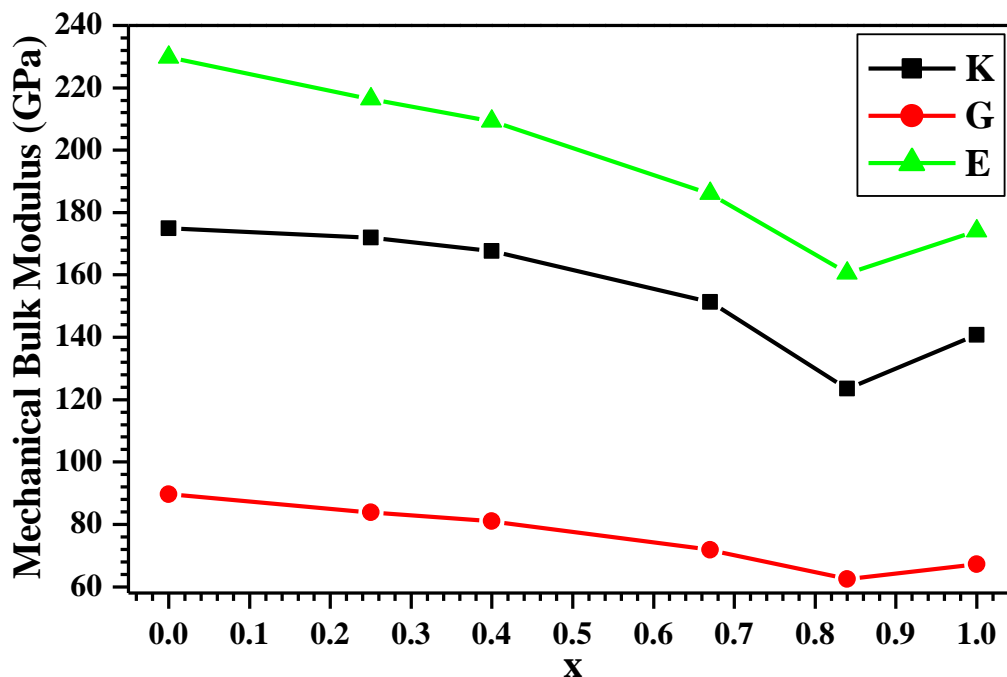


Figure 5. Calculated mechanical bulk properties of mullite phases in GPa

experimental data (see Table 3) on the elastic stiffness constants of single crystal 2/1 mullite [78, 81] and 2.5/1 mullite [66, 79]. In the 2/1 mullite, the reported values for  $C_{11}$ ,  $C_{33}$ ,  $C_{12}$ , and  $C_{23}$  from the two sets of measurements are somewhat different. Generally speaking, calculated  $C_{11}$ ,  $C_{33}$ ,  $C_{44}$ ,  $C_{55}$ , and  $C_{12}$  are quite close to those measured ones with  $C_{22}$ ,  $C_{66}$ ,  $C_{13}$ , and  $C_{23}$  in very good agreement. The minor differences are understandable because the calculation is based on LDA theory and is applied to a supercell model of limited size. Most likely, the samples used in the experimental measurements invariably contain impurities, porosity, and defects and therefore cannot be easily characterized. The

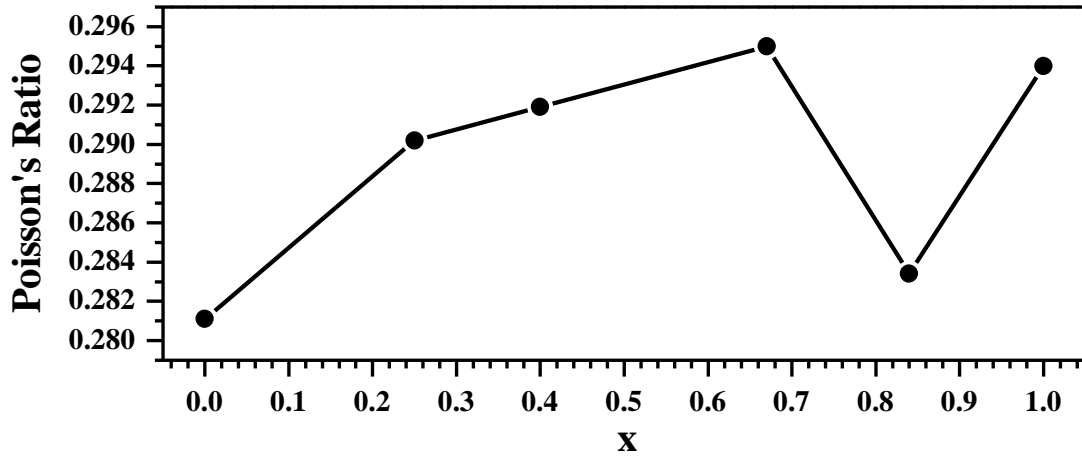


Figure 6. Calculated Poisson's ratios of mullite phases.

measured elastic stiffness constants for the other mullite phases are available so far. From

Table 4. Calculated and measured bulk mechanical properties of mullite phases (GPa).

Crystal	K	G	E	$\eta$	
Sillimanite	174.9	89.7	229.7	0.281	
3/2 mullite	173.2	84.2	217.4	0.290	
2/1 mullite	167.6	81.0	209.2	0.292	
4/1 mullite	151.3	71.8	186.0	0.295	
9/1 mullite	123.5	62.5	160.5	0.283	
$\iota$ - $Al_2O_3$	140.8	67.3	174.1	0.294	
Measured data from literatures.					
Mullite phases	Ref.				
2/1 mullite	35	166.5			
3/2 mullite	34	173.9	89.5	229.1	0.28
2/1 mullite	32	169.2	87.86	224.7	0.279
2.5/1 mullite	33	173.5	88.0	225.9	
3/2 mullite	24			202/195	
Mullite	29			143	
3/2 mullite	23			246	
Mullite	16			194	0.276

the calculated elastic stiffness coefficients, bulk mechanical properties: bulk modulus (K), shear modulus (G), Youngs modulus (E) and Poissons ratio ( $\nu$ ) can be obtained and they are listed in Table 4 together with some measured values from the literature. Fig. 5 display the calculated values of K, G, and E as a function of  $x$ . They all decrease with increasing  $x$  with K and E decreasing more sharply beyond 4/1 mullite. This is expected because the presence of a large number of O vacancies at large  $x$  makes the structure weaker against volume compression. Interestingly, there is a slight increase in K, G, and E in  $\nu$ - $Al_2O_3$  after 9/1 mullite. It should be mentioned that the modeling of 9/1 mullite is far more difficult than the other mullite phases due to the small silica content. In particular, the void space that appears due to the large number of O vacancies is difficult to characterize. This can lead to a greater degree of uncertainty in the structure and the properties that depend on it. So, between 9/1 mullite and  $\nu$ - $Al_2O_3$ , a change in mechanical bulk properties is expected to be different due to such fluctuations. In Fig. 6, the variation of Poissons ratio  $\nu$  with  $x$  is displayed. The variation in  $\nu$  tends to be more irregular than for the other bulk properties. It increases with  $x$  up to 4/1 mullite and then at 9/1 mullite, there is a sudden drop in  $\nu$  before it rises again to almost the same level as in 4/1 mullite at  $\nu$ - $Al_2O_3$ . This feature is in line with a large change in the bulk properties at 9/1 mullite. However, the differences in  $\nu$  in Fig.6 are highly magnified with the difference between maximum (in 4/1 mullite) and minimum (in sillimanite) only being 0.014. A comparison of calculated and measured bulk mechanical properties of mullite is presented in Table 4. There are large variations among the measured data presumably due to sample differences of various origins. Most of the reported measurements did not even specify the composition (indicated simply as mullite in Table 4) so that only a qualitative comparison is possible. It is worth to emphasize on the 3/2 and 2/1 mulites where complete sets of measured data were provided and where they are more consistent with each other [78, 80]. Calculated K of 173.2 GPa for the 3/2 mullite

is in excellent agreement with the measured value of 173.9 GPa obtained by Ledbetter et al. [80] on polycrystalline void free samples. The measured values for  $G$ ,  $E$ , and  $\eta$  are also very close to calculated data. Similarly, the calculated value for  $K$  (167.6 GPa) for 2/1 mullite is also in good agreement with the measured value of 169.2 GPa from Hildmann et al. [78] obtained on single crystal 2/1 mullite using acoustic resonance spectroscopy. The calculated values for  $K$ ,  $G$ , and  $E$  are slightly smaller than the quoted experimental values whereas the calculated Poissons ratio of 0.290 (0.292) for 3/2 (2/1) mullite is slightly larger than the measured value of 0.28 (0.279). It is interesting to compare the measured values of  $K$ ,  $G$ ,  $E$  for 3/2 mullite [80] [34] and 2/1 mullite [78] with those obtained by Palko et al.[79] on the 2.5/1 mullite at room temperature using Brillouin spectroscopy. These three sets of data are actually quite close to each other with no correlation to  $x$ . This underscores that the accuracy currently obtainable in experimental determinations of the bulk mechanical properties is still not sufficient to delineate the fine differences between mullites. Measured mechanical properties for other mullite phases are not available so far and calculated values for these mullite phases can be treated as reasonable predictions.

#### 4.3.2 Sound Velocity in Different Planes

Because mullite is also considered to be an important mineral, it is imperative to obtain the sound velocities once their elastic tensors are obtained. In fact, some of the experimental values for elastic constants of mullite discussed above were obtained from the sound velocity measurements [66, 79]. The elastic wave velocity in mullite in specific directions has been calculated by using the Christoffel wave equation [94, 95].

$$\rho v^2 u_i = C_{ijkl} l_j l_k u_l \quad (4.2)$$

In Eqn. (4.2),  $\rho$  is the density of the solid,  $v$  is the elastic wave velocity,  $C_{ijkl}$

is a more general form for writing the elastic stiffness tensor  $C_{ij}$  in Voigt notation for anisotropic media,  $l_j$  and  $l_k$  represent the direction of propagation of the elastic wave, and  $u_l$  is the polarization of the wave. For each direction, Eqn. (4.2) has three solutions corresponding to three mutually orthogonal wave propagations, one longitudinal and two transverse. The sound velocities are calculated for all four mullite phases along with sillimanite and  $\iota$ - $Al_2O_3$  as well. In Fig. 7, the calculated sound velocity distributions of the 3/2 mullite in the (001), (100), and (010) planes are displayed. In each plane, the outer envelope defines the longitudinal component and the two inner envelopes define the transverse components of the sound velocity. In the (001) plane (Fig. 7(a)), the longitudinal velocity along the [100] direction is slightly larger than along the [010] direction because  $C_{11}$  is larger than  $C_{22}$ . However, compared with the other two planes, the longitudinal velocity distribution in the (001) plane is more isotropic. The larger anisotropy of the longitudinal velocity in the (100) plane (Fig. 7(b)) and the (010) plane (Fig. 7(c)) originates from the significantly larger values of  $C_{33}$  over  $C_{11}$  and  $C_{22}$ .

Because the sound velocity is proportional to the elastic stiffness, it is used as a tool to experimentally measure the stiffness of a solid in a particular direction. For example, in the (001) plane of 3/2 mullite, the maximum longitudinal velocity of 9195.1 m/s is along a direction  $24^\circ$  from the a-axis and the minimum velocity of 8456.8 m/s is along the b-axis. This implies that the structure is stiffer along the former direction and softer along the b-axis. Similarly, in the (100) plane, the maximum longitudinal velocity of 10768.2 m/s is along the c-axis and the minimum velocity is along the b-axis. Finally, in the (010) plane, the maximum velocity of 10768.2 m/s is along the c-axis and the minimum velocity is 9073.5 m/s along a direction  $78^\circ$  off the c-axis. For the transverse components of sound velocity in mullites, the patterns are more complicated. The distribution is quite anisotropic in all three planes, (001), (100), and (010). It is interesting to see how the sound velocities

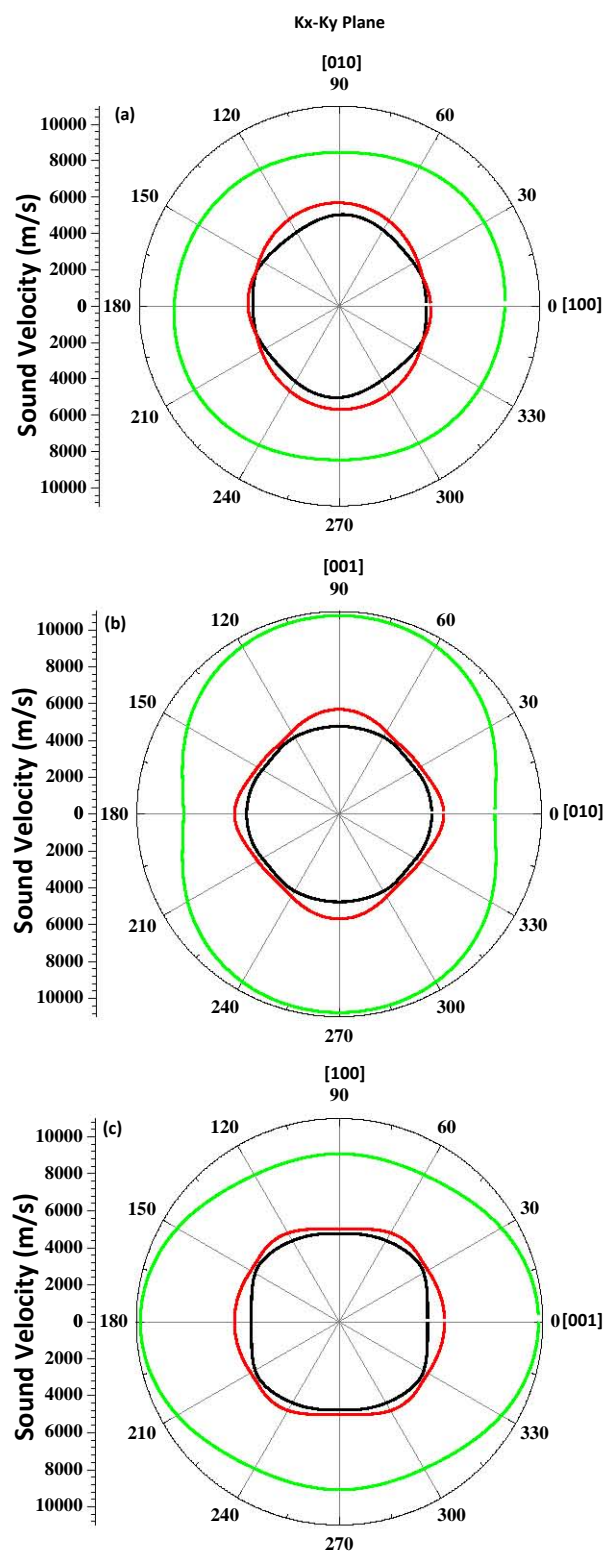


Figure 7. Calculated sound velocities (m/s) in  $3/2$  mullite in: (a) (001) plane; (b) (100) plane; (c) (010) plane.

Figure 7.

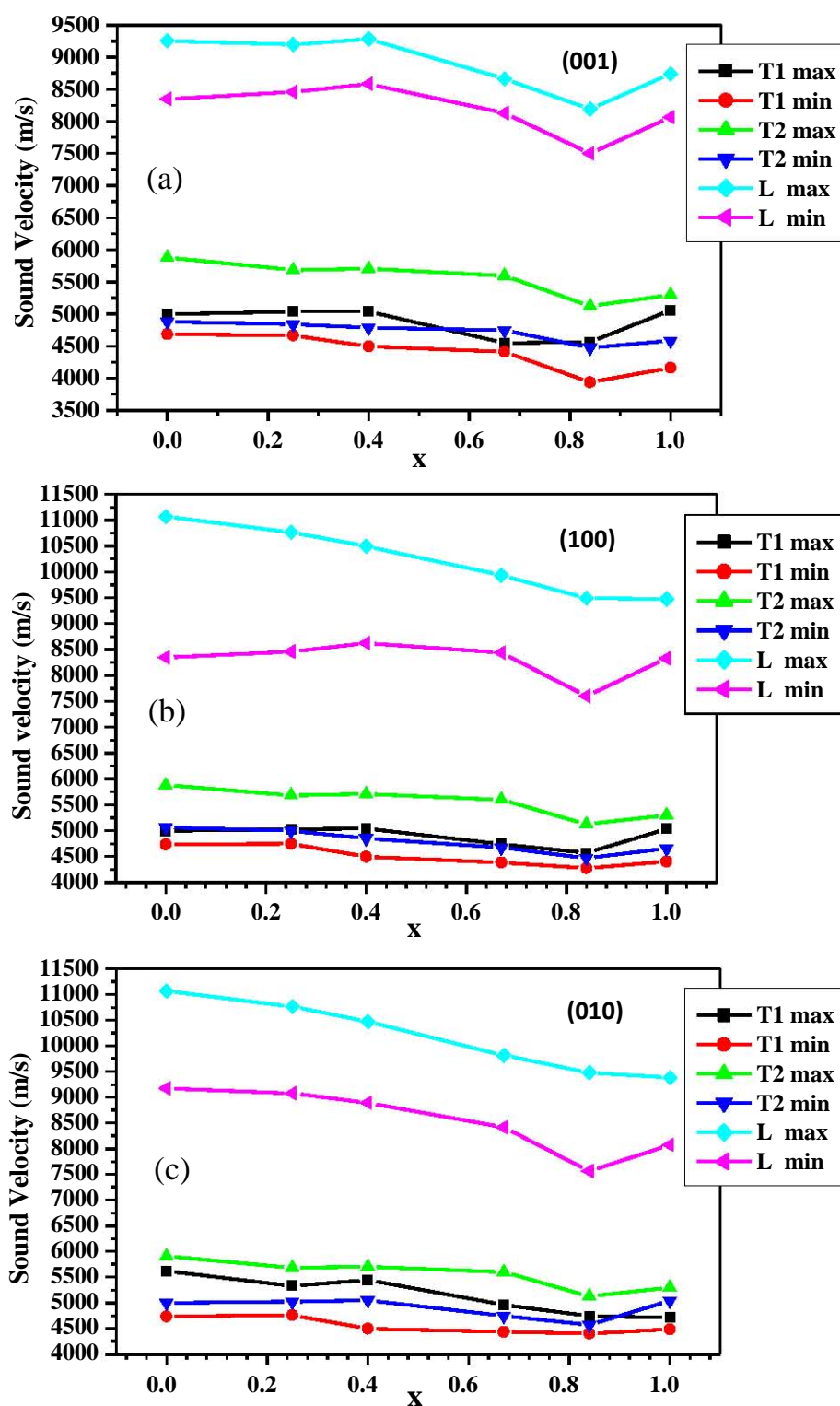


Figure 8. Calculated maximum and minimum sound velocity (m/s) in mullite phases in: (a) (001) plane; (b) (100) plane; and (c) (010) plane. T for the transverse modes and L for the longitudinal mode.

Figure 8.

in different planes vary when alumina content in the mullite series increases. This is displayed in Fig. 8 for the maximum and minimum sound velocity components in the (001), (100), and (010) planes and it can reveal the degree of elastic anisotropy in the mullite structures. In all three planes, sillimanite has the maximum anisotropy for the longitudinal velocity. As  $x$  increases, the longitudinal anisotropy decreases. At the 9/1 mullite, there is a slight increase but the trend reverses at  $\iota$ - $Al_2O_3$ . In summary, among the three planes, the (100) plane is the most anisotropic and the (001) plane is the least anisotropic. On average, there is an overall decrease in the value of the transverse components of sound velocity with increasing  $x$ . All mullite phases have an anisotropic distribution of the transverse components in each plane but do not show a definite pattern with increasing  $x$  as in the longitudinal case. There are no direct experimental data available on directionally dependent sound velocities to compare with this calculated data but they can be inferred from reliable elastic constant measurements.

## 4.4 Electronic Structure of Mullite Phases

### 4.4.1 Band Structure and Density of States

The electronic structure and bonding are at the heart of all physical properties of materials including the mechanical and elastic properties. The electronic structure of the mullite phases are studied using the OLCAO method [4, 96]. In the present calculation, a full basis set is employed to obtain the self-consistent potentials, band structures, and density of states (DOS) all using the local density approximation (LDA). The full basis set consists of atomic orbitals of 1s, 2s, 2p, 3s, 3p, 3d, 4s, and 4p for Al and Si; and atomic orbitals of 1s, 2s, 2p, 3s, and 3p for O. For effective charge and bond order calculations, a more localized minimal basis set that includes only the occupied orbitals based on the Mulliken scheme is used [38]. For the case of the optical properties calculations an extended

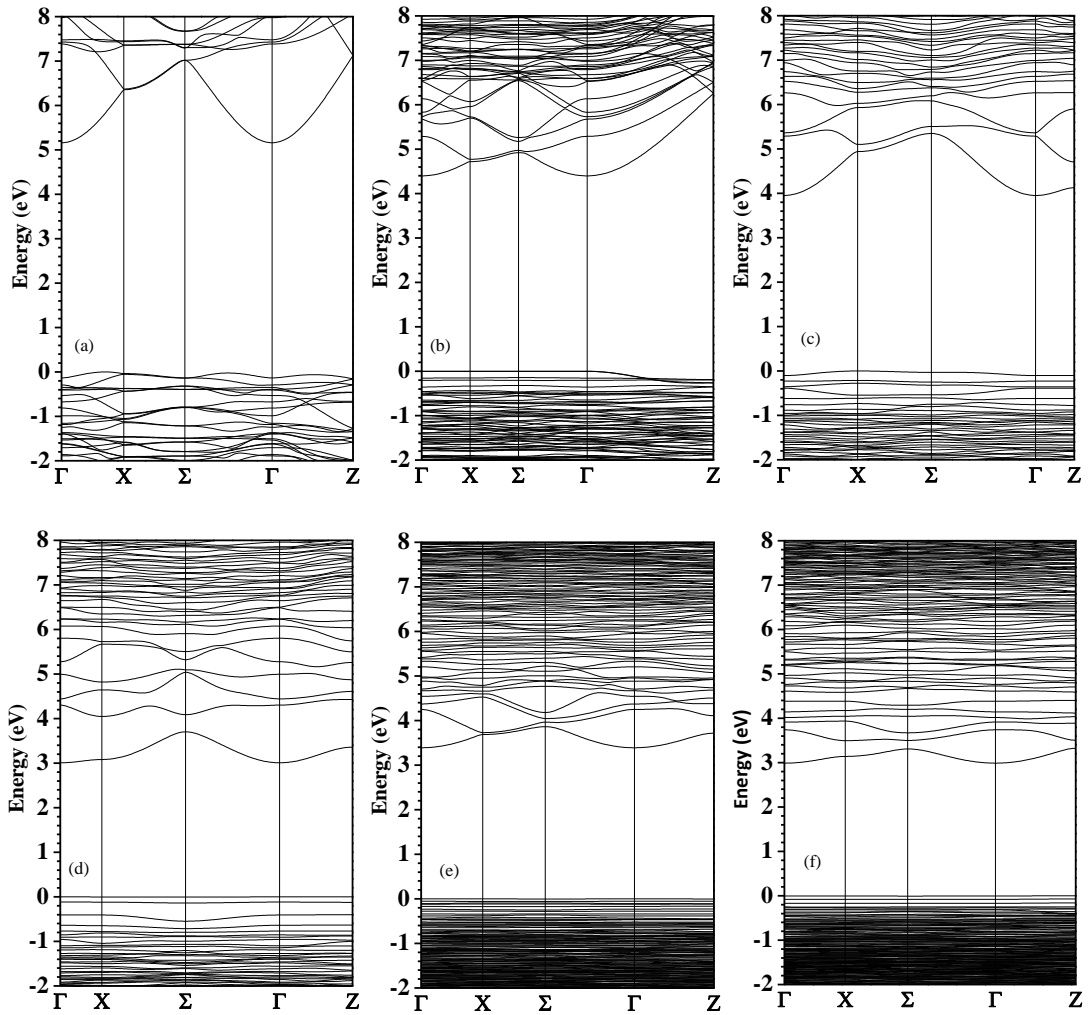


Figure 9. Calculated band structures of mullite along the high symmetry points in the Brillouin zone: (a) Sillimanite; (b) 3/2 mullite; (c) 2/1 mullite; (d) 4/1 mullite; (e) 9/1 mullite; (f)  $\iota$ - $Al_2O_3$ .

basis set was used. This basis set includes one further shell of orbitals in addition to the full basis set to improve the representation of the higher energy unoccupied states. The calculated band structure of the four mullite phases and the two end members, sillimanite and  $\iota$ - $Al_2O_3$ , are presented in Fig.9. They are all large band gap insulators with a direct band gap at the Brillouin zone center  $\Gamma$ . The variation of the band gap with x is shown in Fig. 10

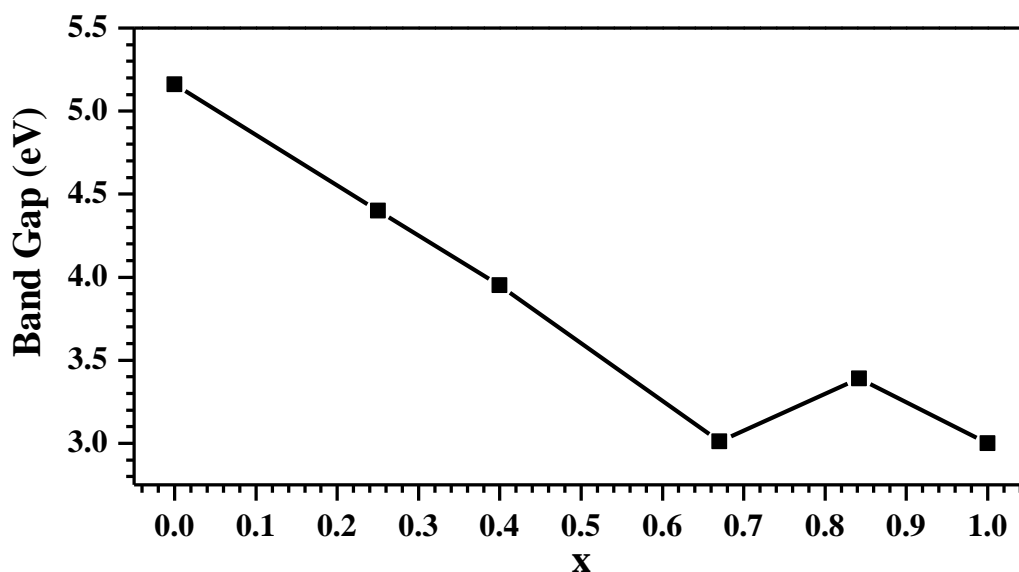


Figure 10. Variation of calculated band gap (eV) with  $x$  in the mullite phases including sillimanite and  $\iota$ - $Al_2O_3$ .

and it indicates a trend of decreasing band gap with increasing alumina content. Sillimanite has the largest band gap at 5.19 eV. The decrease in the band gap with  $x$  is almost linear up to 3.00 eV for 4/1 mullite ( $x = 0.67$ ). At 9/1 mullite, the band gap is slightly increased to 3.19 eV and then it returns to a similar value of 3.00 eV at  $\iota$ - $Al_2O_3$ . The decrease in the band gap from the crystalline phase to the more disordered mullite phases is obvious. A likely explanation for the fluctuation in band gap values near 9/1 mullite and beyond follows the same argument as for the mechanical properties. Fig. 9 shows that disorders in the structure of mullite are mostly reflected in the bands at the bottom of the conduction band (CB) because they have larger dispersions. These dispersions can be traced to the presence of O vacancies and distortions in the Al/Si tetrahedra. On the other hand, the top of the occupied valence band (VB) is dominated by the non-bonding O orbitals and are all flat with no dispersion. All the calculated band gaps are expected to be smaller than any measured values because the LDA generally underestimates the band gaps of insulators. There is no

band structures or gap values for the mullite phases available so far, either measured or calculated, that can be directly compared with this calculations. The calculated total density of states (TDOS) of the mullite phases including sillimanite and  $\iota$ - $Al_2O_3$  are shown in Fig. 11. These TDOS can be easily resolved into atomic and orbital components but this is not shown here. In all mullite phases, like in many other oxides, the lower VB DOS features are mostly from O atoms whereas the CB DOS features are from the Al atoms with significant contributions from the Si and O atoms. In sillimanite, DOS features show multiple well-resolved peak features corresponding to crystalline van Hove singularities. More detailed information on the electronic structure and spectroscopic calculations on the three phases of  $Al_2SiO_5$  using the OLCAO method can be found in ref [87]. In the mullite phases including  $\iota$ - $Al_2O_3$ , the DOS peaks become more broadened which is an indication of the disorder in the structure seen previously in the RPDF plots of Fig. 2. However, the presence of small peak structures near the band edges of the broadened DOS in the mullite phases comes from structural defects such as O vacancies and some severely distorted bonds in that particular model. These features are expected to be smoothed out if several models of the same mullite of the same x are averaged.

#### 4.4.2 Effective Charges and Bond Orders

Bond order (BO) and the effective charge ( $Q^*$ ) are important physical quantities that describe the bonding of atoms in solids and they must be calculated from the wave functions obtained by quantum mechanical calculations. Bond order (also called the overlap population) is a measure of the relative strength of a bond between a pair of atoms and it is the microscopic origin for the mechanical properties of materials. For the same type of atomic pairs, the BO values generally scale with the bond length but they can also be influenced by the near-by atoms and the local geometric environment. This is a distinct ad-

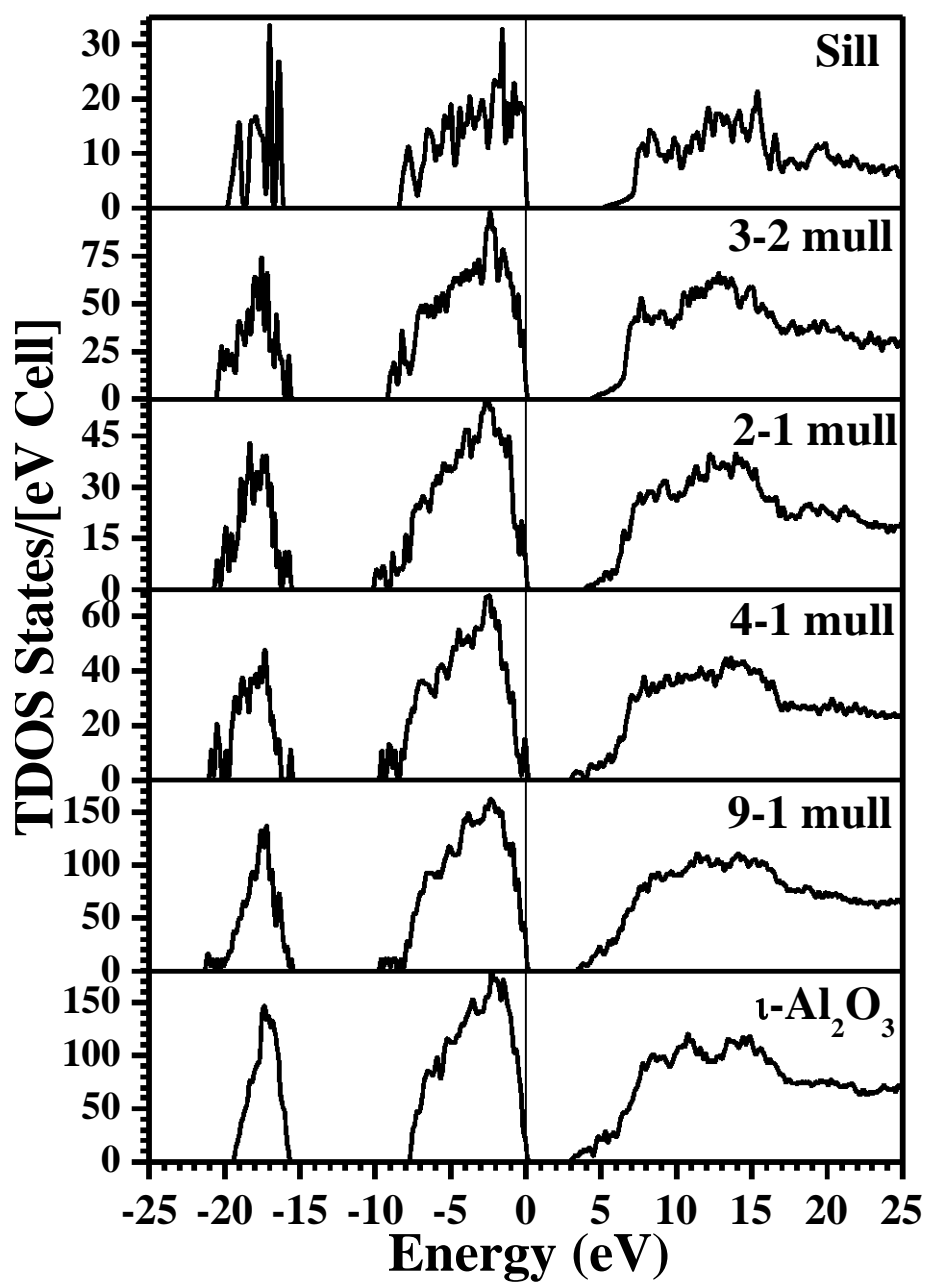


Figure 11. Calculated total density of states (TDOS) of mullite phases. The vertical line represents the top of valance band set at 0.0 eV.

Figure 11.

vantage of using bond order values to quantitatively assess the bond strength as opposed to simply using the atomic separations, or the alignment of peaks in the atom-resolved partial DOS as used in other methods. On the other hand,  $Q^*$  represents the total valence electrons of an atom in the solid and it can be used to provide important information on the charge transfer between atoms. The effective charges on the atoms should not be confused with the valence state of the atoms. In the OLCAO method  $Q^*$  and bond order are evaluated using the Mullikan scheme [38] with a minimal basis set using equations 3.14 and 3.15.

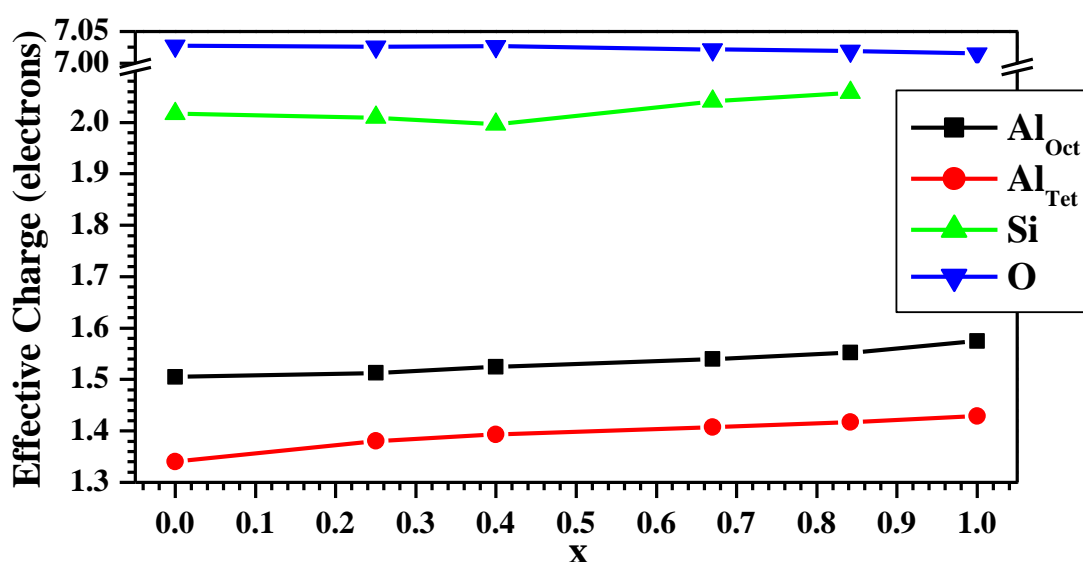


Figure 12. Average effective charge  $Q^*$  distribution in mullite phases.

The calculated average  $Q^*$  for each type of atom in the mullite phases in Fig. 12. The Al atoms are distinguished by either  $Al_{oct}$  or  $Al_{tet}$ . As expected for any ionic insulator, the cations (Al and Si) lose charge to the anions (O) in all phases. The charge lost by  $Al_{tet}$  is slightly larger than that lost by  $Al_{oct}$  by less than 0.2 electrons. This is consistent with the fact that tetrahedral Al has shorter bonds than the octahedral Al atoms. As  $x$  increases,

the charge transfer between cations and anions decreases slightly except for Si. There seems to be a reversal in the trend at 2/1 mullite. Before 2/1 mullite,  $Q^*$  for Si slightly decreases (more transfer and more ionic) and after 2/1 mullite,  $Q^*$  increases up to 9/1 mullite. Naturally, there is no  $Q^*$  for Si in  $\iota$ - $Al_2O_3$ . However, the average effective charge on O is almost constant indicating very little variation in the overall ionicity within the mullite series.

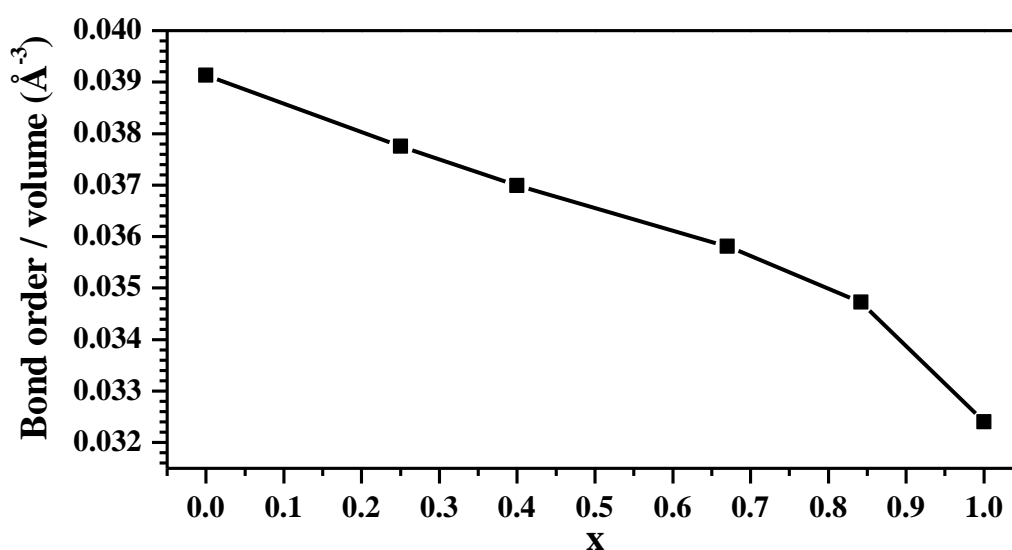


Figure 13. Variation of the bond order density in mullite phases with  $x$ .

Although the BO values for all pairs of atoms in the all four mullite phases, sillimanite and  $\iota$ - $Al_2O_3$  have been calculated, it is not practical to present all these BO values because the atoms in the mullite structures (except sillimanite) are all non-equivalent. For this reason, it is more meaningful to present the BO density which is the sum of all BO values of the nearest neighbor bonds in the model divided by volume of the crystal. Fig. 13 shows the BO density vs.  $x$  in the structure. As can be seen, sillimanite has the largest BO per volume and  $\iota$ - $Al_2O_3$  has the smallest. This is expected for two reasons. First, the

tetrahedral Si-O bonds are stronger bonds with larger BO values than the tetrahedral Al-O bonds. When x increases, Si in the structure decreases which leads to a decrease in total BO. Second, O vacancies increase with x which tends to increase some bond lengths which in turn can lead to a smaller total bond BO and a decrease in density. The ultralow-density  $\iota$ - $Al_2O_3$  has the largest decrease in BO density in comparison to the mullite phases. The trend of decreasing BO density with x is totally consistent with the decrease in mechanical strength throughout in the mullite series as the alumina content increases.

#### 4.4.3 Optical Properties of Mullite

Based on the calculated electronic structures of mullite, the interband optical properties of the four mullite phases in the form of the frequency-dependent real and imaginary dielectric functions  $\varepsilon(\hbar\omega)$  were calculated according to the equations 3.17 and OP3.

The calculation includes the momentum matrix elements from the occupied valence band states to the empty conduction band states at a relatively large number of k points in the BZ. The real part of the dielectric function  $\varepsilon_1(\hbar\omega)$  is obtained from the imaginary part  $\varepsilon_2(\hbar\omega)$  of Eq. 3.17 through the Kramers-Kronig conversion. From the zero frequency limit of  $\varepsilon_1(\hbar\omega)$  or  $\varepsilon_1(0)$ , the static optical dielectric constant, the refractive indices of the mullite models can be obtained as.

$$n = \sqrt{\varepsilon_1(0)} \quad (4.3)$$

Fig.14 shows the calculated  $\varepsilon_1(\hbar\omega)$  and  $\varepsilon_2(\hbar\omega)$  averaged over three Cartesian directions for the four phases of mullite and the two end members, sillimanite and  $\iota$ - $Al_2O_3$ , for frequencies up to 35 eV. Generally speaking, the absorption spectra  $\varepsilon_2(\hbar\omega)$  can be characterized as follows: (1) the threshold of absorption is determined by the band gap which decreases as x increases. The intensity of absorption increases rapidly after the threshold.

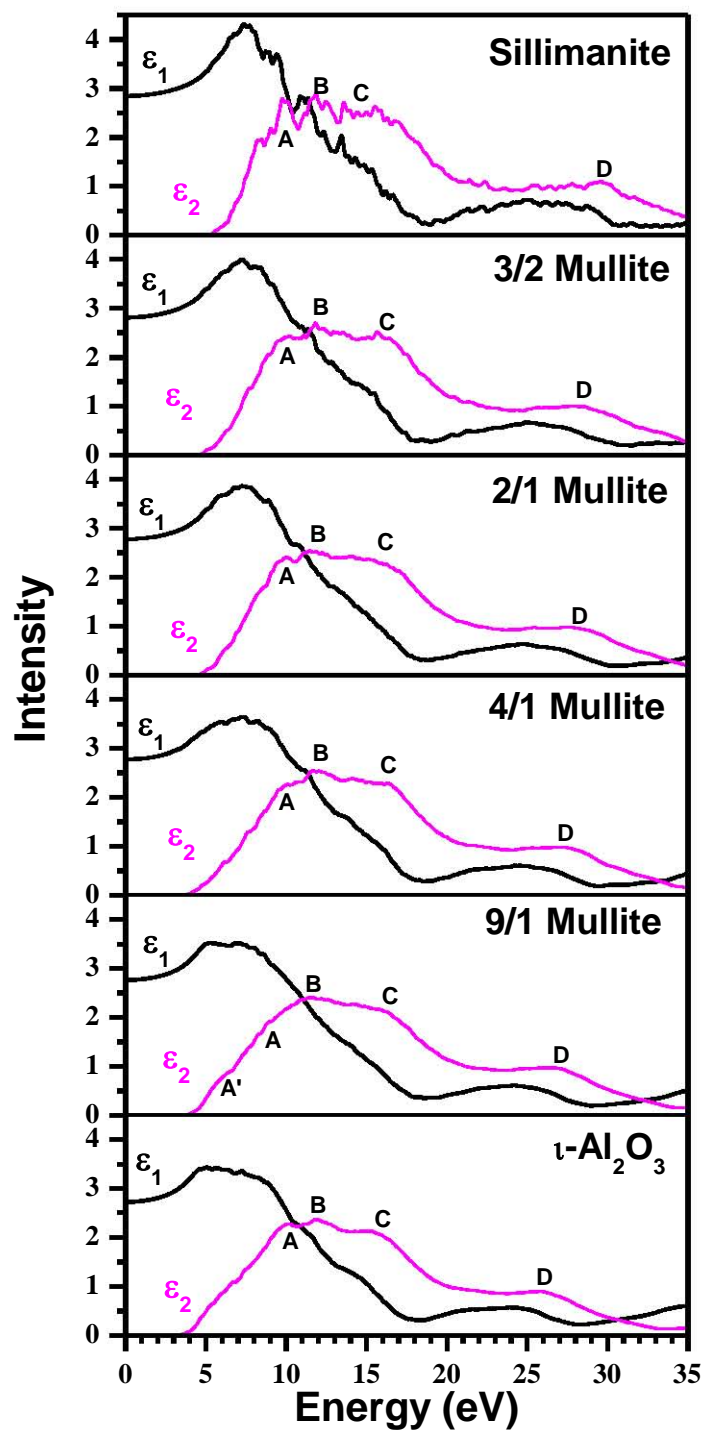


Figure 14. Calculated real and imaginary parts of the dielectric functions.

Table 5. Calculated refractive indices of mullite phases.

	$n$ (average)	$(n_x + n_y)/2$	$n_z$
Sillimanite	1.686	1.719	1.619
3-2 mullite	1.680	1.716	1.606
2-1 mullite	1.668	1.701	1.599
4-1 mullite	1.666	1.703	1.589
9-1 mullite	1.662	1.697	1.590
$t$ - $Al_2O_3$	1.652	1.689	1.570

(2) It is remarkable that the absorption features for all 6 mullite phases can be described as having four main features marked as A, B, C, D in Fig. 14. Peaks A and B are around 10.0 and 12.5 eV respectively. Feature C appears as a broad shoulder or a plateau centered around 15 eV. Feature D is another plateau at a higher energy between roughly 25 - 30 eV. (3) There exists anisotropy or birefringence in the components of  $\varepsilon_2(\hbar\omega)$  between the parallel (z-) and the perpendicular (x and y) directions but this is not shown here. (4) The similarities in the main features of  $\varepsilon_2(\hbar\omega)$  in the mullite series underscore the commonality of their underlying structures. The minor differences between them are due to shifts in the positions of the four features and their intensities. These differences stem from the difference in the alumina content and the specifics in the model structures. The crystalline sillimanite has a substantially smaller peak structures due to its crystalline nature. As the alumina content increases, the disorder increases and the optical absorptions become more broadened. At the 9/1 mullite where the structure is less certain and modeling has been more challenging, peak A seems to disappear whereas another broad shoulder A' at 6.5 eV emerges.

In Fig. 15, the refractive index  $n$  in mullite is plotted as a function  $x$  which shows an approximate linear relationship.  $n$  decreases as  $x$  increases or the alumina content increases. In Table 5, the refractive index values together with their parallel and perpendicular

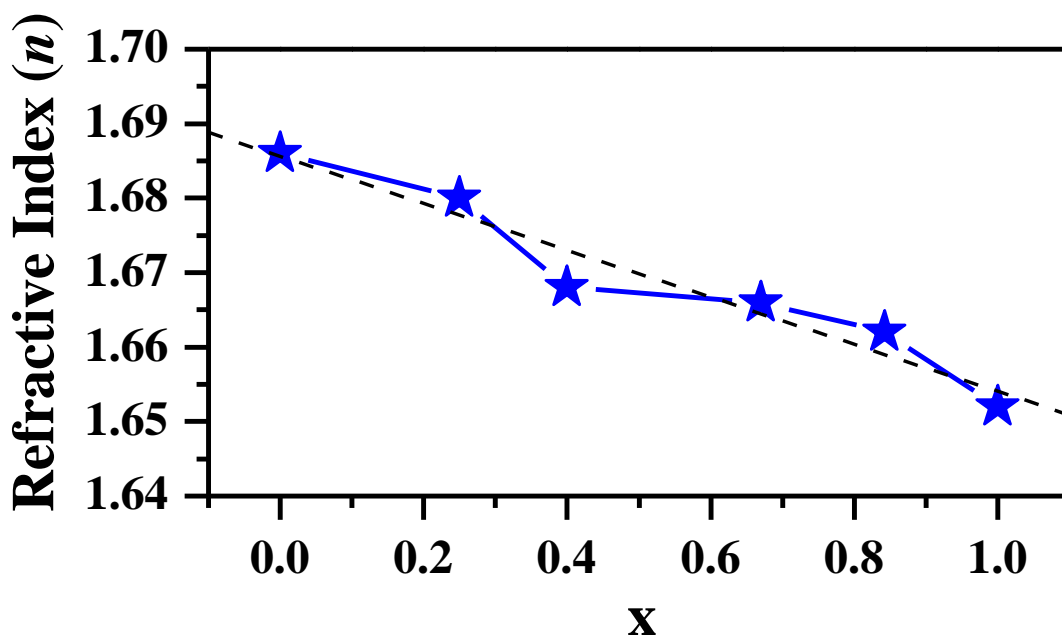


Figure 15. Variation of calculated refractive index  $n$  with  $x$  in the mullite phases including sillimanite and  $\iota$ - $Al_2O_3$ .

components are listed which show the existence of birefringence which is known to exist [97]. In spite of many claims about the importance of the optical properties of mullite, there is a lack of well documented values for the refractive indices along with their dependence on  $x$ . For the end members of the series, Klein and Hurlbut [98] listed a measured value of  $n = 1.69$  for sillimanite which is very close to calculated value of  $x = 1.686$ . For  $x = 1$ , or the  $\iota$ - $Al_2O_3$ , calculated value of  $n = 1.652$  is reasonably close to the value of 1.63 reported by Saafeld [92]. For the other mullite phases, indirect references to the mullite refractive index (usually implied to be the 3/2 mullite) can be used. For example, Wojtowicz et al. mentioned  $n$  for a mullite microcrystal to be 1.69 [99]. Spectral transmittance measurements on an infrared-transparent mullite ceramic with a composition of 72.3 wt. % of  $Al_2O_3$  yielded a refractive index value of 1.62 [100]. Optical measurements using a microrefractometer on 10 solid solution crystals of (Al, Ge) mullite give refractive indices in the range of 1.69

- 1.70 [101]. Commercial product brochures list  $n$  to be 1.654 for the 3/2 mullite powders etc. Hence, a systematic calculation of the refractive indices of the whole mullite series from the optical absorptions will be extremely useful for future references. Based on the 6 data points in Fig. 15, a linear relation of  $n(x) = -0.0316x + 1.686$  results which can be used to estimate the refractive index of mullite phases at any given  $x$ . The Table 5 also shows that the differences between the parallel and perpendicular components of  $n$  do not follow the similar linear scaling rule of Fig. 15, indicating that there is some other effect on the birefringence as the alumina content in the cell varies.

#### 4.5 Summary and Conclusions

This is a comprehensive study of the mechanical and electronic properties of the mullite series using first-principles methods. The stoichiometric supercell models based on the geometric structural pattern of crystalline sillimanite and existing experimental structural data on 3/2, 2/1, and 9/1 mullite are constructed. The published mullite structures were always presented using crystallographic terminology that identified some sites as being partially occupied. Until now, the issue of partial occupation in mullite structures has prevented any detailed theoretical calculations on their mechanical properties and electronic structures. The models constructed cover the whole range of mullite composition for the alumino-silicate series  $Al_{4+2x}Si_{2-2x}O_{10-x}$ , with  $x$  ranging from 0 to 1. The RPDF plots of relaxed supercell models show an increased disorder in the structure with increasing alumina content. The calculated lattice constants and their trends in the change of structural parameters are consistent with the measured data on mullite samples.

Based on these stoichiometric supercell models, the mechanical properties and electronic structures of the mullite phases are calculated and their trends with  $x$  analyzed. The calculated elastic stiffness constants of mullite phases show a direct correlation with the

alumina content in the structure. As alumina content increases there is an accompanying increase in O vacancy and the mullite structure loses its elastic strength. This loss in elastic strength is predominantly due to the decrease in  $C_{33}$  which can be traced to the replacement of the stiffer Si tetrahedra with weaker Al tetrahedra and partially broken Al/Si tetrahedral chains along the crystallographic c-axis. The changes in other elastic coefficients are also analyzed in detail in relation to the structural changes in the series. Shear stiffness constants  $C_{44}$ ,  $C_{55}$ ,  $C_{66}$  and other off diagonal stiffness constants do not follow specific trends. The calculated bulk mechanical properties show that the bulk moduli K, shear modulus G, and Young's modulus E all decrease with increasing alumina content whereas the Poisson's ratio increases up to 4/1 mullite and then decreases sharply at 9/1 mullite. The calculated results are in good agreement with measurements on single crystals of 3/2 and 2/1 mullite.

The sound velocities of the mullite phases are calculated using data from the elastic coefficients. For the 3/2 mullite, there is a noticeable anisotropy in sound velocity distribution in different planes consistent with its structural pattern. The (100) plane shows the highest anisotropy and the (001) plane shows the least anisotropy. When alumina content in the structure increases, anisotropy in the longitudinal sound velocity distribution in all three planes decreases up to 4/1 mullite but has a slight increase at 9/1 mullite.

The electronic structures and the optical properties of the mullite series are presented for the first time. They are all wide band gap insulators with a direct band gap at the Brillouin zone center. The band gap decreases linearly with increasing alumina content up to 4/1 mullite with a small increase at 9/1 mullite. The calculations of effective charge  $Q^*$  for each type of atom and the calculations of bond order density for each mullite phase are most useful and revealing. These  $Q^*$  calculations show a lack of variation in the ionicity of the mullite series and the bond order density variation shows a clear trend that is consistent with a decrease of mechanical strength in the mullite series with the increase

of alumina content. The calculated refractive indices of mullite show an approximate linear correlation with changes in the alumina content and the values are in good agreement with the available measured data.

This is the first theoretical work on the mullite phases that covers both elastic and electronic properties. This is the first step towards an understanding of the physical properties of mullites and their variations in the alumina content. This work also validates the approach of using the sillimanite structure as a starting point for the description of the subsequent mullite structures. Most importantly, the use of supercells was shown to be a practical way to account for the partially occupied sites in mullite structures. There are still areas that the present calculations can be further improved or enhanced. For example, only one representative model for each mullite phase was used. In principle, it is more ideal to have averaged results from at least several other models. It is also desirable to have more mullite models at different  $x$  values rather than being restricted to 3/2, 2/1, 4/1, and 9/1 mullites. The inclusion of the end member of the mullite series with  $x = 1$  is particularly significant because it provides detailed information on a relatively new transition alumina that could bridge the relations between two important classes of ceramic materials, alumina and mullite. In the coming years, it should be possible to use large-scale first-principals computations for determining other interesting properties of mullite such as the temperature dependence of the mechanical strength and the effects of impurity contaminations, or intentionally included dopants to achieve specific purposes. High temperature properties and phases transitions through ab initio phonon calculations are also possible as was demonstrated in the case of  $\iota$ - $Al_2O_3$  [102]. Because mullite phases have been used as special optical materials when doped with transition metal ions, their optical properties can also be investigated and related to experimental data. Such work will lead to further understanding of its fundamental properties and extend its scope of application.

## CHAPTER 5

### STRUCTURE AND PROPERTIES OF IOTA-ALUMINA ( $\iota$ - $Al_2O_3$ )

#### 5.1 Introduction

The iota phase of alumina ( $\iota$ - $Al_2O_3$ ) came to light more than fifty years ago when Foster [5] found the x-ray patterns of rapidly quenched cryolite-alumina melts to be similar to those of a known mullite phase. It was later recorded as the  $\iota$ - $Al_2O_3$  in the powder diffraction file. When this new phase was heated it converted to one of the transition alumina  $\eta$ - $Al_2O_3$  and then to corundum ( $\alpha$ - $Al_2O_3$ ), indicating its metastable nature. A few years later, Saalfeld reported the observation of needle-like crystals having a structure similar to that of sillimanite ( $Al_2SiO_5$ ) on  $Al_2O_3$ - $Ni$  cermets at high temperatures (about 1700°C) in the presence of water vapor [92]. In 1974, there were reports of the existence of a silicon-free mullite-like alumina with x-ray diffraction (XRD) patterns similar to that of mullite [6, 7] although there were conflicting opinions as to whether the crystal was orthorhombic or tetragonal [50, 92]. Very recently, interest in this elusive phase of alumina has revived. Korenko et al. reported the XRD patterns on samples believed to belong to  $\iota$ - $Al_2O_3$  in deeply undercooled cryolite-alumina melts from rapid solidification processing [103]. Ebadzadeh and Sharifi proposed a simple method to synthesize  $\iota$ - $Al_2O_3$  from a mixture of aluminum nitrate and carboxymethyl cellulose [104].

In spite of these previous efforts, the structural details of  $\iota$ - $Al_2O_3$  are not available and its physical properties are totally unknown. The first step to understand the structure of  $\iota$ - $Al_2O_3$  is to understand the structural details of aluminosilicates, or the mullite series [47]. In general, aluminosilicates can be represented by a solid solution series  $Al_{4+2x}Si_{2-2x}O_{10-x}$  where x represents the number of O vacancies in the structure. Thus,

the sillimanite crystal ( $x = 0$ ) is the end member of the series corresponding to 1-1 mullite ( $Al_2O_3 \bullet SiO_2$ ). It has two Al sites (octahedral and tetrahedral or  $Al_{oct}$  and  $Al_{tet}$ ), one Site<sub>tet</sub> site and 4 nonequivalent O sites.  $Al_{oct}$  atoms run along the crystallographic c-axis and are cross-linked by  $Al_{tet}$  and Site<sub>tet</sub> sites which are also aligned along the c-axis. As  $x$  increases in the solid solution series, the alumina ( $Al_2O_3$ ) content increases and silica ( $SiO_2$ ) content decreases. This can be seen in stoichiometric mullite phases of 3-2 mullite ( $3 Al_2O_3 \bullet 2 SiO_2$ ,  $x = 0.25$ ), 2-1 mullite ( $2 Al_2O_3 \bullet 1 SiO_2$ ,  $x = 0.4$ ), 4-1 mullite ( $4 Al_2O_3 \bullet 1 SiO_2$ ,  $x = 0.6667$ ) and 9-1 mullite ( $9 Al_2O_3 \bullet SiO_2$ ,  $x = 0.842$ ). The increase in alumina content in the series can be realized by successive replacement of Si by Al followed by the removal of O atoms to maintain charge balance, which creates vacancies in the structure. This process makes the structure more and more complex and disordered. The removal of O atoms introduces vacancies in the structure and the readjustment of bonds makes the tetrahedral Al/Si alignment along the crystallographic c-axis distorted. When  $x = 1$ , the solid solution series leads to a silica free phase, or  $\iota-Al_2O_3$ . This could be argued as being a process in which the alumina content in mullite is increased to its maximum and, once reached, this silica free phase should still possess structural signatures of mullite phases.

Despite the multiple points of evidence of its existence,  $\iota-Al_2O_3$  is the least understood phase of alumina. There is no experimental or theoretical works on  $\iota-Al_2O_3$  so far that have elucidated its physical properties other than the refractive index and density listed in reference [92]. In work, a comprehensive study of  $\iota-Al_2O_3$  based on a theoretically constructed model is presented.

## 5.2 Structural Modeling of $\iota$ - $Al_2O_3$

### 5.2.1 Construction of Model

As discussed in the introduction,  $\iota$ - $Al_2O_3$  is the end member in the aluminosilicate solid solution series  $Al_{4+2x}Si_{2-2x}O_{10-x}$  with  $x=1.0$ . It is therefore natural to assume that the structure of  $\iota$ - $Al_2O_3$  should be close to the mullite phase with high alumina content but with all Si atoms replaced by Al along with the removal of some oxygen to make it stoichiometric. This process results in a more disordered structure. The experimental structural data [91] of a high alumina mullite phase ( $x = 0.826$ ) which are presented in Table 6 is used as starting structure for modeling of  $\iota$ - $Al_2O_3$ .

Table 6. Experimental Structural Data of High Alumina Content Mullite Phase ([91])

Chemical formula $Al_{2.826}Si_{0.174}O_{4.588}$				
Space Group PBAM (55)				
$a = 7.7391, b = 7.6108, c = 2.9180$				
$\alpha = 90, \beta = 90, \gamma = 90$				
Fractional Coordinates of Atoms				
Atom	x	y	z	occupancy
Al	0.0000	0.0000	0.0000	1.000
AlT	0.1479	0.3317	0.5000	0.500
SiT	0.1479	0.3317	0.5000	0.087
Al*	0.2590	0.2203	0.5000	0.294
Al**	0.3350	0.1030	0.5000	0.119
Oab	0.3539	0.4209	0.5000	1.000
Oc	0.4700	0.0280	0.5000	0.294
Od	0.1336	0.2164	0.0000	1.000

In Table 6, the site labeled as Al is fully occupied and is octahedrally coordinated. All of the other Al and Si cation sites are tetrahedrally coordinated and are partially occupied. For the O sites, Oab and Od are fully occupied whereas Oc which bonds only with

tetrahedral Al and Si sites is partially occupied. The sites labeled as AlT and SiT are geometrically equivalent sites, and therefore there are only 4 non-equivalent cation sites. To convert the mullite structure (Table 6) into an initial model for  $\iota$ - $Al_2O_3$  (Table 7) with correct stoichiometry, different labeling as Al as Al1, (AlT, SiT) as Al2, and (Al\*, Al\*\*) as Al3 with combined occupancy were used. Further, three oxygen sites Oab, Oc, and Od are relabeled as O1, O2, and O3 with some changes to the occupancy as described next. When Al replaces Si, the structure becomes non-stoichiometric and it is necessary to remove an appropriate number of O atoms to make it stoichiometric. In the mullite phases when alumina content increases, certain O atoms are removed. It is observed that the removed O (Oc) is the one which bridges AlT and SiT [8] sites. Following the same pattern, the removal of O atoms can be realized by changing the occupancy of the O2 site. For this reason, the occupancy of the O2 site is reduced to 0.25 from 0.294. In this representation, the initial ideal structure for  $\iota$ - $Al_2O_3$  has 15 atoms in the unit cell with an orthorhombic lattice of space group PBAM. The atomic coordinates are listed in Table 7.

Table 7. Initial idealized model of  $\iota$ - $Al_2O_3$  derived from high alumina mullite phase.

Chemical formula $Al_2O_3$				
Space Group PBAM (55)				
$a = 7.7391, b = 7.6108, c = 2.9180$				
$\alpha = 90, \beta = 90, \gamma = 90$				
Fractional Coordinates of Atoms				
Atom	x	y	z	occupancy
Al1	0.0000	0.0000	0.0000	1.000
Al2	0.1479	0.3317	0.5000	0.587
Al3	0.2590	0.2203	0.5000	0.413
O1	0.3539	0.4209	0.5000	1.000
O2	0.4700	0.0280	0.5000	0.250
O3	0.1336	0.2164	0.0000	1.000

The ideal structural data of  $\iota$ - $Al_2O_3$  presented in Table 7 cannot yet be used for theoretical calculations due to the use of partial occupation notation for certain sites. To overcome this difficulty, a large  $2 \times 2 \times 4$  supercell of the initial model was generated and certain number of atoms were deleted at the appropriate sites to account for the partial occupancy. There are many different possibilities for generating a supercell model in this manner. So, 20 such models with different configurations of tetrahedral Al and O2 sites were constructed. All the 20 models were then fully relaxed using VASP (to be described below) and the model with the lowest total energy was taken as the representative model for the structure of  $\iota$ - $Al_2O_3$ .

### 5.2.2 Structural Analysis

The relaxed supercell model of  $\iota$ - $Al_2O_3$  has 240 atoms and is shown in Fig. 16.

The lattice constants are  $a = 15.6735$ ,  $b = 15.1652$ ,  $c = 11.9823$ ,  $\alpha = 90.130$ ,  $\beta = 90.257$ ,  $\gamma = 90.183$ . Fischer and Schneider [105] studied the change in lattice constants of mullite phases with increasing alumina content. They found that  $a$  increases linearly,  $b$  decreases non-linearly and  $c$  increases non-linearly. Lattice constants  $a$  and  $b$  cross at  $x = 0.67$  (80 mole % of  $Al_2O_3$ ) and beyond that  $a$  is larger than  $b$ . The extrapolated lattice constants for 100% alumina are in reasonable agreement with the lattice constants of the present model for  $\iota$ - $Al_2O_3$  scaled back to the unit cell dimension by dividing  $a$ ,  $b$ , and  $c$  by factors of 2, 2, and 4 respectively.

After full relaxation, the structure lost the distinct site labeling that was presented in Table 7 due to the disordered nature of the model. The previously labeled  $Al_{oct}$  and  $Al_{tet}$  atoms now have distorted polyhedral bonding environments with varying Al-O bond lengths and even coordination number. For the purpose of better describing the structure of  $\iota$ - $Al_2O_3$ , it is more practical to classify the atomic sites into different groups according

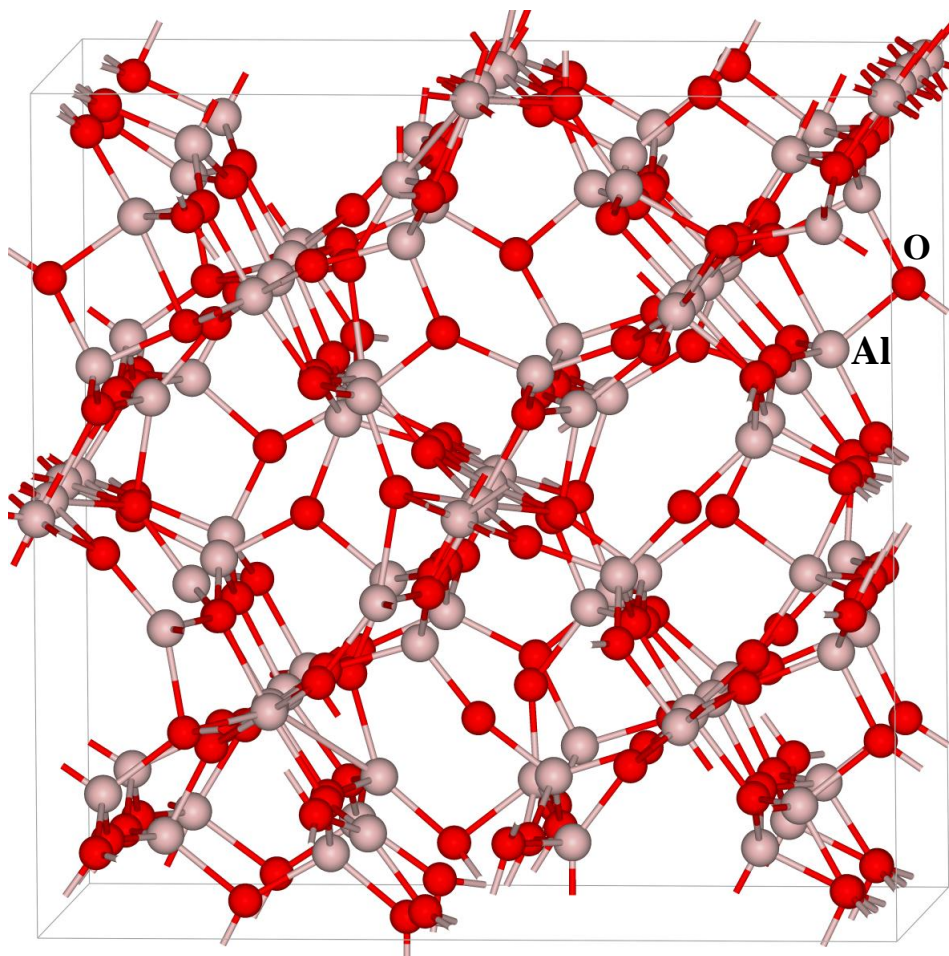


Figure 16. Relaxed supercell model of  $\iota$ - $Al_2O_3$ .

to their local environments. Using a reasonable criterion of 2.0 Å as a cutoff for the Al-O bonds, the Al and O atoms can be grouped into five distinct Al groups and three O groups which are listed in Table 3. There are roughly two groups for Al atoms,  $Al_{oct}$  and  $Al_{tet}$ . They can be further divided into subgroups because relaxation causes some of the bonds to elongate or distort with considerable deviations in individual bond lengths (BLs) from the average. The O-atoms can also be divided into three groups O-A, O-B, and O-C according to the bonds they form with Al and the deviations of the BL within. The number of atoms in each group and their general characteristics are described in the Table 8. The division

of the atoms in  $\iota$ - $Al_2O_3$  according to Table 8 will be further elucidated and correlated with the results of x-ray absorption near edge structure (XANES) spectral calculations of  $\iota$ - $Al_2O_3$  in Section 3.8.

Table 8. Al and O Groups in the Relaxed  $\iota$ - $Al_2O_3$  Model.

Group	#Atoms	Description
$Al_{oct}$	32	This group was octahedrally coordinated before relaxation and relatively ordered with alignment along c-axis. After relaxation, they can be divided into 2 subgroups. Subgroup $Al_{oct}$ -A retains the average bonding environment with 6 Al-O bonds, and subgroup $Al_{oct}$ -B has a slightly shorter average BL with only 5 Al-O bonds.
$Al_{tet}$	64	This group was originally from the tetrahedrally coordinated Al before relaxation and is highly disordered after relaxation. It can be further divided into 3 subgroups. Subgroup $Al_{tet}$ -A retains the normal pattern with 4 fold coordination. Subgroup $Al_{tet}$ -B is also 4 fold coordinated but is more disordered with one of the bonds being longer. Atoms in subgroup $Al_{tet}$ -C are 3-fold coordinated with shorter BLs than the group average.
O-A	64	This group of O atoms are either 3-fold or 4-fold coordinated and are highly disordered. Some of them have a relatively longer Al-O bond than the average.
O-B	16	This is the most disordered group of O atoms with either 3 or 2 bonds that bond only with $Al_{tet}$ .
O-C	64	This is the least disordered group of O atoms; all are 3-fold coordinated with bond lengths close to the average value.

A common practice of investigating the structure of non-crystalline and amorphous materials is to calculate their radial pair distribution function (RPDF). The calculated RPDF between Al-O, Al-Al, and O-O atomic pairs are shown in Fig. 17. It can be seen that the RPDF of Al-O has two well-resolved peaks at 1.75 Å and 1.88 Å which correspond to the averaged Al-O separations for  $Al_{tet}$ -O and  $Al_{oct}$ -O. There are only a few sporadic Al-O

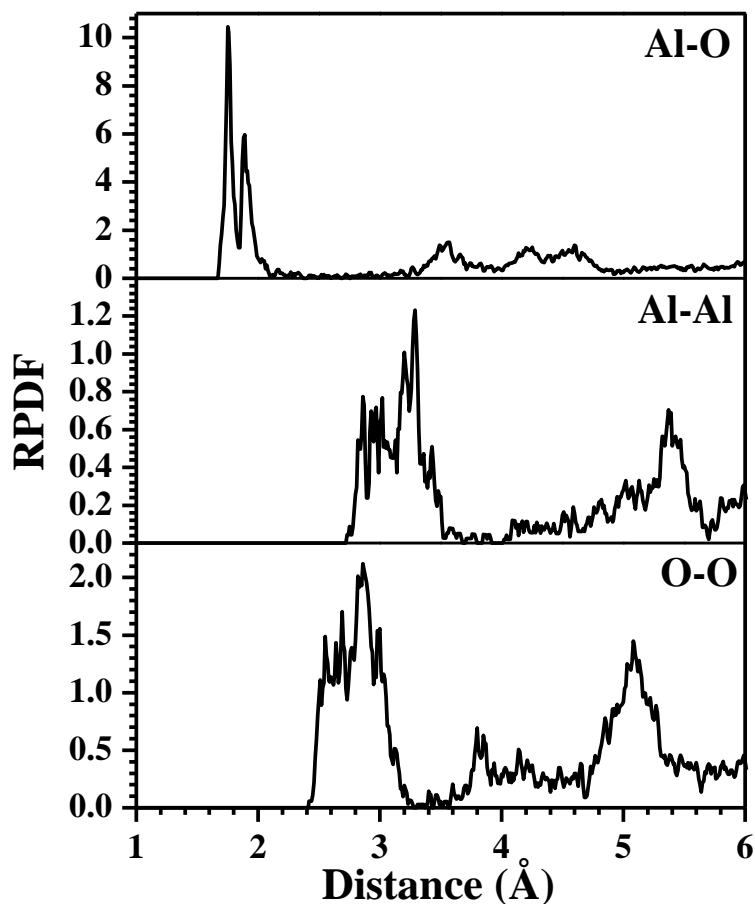


Figure 17. Radial pair distributions function of  $\nu$ - $Al_2O_3$ .

pairs slightly between  $2.0\text{\AA}$  and  $3.4\text{\AA}$ , indicating the presence of a few longer bonds associated with the disorder. The RPDF plots for Al-Al and O-O pairs are quite broadened indicating both a lack of long-range order in the structure and a sufficiently large supercell size. Despite the lack of long-range order, the RPDF of  $\nu$ - $Al_2O_3$  is quite different from that of amorphous alumina ( $a$ - $Al_2O_3$ ). Two sharp peaks, which appear in Al-O RPDF in  $\nu$ - $Al_2O_3$  are absent in both the measured and simulated  $a$ - $Al_2O_3$  structures [106–108]. Measured Al-O pair correlation function of  $a$ - $Al_2O_3$  show a sharp peak at  $1.8\text{\AA}$  [106], which is about the average bond length of  $\nu$ - $Al_2O_3$ . Calculated Al-O pair distribution

functions of a- $Al_2O_3$  at various densities also show a single peak [107, 108]. In both calculations, the position of the peak appears to be independent of density. However, the positions of the peak from the two different simulations are somewhat different. Another, interesting point is the Al polyhedral content in the structure. Only in  $\alpha$ - $Al_2O_3$ , which is the most stable phase of alumina, all Al are in octahedral setting. In other phases, there are different compositions of Al octahedra and tetrahedra. In  $\gamma$ - $Al_2O_3$ , there are 62.5 %  $AlO_6$  octahedra and 37.5 %  $AlO_4$  tetrahedra [25]. As the disorderness increases, from  $\gamma$ - $Al_2O_3$  to  $\iota$ - $Al_2O_3$ , the structure adjusts to include  $AlO_5$  and  $AlO_3$ . In  $\iota$ - $Al_2O_3$ , there are 22.9 %  $AlO_6$ , 10.4 %  $AlO_5$ , 60.4 %  $AlO_4$  and 6.25%  $AlO_3$ . In a- $Al_2O_3$ , it also consists of different Al polyhedra depending on density [107, 108]. The  $\iota$ - $Al_2O_3$  is at the lower end of transition alumina with some features close to amorphous phase. The lower density of  $\iota$ - $Al_2O_3$  than that of the a- $Al_2O_3$  (2.9 to 3.3  $g/cm^3$ ) is due to the O vacancy, which is a structural feature of mullite frame.

### 5.2.3 X-ray Diffraction Pattern

Construction of the  $\iota$ - $Al_2O_3$  model is based on the idea that the pattern of evolution of high alumina content in mullite phases is somehow followed up to  $\iota$ - $Al_2O_3$ . A large supercell of 240 atoms provides an ample space for adjustment and reconstruction of atomic configuration in the structure. After full relaxation, it is supposed that this supercell model of  $\iota$ - $Al_2O_3$  is reliable and represents the true phase claimed to be a silicon-free mullite-like phase of alumina. For further confirmation of the correctness of the model, XRD pattern of the 6 fully relaxed supercell models with lowest total energy were simulated using the powdercell program [109]. Fig. 18 shows the calculated XRD pattern as compared to two measured patterns that are labeled as Expt. 1 [7] and Expt. 2 [104]. The measured XRD data are similar to each other but Expt. 2 is slightly shifted to lower values of  $2\theta$  and it agrees

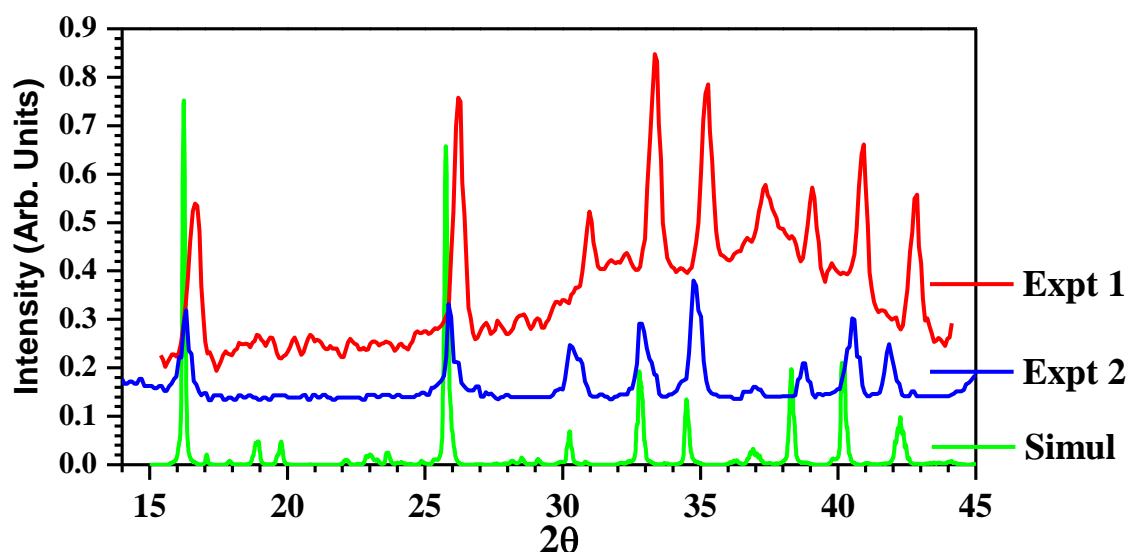


Figure 18. Simulated x-ray diffraction pattern of  $\iota$ - $Al_2O_3$  as compared to experiment. Expt 1 is from reference [7] and Expt 2 is from reference [104].

better with simulation. Although there is a shift in peak positions between Expt. 2 and the simulated spectrum at higher values of  $2\theta$ , the magnitude of the shift is no greater than the difference between Expt. 1 and Expt. 2. In Expt. 1, the authors claimed that the broad line at  $37.36$  ( $2\theta$ ) is caused by the presence of  $\gamma$ - $Al_2O_3$  in the sample which is almost negligible in Expt. 2. Within the regions of  $2\theta$  between 18 and 24 there are a few small peaks that are not shown in the experiment. It is likely that this is due to the finite size of the supercell and a few of them were used for the XRD spectral calculation.

### 5.3 Results and Discussions

#### 5.3.1 Total Energy and Density

Of the various phases of transition alumina, iota-alumina ( $\iota$ - $Al_2O_3$ ) is the least well known due to its elusive history. Transition alumina are the complex intermediate phases ( $\beta$ ,  $\gamma$ ,  $\eta$ ,  $\theta$ ,  $\kappa$ ,  $\chi$  etc.) that occur in the processing of alumina from raw materials, eventually reaching the thermodynamically most stable phase,  $\alpha$ - $Al_2O_3$  [110]. They generally

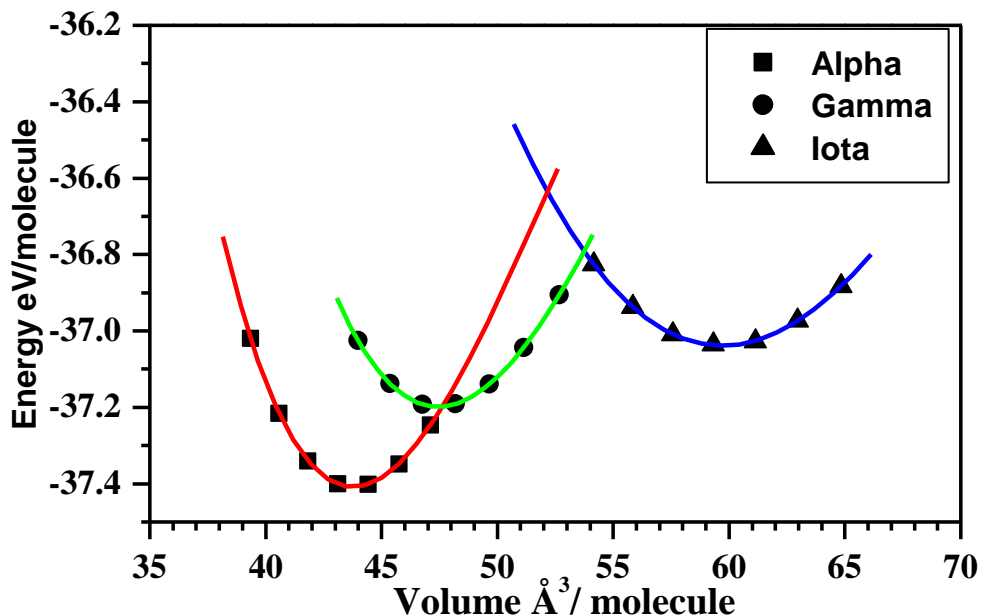


Figure 19. Calculated total energy vs. volume of  $\alpha$ - $Al_2O_3$ ,  $\gamma$ - $Al_2O_3$ , and  $\iota$ - $Al_2O_3$ .

have lower density, higher total energy, and more complex structures. In Fig. 19 calculated total energy plotted against the volume per molecule for  $\alpha$ - $Al_2O_3$ ,  $\gamma$ - $Al_2O_3$ , and  $\iota$ - $Al_2O_3$  are displayed. For each phase, total energy of the crystal was calculated under successively greater hydrostatic compressions (3 points) and expansions (3 points) from its equilibrium fully relaxed volume. The calculated total energy per  $Al_2O_3$  molecule (and calculated density) for  $\alpha$ - $Al_2O_3$ ,  $\gamma$ - $Al_2O_3$ , and  $\iota$ - $Al_2O_3$  are -37.401 eV ( $3911 \text{ kg/m}^3$ ), -37.192 eV ( $3513 \text{ kg/m}^3$ ), and -37.036 eV ( $2854 \text{ kg/m}^3$ ) respectively. Thus,  $\iota$ - $Al_2O_3$  can be an ultra-low density transition alumina preceding  $\gamma$ - $Al_2O_3$  which is also a highly disordered phase [25]. The calculated density of  $\iota$ - $Al_2O_3$  is slightly smaller than the measured value of  $3000 \text{ kg/m}^3$  quoted by Saafeld [92] using the suspension method in a liquid of known density. The discrepancy can be easily explained by the presence of some Si and maybe other impurities in the measured sample.

### 5.3.2 Elastic Properties

A strain-stress analysis scheme [40] as described in chapter 3 has been used to obtain the elastic coefficients of  $\iota$ - $Al_2O_3$ . The bulk modulus (K), shear modulus (G), Young's modulus (E), and Poisson's ratio ( $\eta$ ) are obtained from  $C_{ij}$  using the Voigt-Reuss-Hill approximation [42, 43, 111]. These calculated values are presented in Table 9 together with those of  $\alpha$ - $Al_2O_3$  and  $\gamma$ - $Al_2O_3$  which were calculated in a similar manner [25]. Obviously, there are no measurements or other calculated data of  $\iota$ - $Al_2O_3$  to compare with our calculations. As can be seen,  $\iota$ - $Al_2O_3$  is much softer than  $\alpha$ - $Al_2O_3$  and  $\gamma$ - $Al_2O_3$  which is consistent with its ultra-low density. Its bulk modulus K (shear modulus G) is only 57.0% (42.5%) of that of  $\alpha$ - $Al_2O_3$ . The ratio of G/K is a reasonable measure of the ductility of a metal [112] where higher values indicate a more brittle material. It is interesting to note that the G/K ratios for  $\iota$ - $Al_2O_3$ ,  $\gamma$ - $Al_2O_3$ , and  $\alpha$ - $Al_2O_3$  are 0.478, 0.555, and 0.642 respectively, indicating that  $\iota$ - $Al_2O_3$  is less brittle on the condition that this simple rule can also be applied to ceramics. On the other hand, the Poisson's ratio of  $\iota$ - $Al_2O_3$  is larger than that of  $\alpha$ - $Al_2O_3$  and  $\gamma$ - $Al_2O_3$  which means that  $\iota$ - $Al_2O_3$  tends to resist volume change more. In  $\alpha$ - $Al_2O_3$ , the elastic constants along all principle directions are the same, and in  $\gamma$ - $Al_2O_3$ ,  $C_{11}$  is slightly larger than  $C_{22}$  and  $C_{33}$ . However, in  $\iota$ - $Al_2O_3$ , it appears to carry the characteristics of the mullite phases because  $C_{33}$  is larger than  $C_{11}$  and  $C_{22}$ . This is related to the fact that the Al octahedral and tetrahedral units are aligned along the c-axis of the current model reinforcing stiffness in that direction. The stiffness is reduced compared to the mullite structure though because the Al tetrahedral units are highly disordered.

### 5.3.3 Phonon Dispersion

Phonon dispersion is the fundamental description of the vibrational properties of a crystal or non-crystalline solid. It defines a solids finite temperature properties and it plays a crucial role in numerous microscopic and bulk phenomena such as thermodynamic phase transitions, thermal expansion, infrared absorption, Raman scattering, etc. In the present phonon calculation for  $\iota$ - $Al_2O_3$ , a small displacement is applied to each non-equivalent atom in the structure along the three Cartesian directions. The resulting force on each atom in the supercell is used to construct the dynamic matrix. Diagonalization of the dynamic matrix gives the  $3N$  modes (3 acoustic and  $3N-3$  optical) where  $N$  is the number of atoms in the cell. The correction for the longitudinal optical (LO) and transverse optical (TO) splitting was neglected since it is less important in a highly disordered solid such as  $\iota$ - $Al_2O_3$ .

The structure of  $\iota$ - $Al_2O_3$  is quite large of 240 atoms in it, and all the atoms are non-equivalent. Calculating phonon is quite computationally expensive. So, for practical reason, all the VASP calculations were done only on gamma-point of the Brillouin zone. Phonon calculations is very sensitive to the accuracy of force constant matrix so a very

Table 9. Elastic constants and bulk moduli of  $\iota$ - $Al_2O_3$  (GPa)

Crystal	$C_{11}$	$C_{22}$	$C_{33}$	$C_{44}$	$C_{55}$	$C_{66}$	$C_{12}$	$C_{13}$	$C_{23}$
$\iota$ -Al <sub>2</sub> O <sub>3</sub>	196.0	208.8	264.9	84.3	60.6	76.6	97.0	91.4	117.7
$\alpha$ - $Al_2O_3^\dagger$	476.8	476.8	476.8	145.5	145.5	145.5	157.4	119.4	-
$\gamma$ - $Al_2O_3^\dagger$	416.3	390.3	390.3	89.3	94.3	136.5	127.2	97.9	100.5
Crystal	K	G	E	$\eta$	G/K				
$\iota$ -Al <sub>2</sub> O <sub>3</sub>	140.8	67.3	174.1	0.294	0.478				
$\alpha$ - $Al_2O_3^\dagger$	246.9	58.5	391.6	0.236	0.642				
$\gamma$ - $Al_2O_3^\dagger$	204.0	113.2	286.5	0.266	0.555				

† [25]

small electronic convergence limit  $1 \times 10^{-8} eV$  is used.

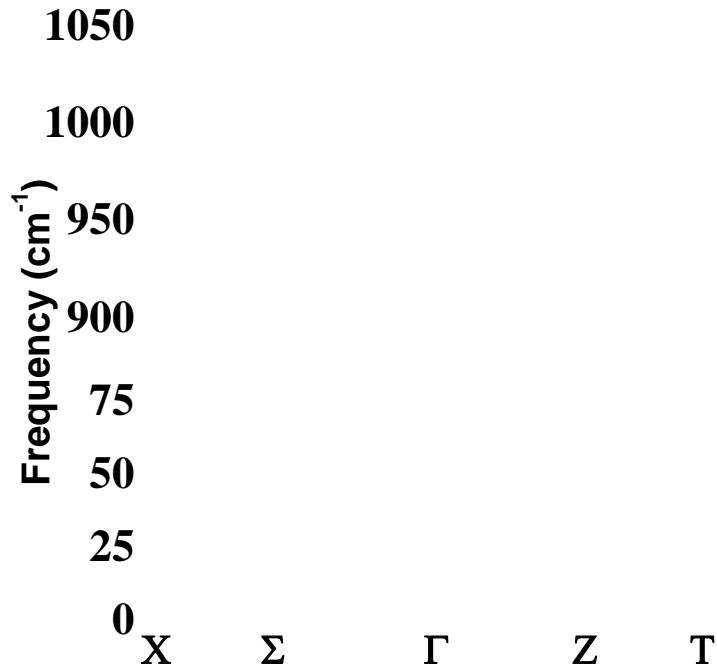


Figure 20. Phonon dispersion along high symmetry lines.

Fig. 20 shows the calculated phonon dispersion of  $\iota-Al_2O_3$  in its equilibrium structure along the high symmetry points of the orthorhombic lattice. For clarity only the lower and upper parts of the dispersion curves are shown since the middle part is very dense and less informative. The phonon density of states (DOS) and its partial components (Al and O) are shown in Fig. 21. There are a few small negative frequency modes near, but not at, the  $\Gamma$  point pointing in the  $\Gamma$  to  $\Sigma$  and  $\Gamma$  to Z directions. Our initial concern was that these were due to insufficient k-point sampling. However, these could also be seen as an indication of the metastable nature of the  $\iota-Al_2O_3$  model and could be the result of defective centers in the structure. This is also manifested in the very broad feature of the vibrational DOS shown in Fig. 21. In the lower frequency region, the Al and O atoms

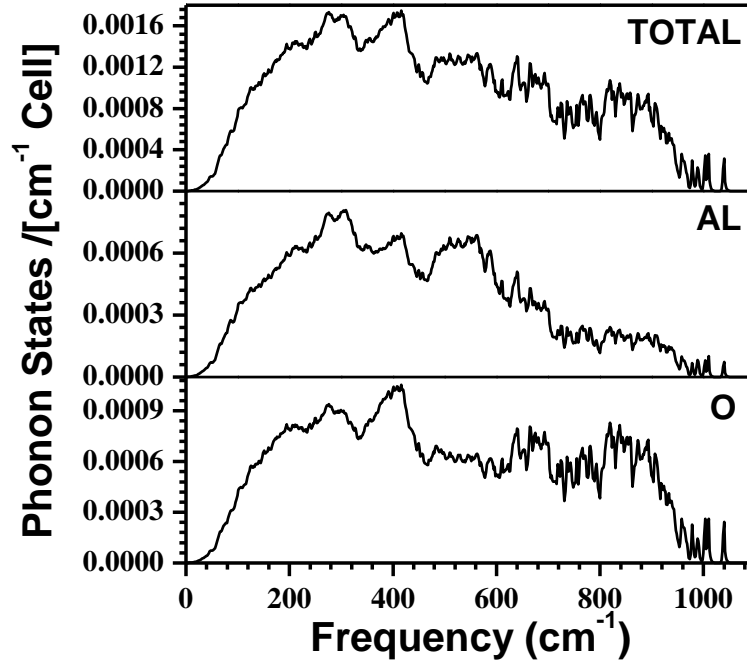


Figure 21. Phonon density of states of  $\nu$ - $Al_2O_3$ . Top panel: total DOS, middle panel: Al PDOS, and bottom panel: O PDOS.

contribute almost equally to the vibrational DOS whereas in the higher frequency region, the vibrations that are related to the lighter O atoms tend to dominate. Compared to similar calculations done on  $\gamma$ - $Al_2O_3$  (Fig.3 of ref. [25]), the phonon DOS features of  $\gamma$ - $Al_2O_3$  are less broadened because it effectively has only two types of bonding coordination for both Al and O and it is less disordered than  $\nu$ - $Al_2O_3$ . Fig. 22 shows the zone center frequency modes plotted against the localization index (LI). Because of the lack of symmetry in  $\nu$ - $Al_2O_3$ , detailed symmetry analysis of frequency modes is not possible, these frequency modes consist of Raman active, Infrared (IR) active and inactive modes. The localization index (LI) is calculated according to following equation:

$$LI_m = \left( \sum_{i=1}^N (a_i^2 + b_i^2 + c_i^2)^2 \right)^{\frac{1}{2}} \quad (5.1)$$

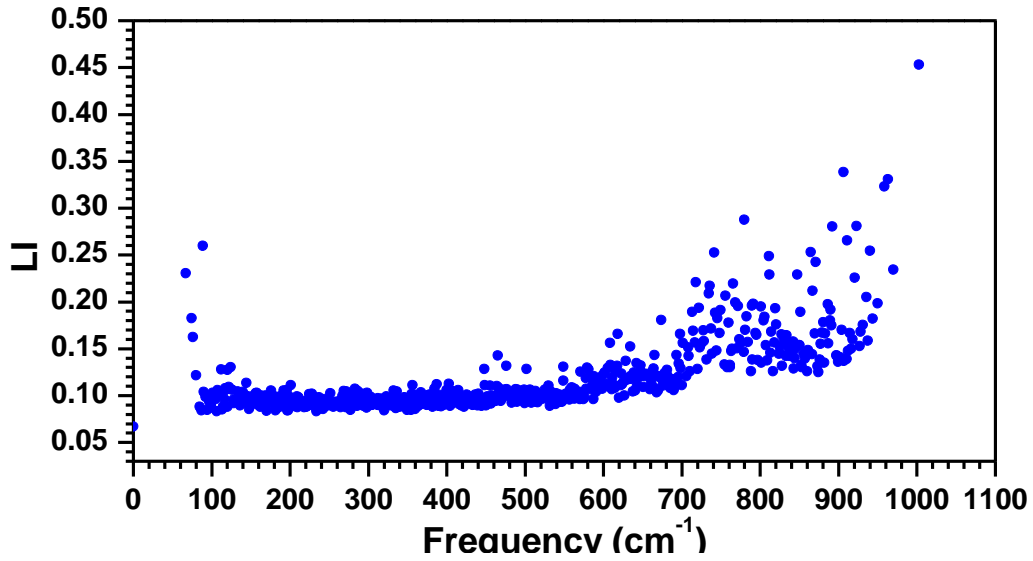


Figure 22. Zone center frequency modes of  $\nu$ - $Al_2O_3$  plotted against the localization index (LI).

Where  $a_i$ ,  $b_i$ ,  $c_i$  are the eigenvector components of the  $i^{th}$  atom in the  $m^{th}$  frequency mode. As can be seen in the figure, the high frequency modes, which are mostly dominated by O oscillations, are relatively more localized and can be traced to particular defective local structures. Similarly, several modes in the low frequency region are also localized. The lowest five non-zero frequency modes in  $\nu$ - $Al_2O_3$  are at 2.003, 2.238, 2.278, 2.397, and 2.542 THz and the highest frequency mode is at 31.134 THz.

#### 5.3.4 Thermodynamic Properties

Thermodynamic properties of  $\nu$ - $Al_2O_3$  are calculated based on the phonon calculations on 7 volumes which is explained in the section 3.4. These calculations are within quasi-harmonic approximations. The parameters used for force constant calculation in each volume is same as that to equilibrium structure as mentioned in section 5.3.3.

Fig. 23 shows the calculated specific heat capacity at constant volume ( $C_V$ ) of

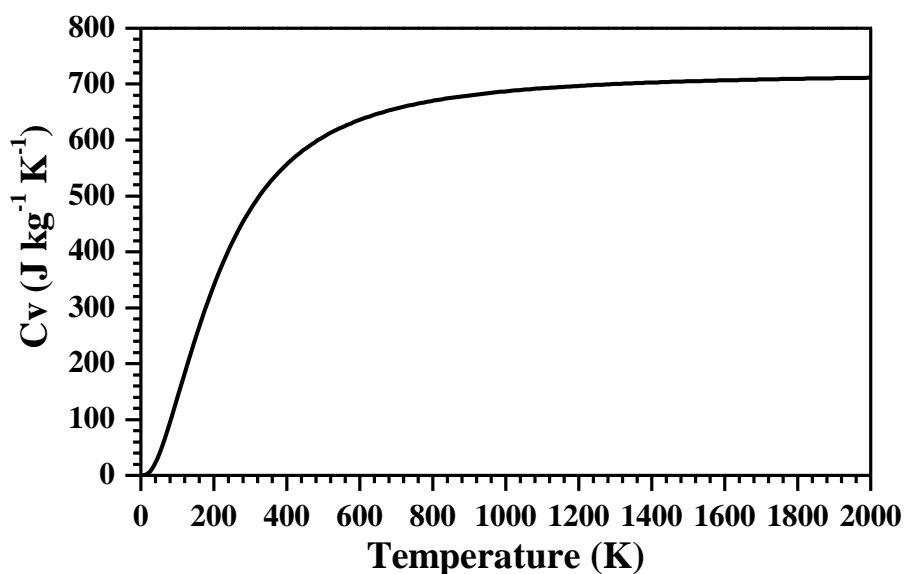


Figure 23. Temperature dependent specific heat capacity at constant volume ( $C_V$ ) for  $l\text{-Al}_2\text{O}_3$ .

$l\text{-Al}_2\text{O}_3$  as a function of temperature. Initially,  $C_V$  rises rapidly between  $T = 0$  K and about 550 K before it starts to saturate. The  $C_V$  of  $l\text{-Al}_2\text{O}_3$  at 295 K is 470.4 J/Kg K which is only about half that of  $\alpha\text{-Al}_2\text{O}_3$  as reported in literature. The isothermal bulk modulus  $B$  of  $l\text{-Al}_2\text{O}_3$  at 295 K as a function of pressure is presented in Fig. 24. At  $P = 0$  and  $T = 295$  K,  $B = 122$  GPa which is considerably smaller than the 140.8 GPa (Table 9) calculated using the stress vs. strain technique at  $T = 0$ . This quite large difference indicates a rapid increase in the softness of the structure as the temperature increases. As the  $P$  increases,  $B$  also increases and it reaches its maximum at a hydrostatic pressure of 7 GPa. Beyond 7 GPa,  $B$  starts to decrease. This behavior indicates that  $l\text{-Al}_2\text{O}_3$  may be unstable at high pressures even under isothermal conditions. Figs. 25 and 26 display the calculated  $G(P, T)$  of  $l\text{-Al}_2\text{O}_3$  and the difference in  $G(P, T)$  between  $\gamma\text{-Al}_2\text{O}_3$  and  $l\text{-Al}_2\text{O}_3$  respectively using colored contour plots. The Gibbs free energy of  $l\text{-Al}_2\text{O}_3$  is lower at high temperature and low pressure conditions, so this may be an indication that  $l\text{-Al}_2\text{O}_3$

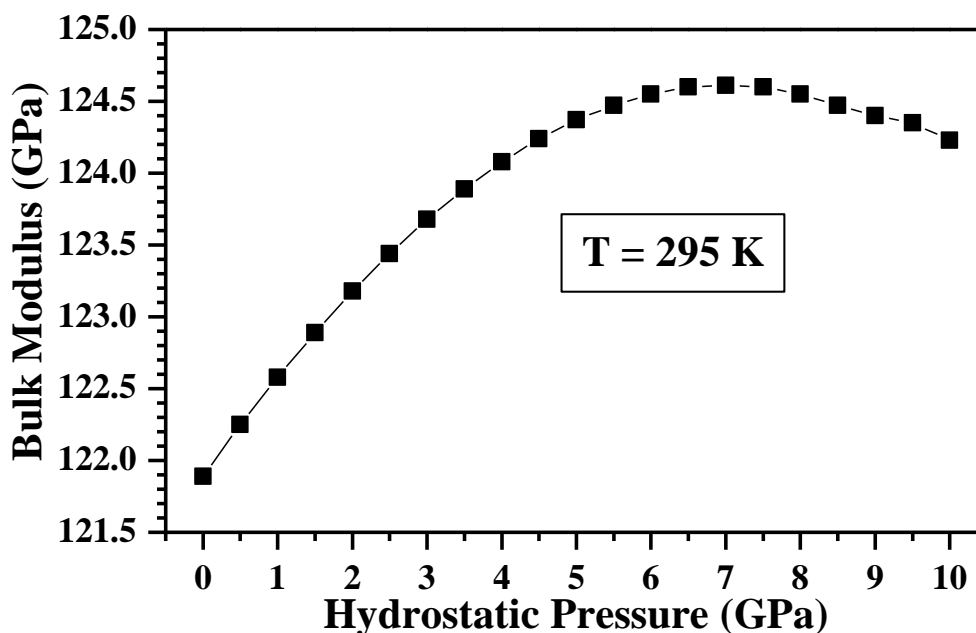


Figure 24. Isothermal bulk modulus of  $\nu$ - $Al_2O_3$  as a function of pressure at 295 K.

is relatively more stable at high temperature and at low pressure, a fact that has implications in the processing conditions involving  $\nu$ - $Al_2O_3$ . Fig. 26 shows the difference in  $G(P,T)$  between  $\gamma$ - $Al_2O_3$  and  $\nu$ - $Al_2O_3$  in a wide range of pressures and temperatures. (Please note the huge difference in the scale bar for the diagrams colors compared to Fig. 25). The difference in  $G(P, T)$  between  $\gamma$ - $Al_2O_3$  and  $\nu$ - $Al_2O_3$  is small but noticeable. It shows that  $\gamma$ - $Al_2O_3$  is relatively more stable than  $\nu$ - $Al_2O_3$  for any combination of pressure and temperature within the range indicated. However, in the low P and high T region, their difference is negligibly small, which again indicates the relatively higher stability of  $\nu$ - $Al_2O_3$  at low pressure and high temperature conditions.

### 5.3.5 Electronic Structure

This section is for the discussion to the calculated electronic structure of  $\nu$ - $Al_2O_3$  based on the supercell model described above and using a different *ab initio* method, the all-

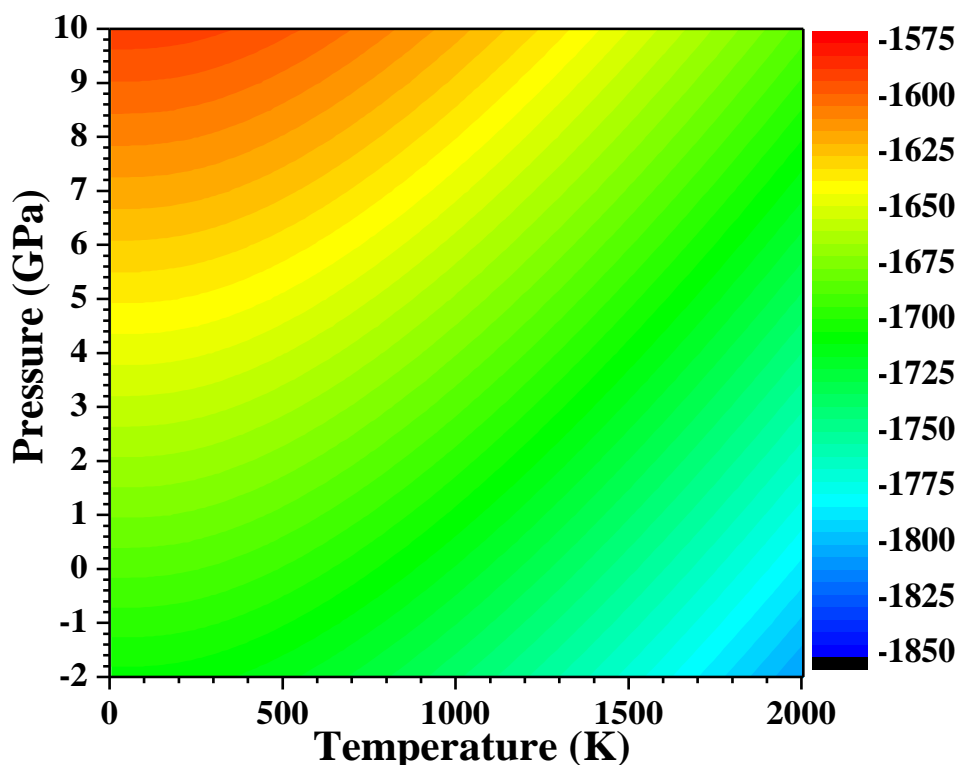


Figure 25. Gibbs free energy  $G(P, T)$  of  $\iota\text{-Al}_2\text{O}_3$  in eV.

electron OLCAO method. One of the many versatile features of OLCAO method is the use of different basis sets for different purposes. For band structure and density of states (DOS) calculations, a full basis which consists of occupied and unoccupied orbitals of Al (1s, 2s, 2p, 3s, 3p, 4s, 4p, 4d, 5s, 5d) and O (1s, 2s, 2p, 3s, 3p, 4s, 4p) atomic orbitals are used. The core orbitals (listed in bold) are later orthogonalized against the non-core orbitals. The full basis is sufficiently large to obtain accurate ground state electronic structures for any crystal. Fig. 27 shows the calculated band structure of  $\iota\text{-Al}_2\text{O}_3$  in the range of -2.0 to 8 eV. This figure 27 was also included in 9 of chapter 4. This is included here to make it easy to read so one does not need turn pages back to see the figure. The bands are very dense due to the large unit cell of  $\iota\text{-Al}_2\text{O}_3$ . It is an insulator with a direct LDA band gap of 3.0 eV which may be slightly underestimated. The calculated band gaps for  $\alpha\text{-Al}_2\text{O}_3$  [113]

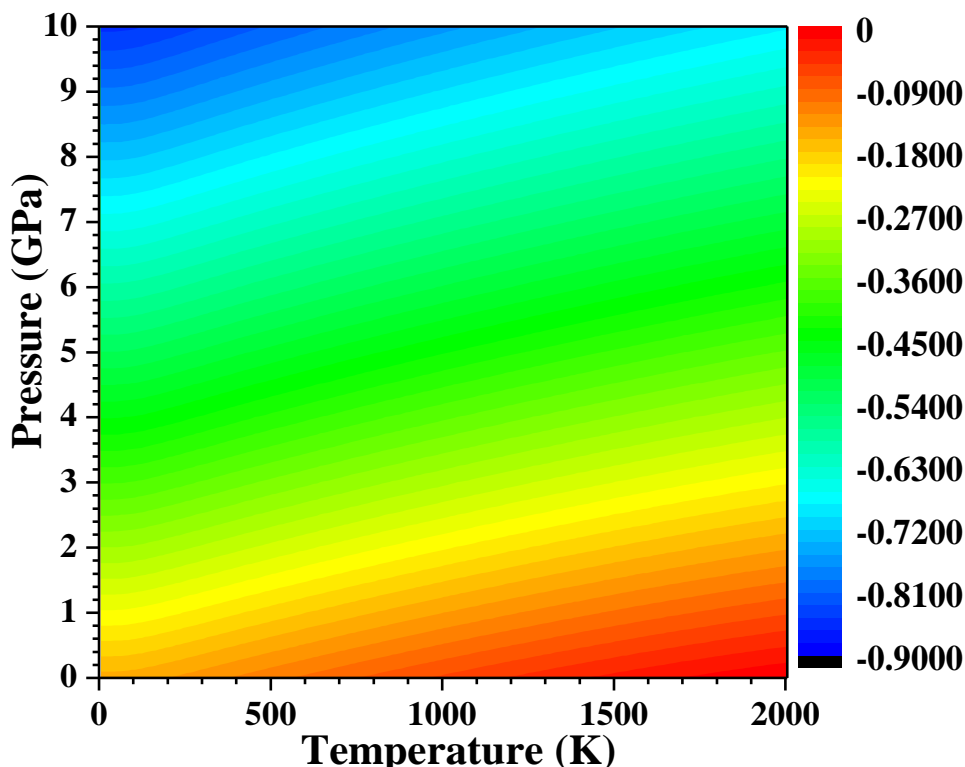


Figure 26. Difference in  $G(P, T)$  between  $\gamma\text{-Al}_2\text{O}_3$  and  $\epsilon\text{-Al}_2\text{O}_3$  in eV.

and  $\gamma\text{-Al}_2\text{O}_3$  [25] using the same OLCAO method are 6.31 eV and 4.22 eV respectively. Thus, the band gaps in these three alumina crystals scale inversely with the density and the associated degree of disorder. The top of the valence band (VB) for  $\epsilon\text{-Al}_2\text{O}_3$  is very flat and the bottom of the conduction band (CB) is at the point which presents an electron effective mass ( $m^*$ ) of 0.54  $m_e$  where  $m_e$  is the mass of a free electron. Fig. 28 shows the total density of states (TDOS) and atom-resolved partial density of states (PDOS) for Al and O. The PDOS are further broken down into their orbital components.  $\epsilon\text{-Al}_2\text{O}_3$  is a very complex and disordered system which is manifested in the broadening of the VB and CB features in the TDOS and PDOS peaks. As in other aluminum oxides, the VB DOS comes mostly from O atoms whereas the CB TDOS peak features are mostly from Al atoms. There are two distinct parts in the VB, the lower part centered at -17.41 eV is the

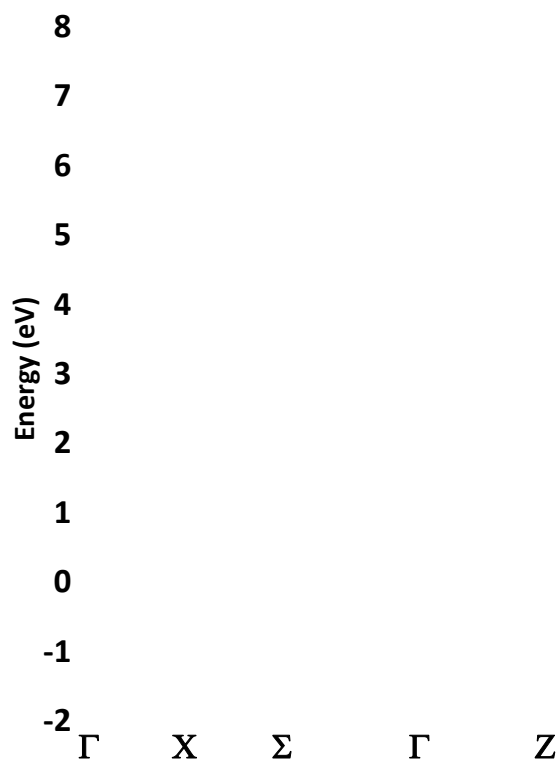


Figure 27. Calculated band structure of  $\iota$ - $Al_2O_3$  along high symmetry points of the BZ.

13

O-2s peak and the upper part which peaks at -2.28 eV originates from the O-2p orbitals, both interact with Al orbitals. The top of the upper VB comes from the non-bonding O-2p orbitals which are also responsible for the flat top of the upper VB band structure. The CB TDOS has several well-resolved peak features A, B, and C roughly at 8.4 eV, 10.7 eV, and near 14 eV respectively. The CB TDOS features are mostly from p and d orbitals of Al atoms but there is strong mixing with the other orbitals especially in the lower energy region. These features will greatly affect the core-level spectra of the Al-K, Al-L, and O-K XANES spectra to be discussed in the later section.

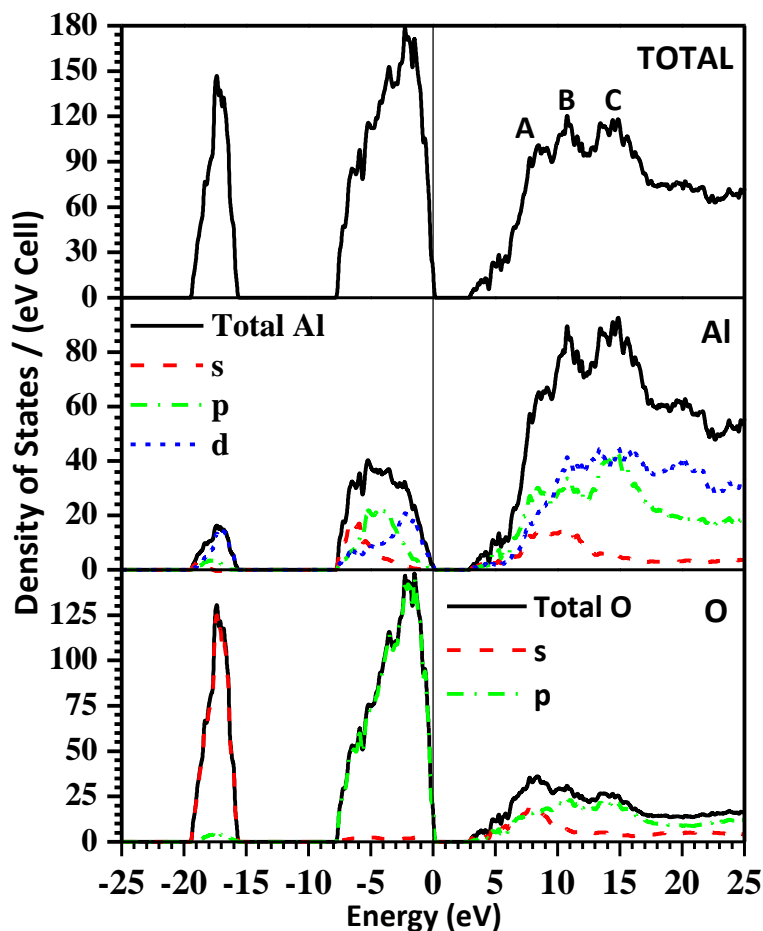


Figure 28. Calculated total, Al partial, and O partial electron density of states of  $\iota$ - $Al_2O_3$ . Orbital components are as indicated.

### 5.3.6 Effective Charge

Another simple yet very effective application of the OLCAO method is the calculation of the effective charge  $Q^*$  on each atom based on the Mullikan scheme [38].  $Q^*$  is the effective charge (in units of electrons) on each atom and it provides information on the nature of the bonding and charge transfer between atoms of different types. Because the calculation uses the *ab initio* wave functions, rather than purely geometrical considerations, the  $Q^*$  value obtained depends also on the local atomic environment and interactions with

neighboring atoms. For effective charge calculations the minimal basis set is used because it is more localized so as to be consistent with the assumption used in Mullikans molecular orbital approach. The  $Q^*$  are evaluated according the equation 3.14 presented in chapter 3.

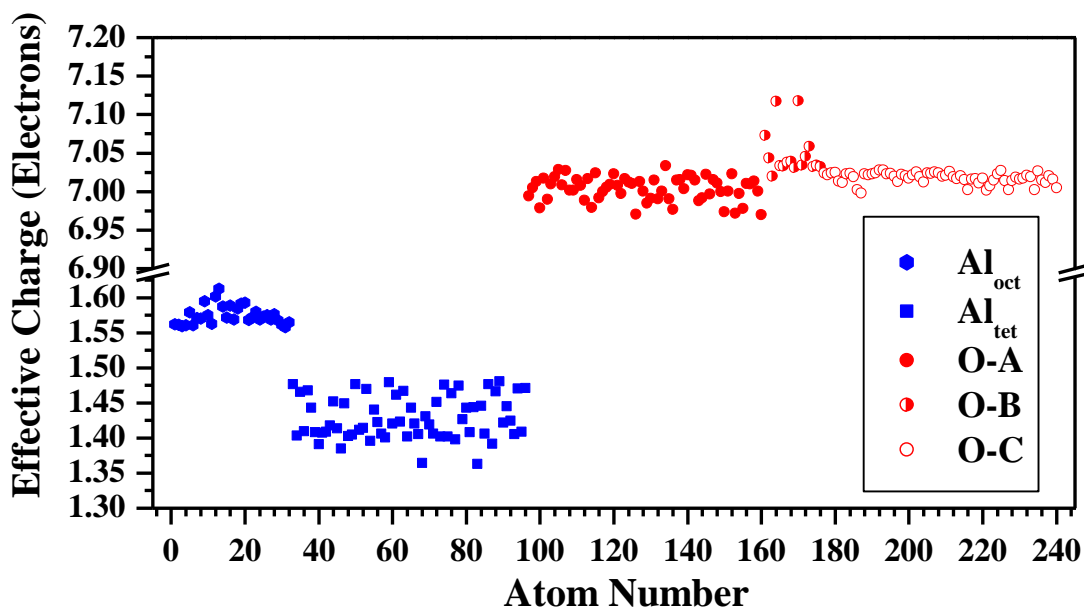


Figure 29. Distribution of effective charge  $Q^*$  of individual atoms in  $\nu$ - $Al_2O_3$ .

In Fig. 29, the  $Q^*$  for the 240 atoms in the supercell model of  $\nu$ - $Al_2O_3$  are plotted. Atoms labeled from 1-96 are Al atoms and those labeled from 97 to 240 are O atoms. As discussed in section 2.3, the atoms in  $\nu$ - $Al_2O_3$  can be roughly divided into two Al groups,  $Al_{oct}$  (atoms 1-36) and  $Al_{tet}$  (atoms 37-96). For O atoms, the group assignment is less clear but they can still be roughly classified into 3 groups as described in Table 8. The average  $Q^*$  for  $Al_{oct}$  ( $Al_{tet}$ ) is 1.57 (1.43) electrons. On average,  $Al_{oct}$  have longer Al-O bond lengths than  $Al_{tet}$  and therefore they have a larger effective charge (or less charge transfer to O). The  $Q^*$  distribution in  $Al_{tet}$  is relatively more dispersed than in

$Al_{oct}$ . This is because replacement of tetrahedral Si by Al and the creation of O vacancies in the structure mostly affects the  $Al_{tet}$  sites. For the  $Q^*$  of the O atoms, the group O-A has a relatively more dispersed distribution than the group O-C. As in the  $Al_{tet}$  groups, the creation of O vacancies and the subsequent structural readjustment affects the O atoms in this group more than in other O groups. For the O-B group (atoms labeled 161 to 176), 4 O atoms are only 2-fold coordinated and they have gained slightly more charge. The effective charge of O-C group (atoms labeled 177 to 240) is relatively less dispersed than in other O groups. In general, the effective charge distribution in  $\iota-Al_2O_3$  does not show the crystalline characteristics of the structure. Averaging over all groups, the  $Q^*$  on Al and O in  $\iota-Al_2O_3$  are 1.48 and 7.01 electrons. This is to be compared with the  $Q^*$  for Al and O in  $\alpha-Al_2O_3$  (1.90 and 6.74 electrons, [114]) and  $\gamma-Al_2O_3$  (1.54 and 6.98 electrons, ref [25]). This leads to a conclusion that  $\iota-Al_2O_3$  has a larger charge transfer from Al to O and therefore is more ionic than  $\alpha-Al_2O_3$  and  $\gamma-Al_2O_3$ .

### 5.3.7 Optical Properties

Optical properties of  $\iota-Al_2O_3$  are calculated in the form of the frequency-dependent dielectric function using the OLCAO method. In this case, an extended basis set was used which consists of one more shell of unoccupied atomic orbitals than the full basis. The calculated optical spectra are shown in Fig. 30, which displays real ( $\epsilon_1(\hbar\omega)$ ) and imaginary ( $\epsilon_2(\hbar\omega)$ ) parts of the dielectric functions.

The imaginary part  $\epsilon_2(\hbar\omega)$  is calculated first according to the equation 3.17: The calculated  $\epsilon_2(\hbar\omega)$  spectrum has quite broadened peak features with the first prominent peak at 10.3 eV followed by the main peak at 11.8 eV. The real part,  $\epsilon_1(\hbar\omega)$ , is obtained from  $\epsilon_2(\hbar\omega)$  through Kramers-Kronig conversion. The calculated static dielectric constant,  $\epsilon_1(0)$ , of  $\iota-Al_2O_3$  is 2.728 which corresponds to a refractive index of 1.652. Amazingly,

this number is almost the same as the refractive index value of 1.63 reported by Saafeld (1962) [2]. This small difference could be coincidental though, considering both the uncertainty in the sample of the early measurement and the limitations of the LDA theory used in calculating the optical absorption spectrum. Calculated values of  $\epsilon_1(0)$  for  $\alpha\text{-Al}_2\text{O}_3$  and  $\gamma\text{-Al}_2\text{O}_3$  using same OLCAO method are 3.14 [115] and 3.15 [25] respectively with corresponding refractive index values of 1.78 and 1.77. Both are larger than that of  $\iota\text{-Al}_2\text{O}_3$ . This is in consistent with the result that  $\iota\text{-Al}_2\text{O}_3$  is a low-density phase with more ionic bonding.

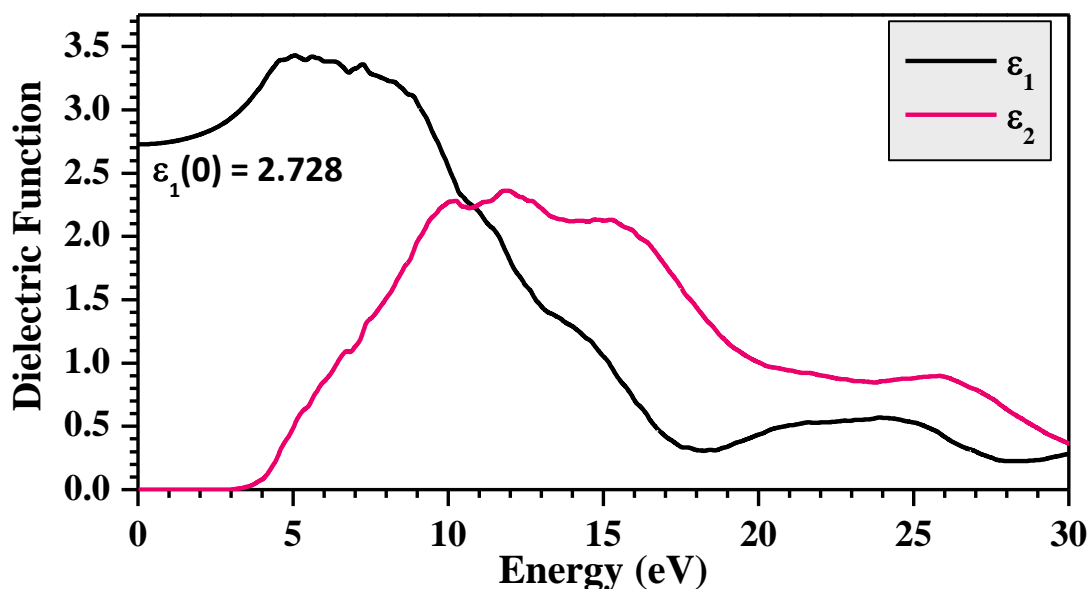


Figure 30. Calculated frequency dependent dielectric functions of  $\iota\text{-Al}_2\text{O}_3$ .

### 5.3.8 XANES/ELNES Spectra

X-ray absorption near-edge structure (XANES) and electron energy loss near-edge structure (ELNES) spectroscopies are powerful characterization techniques for obtaining

information about the electron states in the unoccupied CB as related to the bonding environment of a particular atom in a solid. They are usually more sensitive than photoelectron spectroscopy which probes the occupied VB state. Experimentally, it is difficult to obtain the XANES/ELNES spectrum of a specific edge at a particular site for most solids. Most likely, the measured spectrum is the average spectral response over many different sites of the same type of atom. This is not a problem for simple crystals where atomic sites are equivalent. However, in complex crystals with many non-equivalent sites, or for atoms at grain boundaries or at the interfaces of a crystal, it is a great experimental challenge to obtain atom specific spectra for accurate analysis. One of the main developments of the OLCAO method in recent years has been the *ab initio* calculation of XANES or ELNES edges using a supercell approach [116, 117] that takes into account the core-hole effect. The supercell-OLCAO method can provide the theoretical spectrum at any atomic site thereby facilitating the interpretation of measured spectra. The steps of the calculation used in the supercell-OLCAO method have been described in detail in ref. [117] and will not be repeated here. This method has been successfully used to obtain the XANES/ELNES spectra of many crystals [30, 31, 87, 116–123] and their defects [124, 125]. XANES/ELNES spectra are particularly important in the case of  $\iota$ - $Al_2O_3$ , because there are few experimental probes available for studying its electronic structure due to the uncertainty and the difficulty involved in obtaining reliable samples. Our modeled structure for  $\iota$ - $Al_2O_3$  with 240 atoms serves as an ideal supercell for OLCAO calculation of the XANES/ELNES spectra. The calculated spectra are the Al-K and Al-L3 and O-K edges of different atoms. Since all atomic sites in the model are non-equivalent, it is not practical to calculate the spectra of all atoms. So, a sufficient number of sites for each group listed in Table 9 are selected and calculated the Al-K, Al-L3, and O-K edges for those selected atoms. The average of these atoms will be the representative spectrum for each group. The average of all spectra for Al

and for O will be what is likely to be observed experimentally if such experiments are ever conducted.

The number of sites selected for each of the 5 groups of  $Al_{oct}$ -A,  $Al_{oct}$ -B,  $Al_{tet}$ -A,  $Al_{tet}$ -B and  $Al_{tet}$ -C are 4, 3, 6, 8, and 3 Al sites respectively; and those for the O-A, O-B, O-C groups are 20, 6, 11 O sites respectively which are also listed in Table 8. XANES calculations were performed on each atom in the sample. The calculated Al-K edge spectra are presented in Fig. 31. The top panel is the weighted average of the groups presented in the lower panels, which are the average spectrum of the atoms within that group. As can be seen, the Al-K spectra from these groups have similarities and differences. Spectra from  $Al_{oct}$ -A and  $Al_{oct}$ -B both have the main double peak at 1580.0 eV, 1582.9 for  $Al_{oct}$ -A and at 1580.7 eV, 1582.8 eV for  $Al_{oct}$ -B, with the later showing a pre-peak at 1576.9 eV.  $Al_{tet}$ -A is the group with the most ideal tetrahedral coordination for all  $Al_{tet}$  and it shows a strong peak at 1579.5 eV whereas  $Al_{tet}$ -B and  $Al_{tet}$ -C have more distorted local structures and their spectra show multiple peaks at different locations. When added together, the top panel shows a main peak at 1579.53 eV and a smaller peak at 1582.8 eV that is contributed to from all five groups, and is the spectrum that is expected from the experimental measurement. Fig. 14 shows the calculated Al-L3 edges in  $\iota$ - $Al_2O_3$  for the same groups as labeled in Fig. 32 for the Al-K edge. The similarities and dissimilarities among the groups bear resemblance to that of Al-K edge. The main features in the averaged spectrum (top panel) are the main peak at 95.7 eV and a pre-peak at 78.7 eV. It is noted that the Al-L3 edges from the group  $Al_{tet}$ -A have a double peak feature in the pre-peak region. Also, the main peak from  $Al_{tet}$ -A is at a relatively lower energy (93.4 eV) whereas those from  $Al_{tet}$ -B and  $Al_{tet}$ -C are at a higher energy (98.0 eV and 99.2 eV). The results for the calculated O-K edges are presented in Fig. 33. The spectra from the anions are fundamentally different from those of the cations since they generally contribute much less

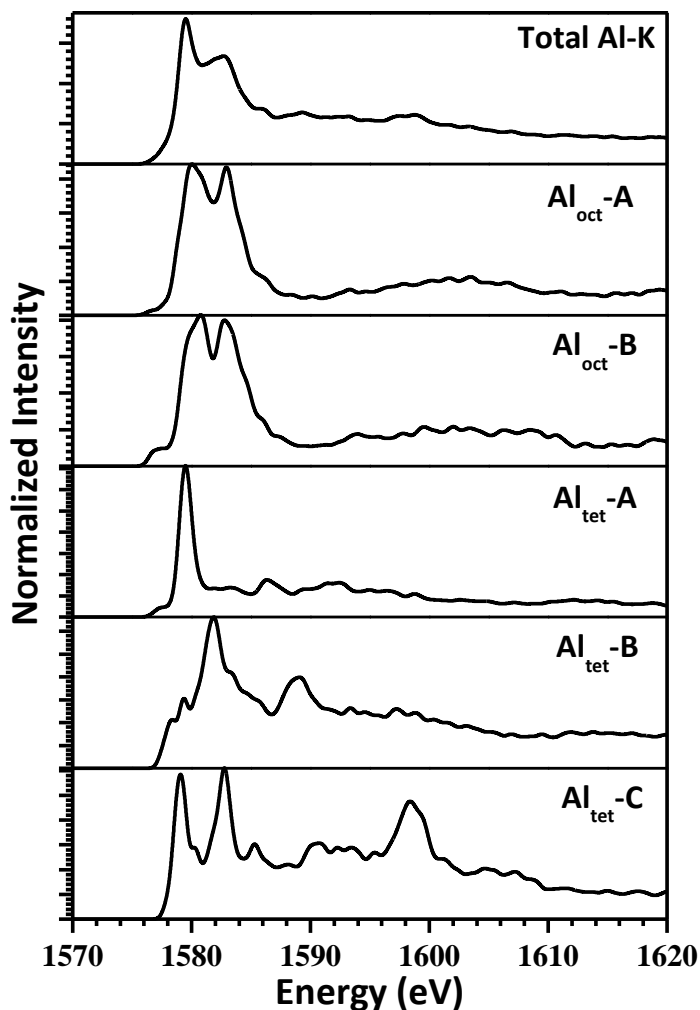


Figure 31. Calculated Al-K edges in  $\nu$ - $Al_2O_3$ . Top panel: averaged Al-K spectra. Bottom panels: average spectra of different groups.

to the unoccupied CB as can be seen from the PDOS of Fig. 10. For  $\nu$ - $Al_2O_3$ , the O-K edge spectra from the three groups O-A, O-B, and O-C show discernible differences because of the differences in their local bonding environment as described in Table 8. When added together, these differences tend to be averaged out and would not be observable in any measured spectra. There two main features in the averaged spectra (top panel), are a rather broadened main peak at 542.4 eV and another peak at 559.0 eV.

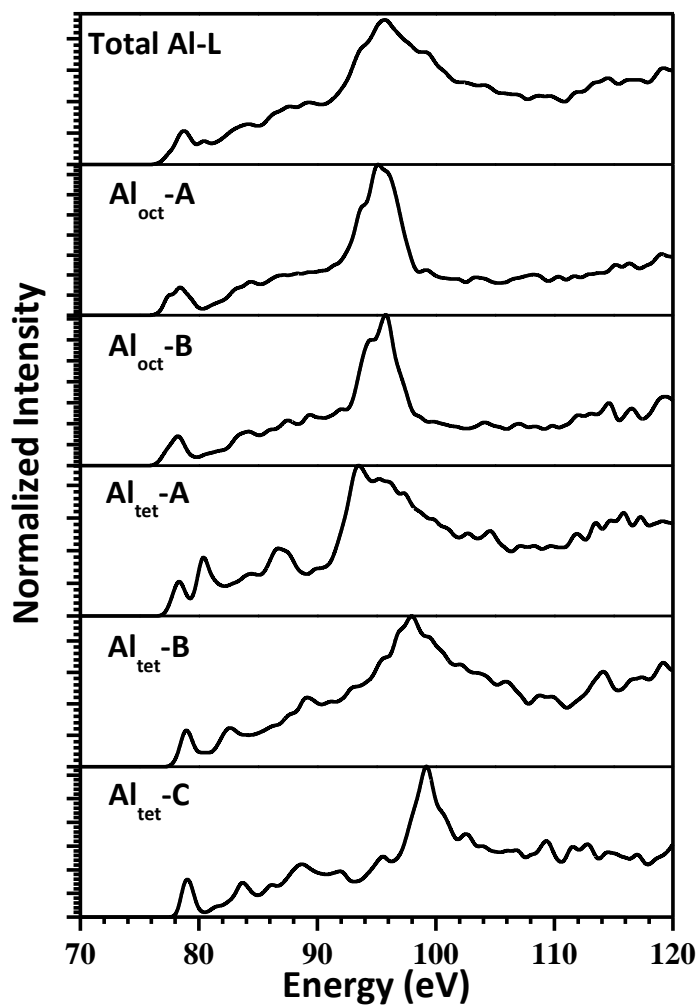


Figure 32. Calculated Al-L3 edges in  $\nu$ - $Al_2O_3$ . Top panel: averaged Al-L3 spectra. Bottom panels: average spectra of different groups.

It is instructive to compare the above spectral data for  $\nu$ - $Al_2O_3$  with that of  $\alpha$ - $Al_2O_3$  [116] and  $\gamma$ - $Al_2O_3$  [25] which have less complicated local structures than  $\nu$ - $Al_2O_3$  and which are easier to interpret. However, such details are beyond the scope of this paper.

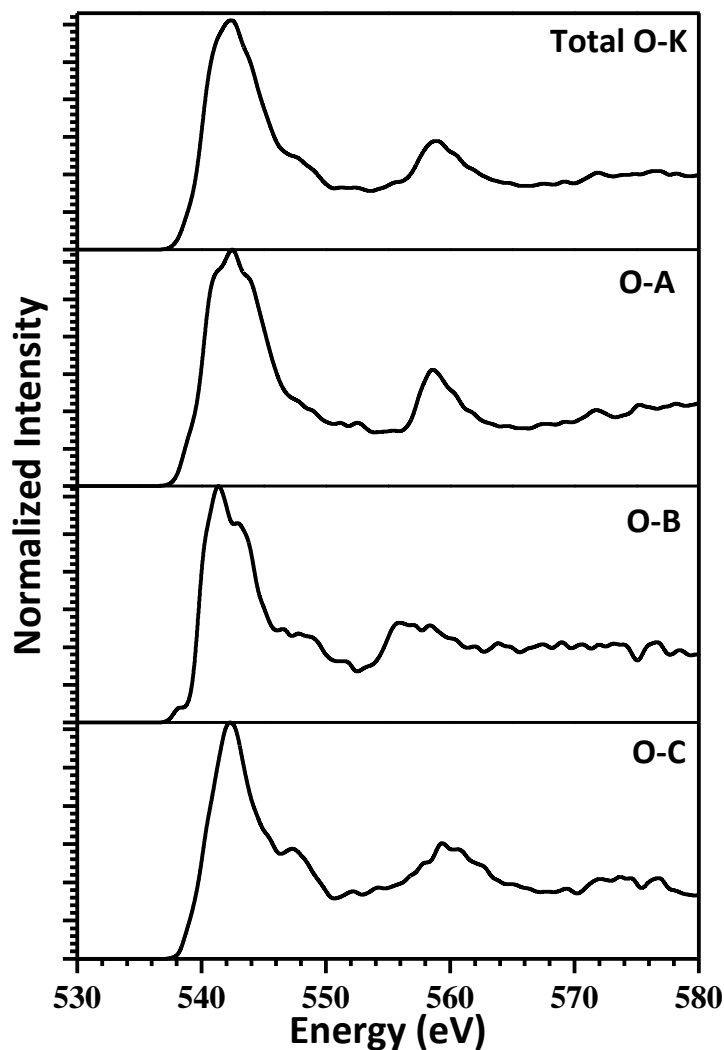


Figure 33. Calculated O-K edges in  $\nu$ - $Al_2O_3$ . Top panel: averaged O-K spectra. Bottom panels: average spectra of different groups

#### 5.4 Summary and Conclusions

Based on the assumption that  $\nu$ - $Al_2O_3$  is a transition alumina which is also the end member of the mullite series that is Si-free, a supercell model is constructed for its structure using the crystal data of high alumina content mullite. The 240-atom orthorhombic cell is highly disordered with a very low density. The fully relaxed model has its simulated x-ray diffraction pattern in excellent agreement with the measured x-ray diffraction pattern

on samples that claim to contain  $\iota$ - $Al_2O_3$ . Using this theoretically constructed model for  $\iota$ - $Al_2O_3$ , a comprehensive *ab initio* study of its physical and spectroscopic properties is completed. The calculated properties include total electronic energy, phonon dispersion relations and phonon density of states, the elastic coefficients and bulk mechanical properties.  $\iota$ - $Al_2O_3$  has a significantly higher total energy and lower density than that of  $\alpha$ - $Al_2O_3$  and  $\gamma$ - $Al_2O_3$ . It is argued that  $\iota$ - $Al_2O_3$  may be an alumina preceding the  $\gamma$ - $Al_2O_3$  phase in the processing of alumina. Calculated elastic stiffness constants and polycrystalline bulk properties are significantly smaller than those of  $\alpha$ - $Al_2O_3$  and  $\gamma$ - $Al_2O_3$ . The phonon dispersion results enables to investigate the thermodynamic properties of  $\iota$ - $Al_2O_3$ , including the pressure and temperature dependent Gibbs free energy. An unusual characteristic of the isothermal bulk modulus at 295 K shows a maximum value at 7.0 GPa strongly suggesting a volume-dependent stability for  $\iota$ - $Al_2O_3$ . The calculated G(P,T) indicates that  $\iota$ - $Al_2O_3$  is a low-pressure high-temperature phase of alumina that less stable than  $\gamma$ - $Al_2O_3$ .

Detailed electronic structure calculations show that  $\iota$ - $Al_2O_3$  is an insulator with a direct band gap of 3 eV. Effective charge distribution confirms that it is a disordered structure and that it has a more ionic bonding character than  $\alpha$ - $Al_2O_3$  and  $\gamma$ - $Al_2O_3$ . The calculated optical absorption and refractive index of 1.652 obtained is in agreement with the reported experimental data. The XANES/ELNES spectra of the Al-K, Al-L3, and O-K edges in  $\iota$ - $Al_2O_3$  which carry the electronic signature of atoms are reported for various groups of Al and O atoms in the model. Their dependence on the local atomic scale structures are critically analyzed and can be compared with those of  $\alpha$ - $Al_2O_3$  and  $\gamma$ - $Al_2O_3$ .

In conclusion, the structure and properties of  $\iota$ - $Al_2O_3$  are fully elucidated, which has evaded full disclosure for a long time. The method and approach used certainly will stimulate investigations on the entire mullite series. As alluded to before,  $\iota$ - $Al_2O_3$  is regarded as an end member of the aluminosilicate solid solution series with the crystal, sil-

limanite, at the other end. Mullite is an important ceramic and refractory material with numerous applications yet there are almost no fundamental theoretical investigations of its properties. Our next goal is to carry out a detailed theoretical study of the different stoichiometric mullite phases and to investigate trends related to how the physical properties change between the end members.

CHAPTER 6  
AMORPHISATION OF BORON CARBIDE ( $B_4C$ )

**6.1 Introduction**

Boron carbide ( $B_4C$ ) in its stoichiometric form is a hard, strong, and light-weight material [8] with a wide variety of applications. It is used in body armor for soldiers, as a neutron absorbent material, for abrasive and wear resistant parts, etc. The stoichiometric boron carbide crystal has a space group of  $R\bar{3}m$  (No.166) [126] with 15 atoms in a rhombohedral primitive cell. It consists of a 12-atom icosahedron of B and a 3 atom chain of C along the body diagonal, and it will be designated as  $B_{12}-CCC$  throughout this paper. Exchanging a C atom in the middle of the chain with a B atom at the polar site of the icosahedron leads to the structure designated as  $B_{11}C-CBC$ . This is generally accepted as the most stable form of  $B_4C$ . [127, 128] Figures 34 and 35 show the  $B_{11}C-CBC$  and  $B_{12}-CCC$  structures in the rhombohedral lattice with the B atoms in the middle of chain and the C atoms highlighted. In both polytypes, the icosahedron has six each of the so-called polar and equatorial sites. Each atom in the icosahedra has 5 nearest neighbor (NN) bonds within icosahedra. The polar atom has one extra bond with a polar atom in another icosahedron and the equatorial atom has one short extra bond with a C atom at the end of the 3-atom chain. The C atoms at the ends of the chains are four-fold bonded with three of the equatorial B atoms in different icosahedra and the central atom in the chain. Bond lengths (BLs) within chain atoms are relatively shorter making the structure stiff along the chain direction. With a very low density and high Hugoniot elastic limit (HEL) of about 22 GPa [8, 129, 130], boron carbide is a very promising material for both personal and vehicle armor. However, boron carbide suffers from a sudden drop in its shear strength when the impact

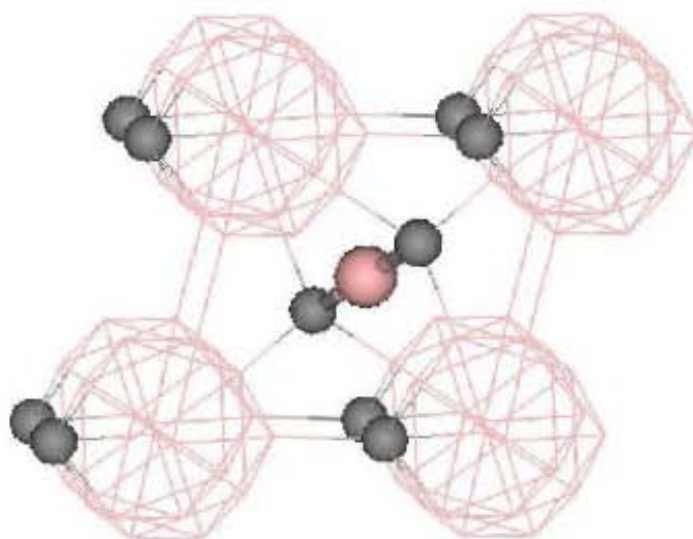


Figure 34.  $B_{11}C$ - $CBC$  structure in the rhombohedral lattice. The small balls in the figures are C atoms and a large ball in the middle of C-B-C chain is B atom

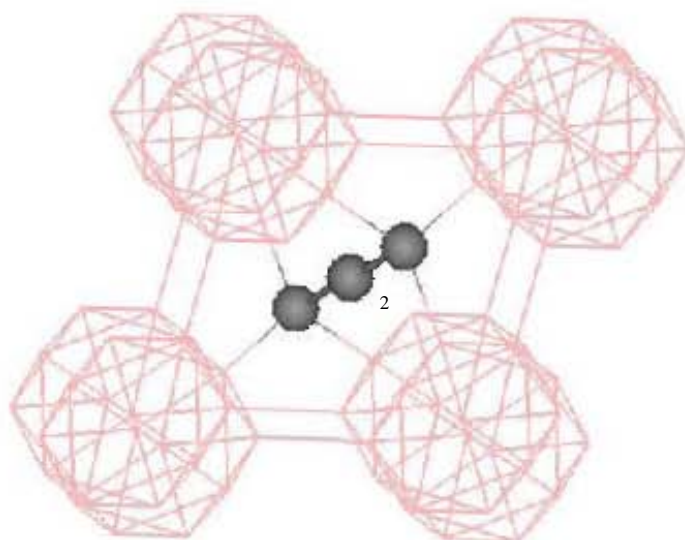


Figure 35.  $B_{12}$ - $CCC$  structure in the rhombohedral lattice. The balls in the figures are C atoms in  $CCC$  chain.

pressure is above the HEL [129, 131, 132]. Post-failure analysis of ballistic experiments indicates that boron carbide undergoes localized amorphization [130]. Amorphization of boron carbide was also observed under different types of nano-indentation [133–135] and under strong electric field [136]. The mechanism of  $B_4C$  amorphization under high velocity impact is a subject of great theoretical and practical interest but it is far from being fully understood even though there have been considerable experimental and theoretical efforts to understand it.

Based on data from low and high temperature Raman spectroscopy, Yan et al. [137] concluded that the destruction of the 3-atom chains leads to an amorphous structure composed of  $sp^2$  bonded aromatic carbon rings and boron clusters with the  $B_{11}C$  icosahedra remaining intact. On the other hand, Fanchini et al. [138], on the basis of Gibbs free energy calculations, argued that  $B_{12}-CCC$  is the most likely polytype that can explain the amorphization of  $B_4C$  because the collapse of the  $B_{12}-CCC$  structure leads to the segregation of  $B_{12}$  icosahedra and carbon atoms to form a 2-3 nm wide amorphous C band in excellent agreement with high resolution electron microscopy (HREM) images of samples recovered from ballistic impact experiments [130]. Fanchini et al. have also suggested the possible transformation of the  $B_{11}C-CBC$  structure into a  $B_{12}-CCC$  structure at high pressure which can then lead to the amorphization of  $B_4C$ . Using Raman and photoluminescence spectroscopy along with Fourier transform infra-red (FTIR) analysis, Ghose et al. [135] concluded that dynamic indentation induced amorphization of  $B_4C$  is due to the collapse of the  $B_{11}C-CBC$  unit cells to form amorphous  $B_{12}$  and C clusters. High pressure experiments using a diamond anvil cell found no pressure induced amorphization in  $B_4C$  for pressures up to 50 GPa [139, 140]. More recently, Yan et al. [141] reported the observation of localized amorphization of  $B_4C$  upon unloading from a high pressure state using in situ high pressure Raman spectroscopy. They concluded that only non-hydrostatic stress

can play a role in the localized amorphization. They have also performed first principles molecular dynamics simulations on a 15-atom rhombohedral unit cell of  $B_{11}C-CBC$  for both hydrostatic and uniaxial compressions along the axial direction. In the hydrostatic compression simulation, up to 60 GPa, a smooth change in volume is observed. However, when compressed along the direction of the C-B-C chain, they found a 4% volume reduction for uniaxial pressure between 18.9 GPa and 22.8 GPa. They related this sudden change in volume to the bending of the 3-atom chain resulting in the amorphization of  $B_4C$ . In a shock wave compression experiment on a highly dense, pure  $B_4C$  polycrystalline sample, Zhang et al. determined the HEL of this sample to be 19.5 GPa and that a large change in the pressure density plot above 38 GPa signaled an onset of a phase transition [142]. However, the exact nature of this high pressure phase was not elaborated.

From these previous efforts to understand the mechanism of amorphization in  $B_4C$ , it is obvious that an unambiguous picture does not emerge and several key questions require clear answers: (1) Can hydrostatic compression lead to amorphization or is the uniaxial compression absolutely necessary? (2) Is the bending of the 3-atom chain the key to amorphization? (3) Does amorphization of  $B_4C$  depend on whether the structure is  $B_{11}C-CBC$  or  $B_{12}-CCC$ ? (4) Is it true that the  $B_{11}C-CBC$  structure reduces to  $B_{12}$  plus amorphous C upon amorphization? (5) How can the amorphous state of  $B_4C$  be unequivocally demonstrated? More importantly, none of the above works made a concerted effort to relate the structure of  $B_4C$ , before and after amorphization, to the fundamental electronic structure and bonding at the atomic level. To answer these questions and provide this relation, accurate large-scale simulations under well controlled conditions in conjunction with atomic scale electronic structure and bonding calculation is necessary. This work presets the results of such simulations using sufficiently large supercell models of  $B_{11}C-CBC$  and  $B_{12}-CCC$  for both hydrostatic and uniaxial compressions.

## 6.2 Methods and Procedures of Simulations

The rhombohedral unit cell of a crystal can be conveniently described using a hexagonal lattice with a cell size three times as large and the hexagonal c-axis aligned with the body diagonal of the original rhombohedral cell. Thus the hexagonal unit cell of  $B_4C$  contains 45 atoms with the 3-atom chain aligned along the crystallographic c-axis. In the present study, a  $2 \times 2 \times 1$  hexagonal supercell with 180 atoms are used for both the  $B_{11}C-CBC$  (Fig. 36) and the  $B_{12}-CCC$  models. It must be emphasized that sufficiently large supercells are necessary for compression studies in order to ensure that the movements of the atoms in the crystal are not restricted by the periodic boundary of the unit cell, which could produce erroneous results. The structural data of the fully relaxed  $B_{11}C-CBC$  and  $B_{12}-CCC$  supercell models are presented in Table 10. The  $B_{11}C-CBC$  model is quite distorted from perfect hexagonal symmetry. It has seven B (B1-B7) and three C (C1, C2, C3) nonequivalent sites. B1, B2, B3, and B4 are equatorial B sites and B5, B6, and B7 are polar sites. B8 is in the middle of the chains between C1 and C2 while C3 is at the polar site of the icosahedron. In the  $B_{12}-CCC$  model, there are only two B sites, the equatorial B (B1) and the polar B (B2). The C1 (C2) atoms are at the ends (middle) of the C-C-C chain. Table 10 also lists the nearest neighbor (NN) BLs for the nonequivalent atoms in both models. Figure 37 shows the sketch of the relaxed supercell model of  $B_{11}C-CBC$  and its projection on the a-b plane. These 180 atom supercell models are large enough to minimize the boundary effect in the total energy and stress related simulations. It also provides flexibility for the formation of new or random bonding patterns due to structural changes under high strain.

Table 10. Crystal structural data of  $B_{11}C-CBC$  and  $B_{12}-CCC$  supercell models.

Lattice	$B_{11}C-CBC$	$B_{12}-CCC$
Constants		
a, b	11.069, 11.087	11.162, 11.162
c	11.907	11.961
$\alpha, \beta$	90.00, 92.075	90.00, 90.00
$\gamma$	120.055	120.00
Non-equivalent sites and their bond lengths in (Angstrom). The integers in parenthesis indicate the number of such bonds.		
B1	1.736, 1.742, 1.779 1.771, 1.60, 1.738	1.735 (2), 1.764 (2) 1.770, 1.644
B2	1.732 (2), 1.775 (2) 1.782, 1.590	1.701, 1.764 (2) 1.770, 1.807 (2)
B3	1.742 (2), 1.772 (2) 1.569, 1.713	
B4	1.732, 1.736, 1.772 1.789, 1.790, 1.596	
B5	1.725, 1.775, 1.779 1.772, 1.779, 1.743	
B6	1.782, 1.813 (2) 1.790 (2), 1.640	
B7	1.725, 1.772, 1.803 1.771, 1.789, 1.813	
B8	1.418, 1.425	
C1	1.425, 1.600 (2), 1.590	1.644 (3), 1.321
C2	1.418, 1.596 (2), 1.569	1.321 (2)
C3	1.640, 1.714, 1.738 (2), 1.743 (2)	

As in the cases of mullite and  $\iota-Al_2O_3$ , two well established *ab initio* methods VASP and OLCAO are used for calculations of various of physical properties of boron carbide. The methods are well described in chapter 3 and will not be repeated here. In this work, VASP is used for structural relaxation of supercell models and for the evaluation of the stress tensor with total energy minimization at each step in the compression simulation.

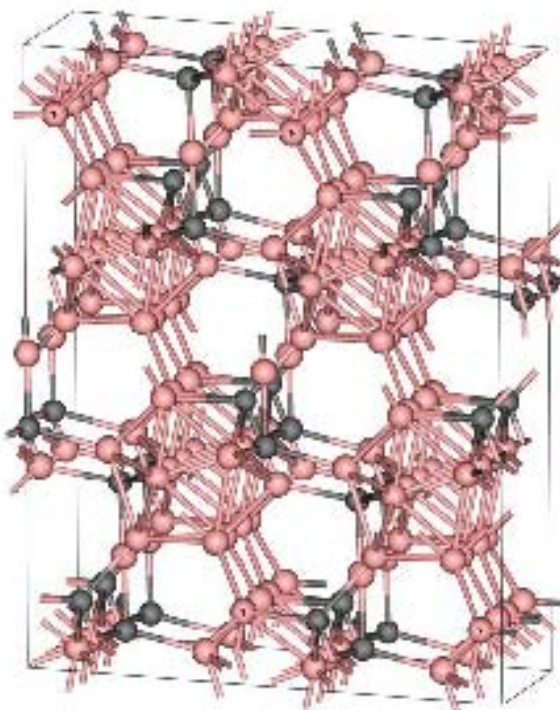


Figure 36. 180-atom supercell model of  $B_{11}C-CBC$  in the hexagonal lattice. The figure is slightly rotated about the c- and a-axes in clockwise direction.

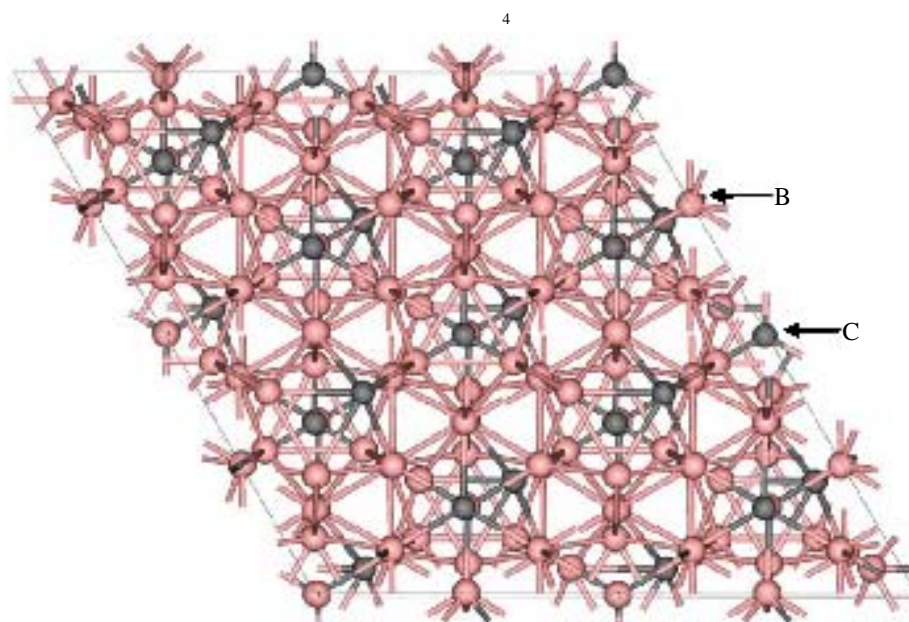


Figure 37. Supercell model of  $B_{11}C-CBC$  in a-b plane.

To ensure high accuracy and in consideration of the large volume change during compression of the structure (and the expected sudden volume change at the phase change), a high cutoff energy of 700 eV, and a small electronic and ionic convergence criterion of  $10^{-7}$  eV and  $10^{-5}$  eV/Å respectively are adopted. Since the 180-atom supercell is fairly large, only the  $\Gamma$  point is used in the k point sampling. Next, the OLCAO method is used to investigate the electronic structure and local bonding of the compressed models by calculating the density of states (DOS), the distribution of effective charges, and their evolutions through the various strained structures. A full basis set consisting of 1s, 2s, 3s, 4s, 2p, 3p, 4p atomic orbitals of B and C was adopted.

Although the primary objective of this study is to investigate the behavior of the  $B_{11}C$ - $CBC$  and  $B_{12}$ - $CCC$  models under uniaxial compression, a hydrostatic compression experiment is also performed in order to compare with the uniaxial compression results and to corroborate with experimental findings. Hydrostatic compressive strain is applied to both supercell models with a 1% volume decrease at each step, and the total energy and hydrostatic pressure are evaluated. For the uniaxial compression simulation, the structure is compressed along the chain direction (c-axis). At each step, the strain is increased by 1% and the structure is fully relaxed with the volume and the shape fixed. Then, the stress tensor and total energy values are extracted. There are two options for the compression simulation, one with constrained lattice vectors in the directions perpendicular to the compression, the other without constraints such that the lattice vectors are allowed to adjust in response to the compression. In this case, the second option is used since it is more realistic and closely mimic the ballistic impact experiments.

### 6.3 Results and Discussion

#### 6.3.1 Results on Hydrostatic Compression

The results of hydrostatic compression on the  $B_{11}C-CBC$  and  $B_{12}-CCC$  models are displayed in Figure 38 and 39 respectively where the hydrostatic pressure and total energy are plotted against the volume strain. Both structures were compressed hydrostatically up to 31 % of their initial volume. The maximum hydrostatic pressure reached in this simulation is 179 GPa (182.5 GPa) for  $B_{11}C-CBC$  ( $B_{12}-CCC$ ). As can be seen in Figure 38 and 39, the total energy varies smoothly in both models, indicating that there are no structural phase transitions involved. This is consistent with the experimental observation of Yan et al. [141] and seems to contradict the conclusion reached by Fanchini et al. [138] that  $B_{12}-CCC$  can transform to an amorphous state under a relatively smaller hydrostatic pressure of about 6 GPa.

#### 6.3.2 Results on Uniaxial Compression

In contrast to the hydrostatic compression simulation, the results from uniaxial compressions are very different. The strain vs. stress plots for the  $B_{11}C-CBC$  and  $B_{12}-CCC$  models are shown in Figure 40. In the  $B_{11}C-CBC$  model, the stress increases almost linearly up to a strain of  $s = 0.23$  and a corresponding stress of 168 GPa, indicating a near-perfect elastic deformation. This very high stress level before amorphization is a result of using a defect free ideal crystal in the simulation and applying the compression along the chain direction. It is unlikely that such a high level can be reached in experiments using real material samples. After this point, there is a sudden and precipitous drop in stress to 20.9 GPa when the strain is increased to  $s = 0.24$  signaling a drastic structural transformation. Beyond  $s = 0.24$ , the stress fluctuates up and down without any particular pattern showing the absence of any residual elasticity in the structure. In the case of  $B_{12}-CCC$  model,

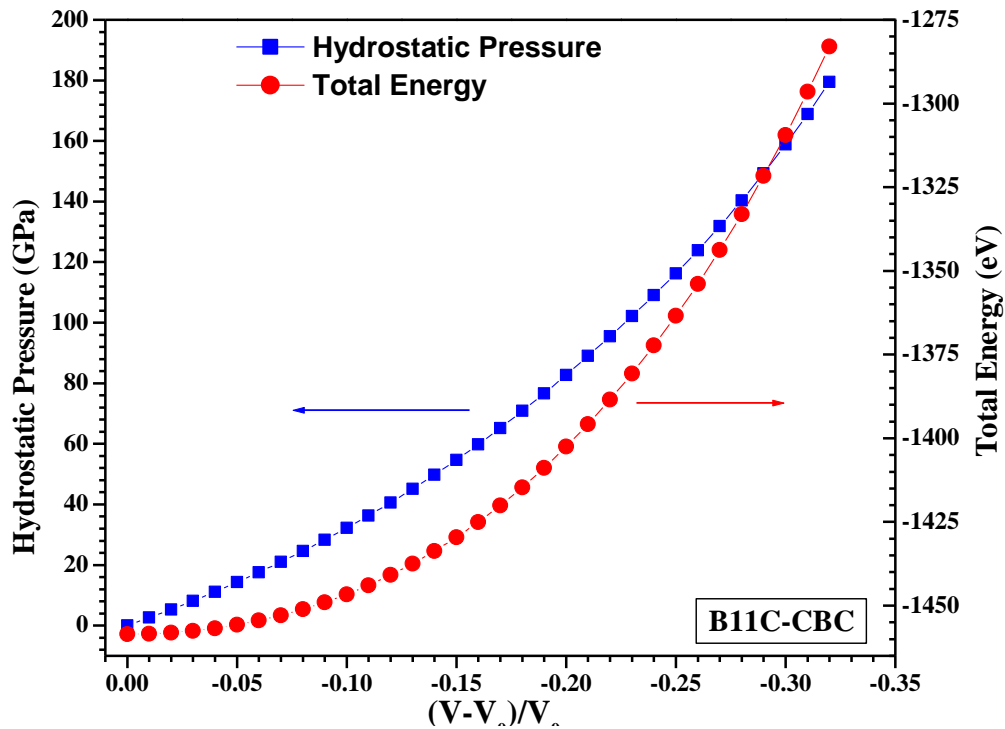


Figure 38. Hydrostatic pressure and total energy vs. hydrostatic strain  $(V-V_0)/V_0$  in  $B_{11}C-CBC$ .

the deformation behavior under uniaxial compression is slightly different. Stress increases linearly up to a strain value of  $s = 0.22$  with a corresponding maximum stress of 151 GPa. There is a sudden drop in stress from  $s = 0.22$  to  $s = 0.23$  suggesting a drastic structural change. However, from  $s = 0.23$  to  $0.24$ , the stress actually rises slightly from 70.2 GPa to 74.5 GPa. This shows that at these strain levels,  $B_{12}-CCC$  model is not fully amorphized and still has some residual elasticity. On further compression, the stress ultimately drops to a minimum value of 26.9 GPa at  $s = 0.26$ , close to the minimum stress in the  $B_{11}C-CBC$  model. After amorphization and beyond  $s = 0.26$ , there is a slight increase in stress and then it appears to fluctuate.

The above results strongly suggest that a drastic collapse in the structure has occurred and that this is associated with a phase transition from a crystalline state to the

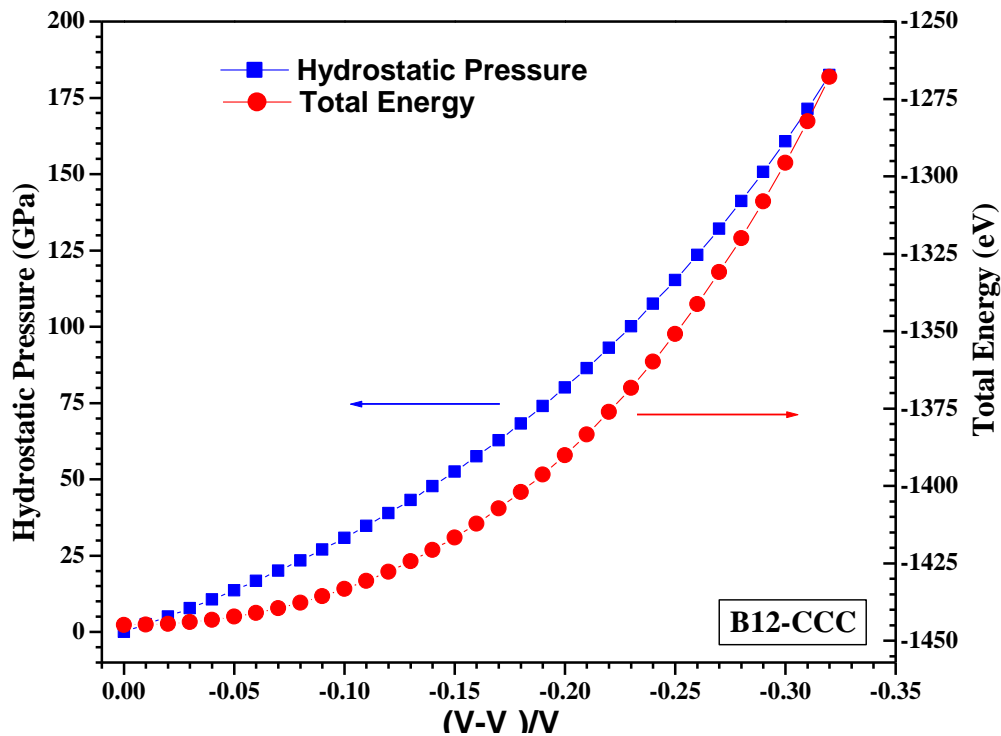


Figure 39. Hydrostatic pressure and total energy vs. hydrostatic strain  $(V-V_0)/V_0$  in  $B_{12}$ - $CCC$ .

amorphous state. This will be verified by critical analysis of both the geometric structure and the electronic structure as presented below. It also shows that the  $B_{11}C$ - $CBC$  model can withstand a uniaxial compressive stress slightly greater than the  $B_{12}$ - $CCC$  model by 17 GPa and at a slightly higher strain. The residual strength observed in  $B_{12}$ - $CCC$  is within a very narrow range of strain between  $s = 0.23$  and  $0.26$ . However, this issue may not play a significant role in what actually happens in ballistic impact experiments. In both models our results clearly show that  $B_4C$  structures can resist a very high uniaxial stress along the chain direction. The maximum stress that the  $B_4C$  models can sustain under uniaxial compression is much larger than the reported HEL. However, in actual ballistic experiments or nano-indentation experiments, it is almost impossible to attain the ideal maximum compression condition as in the simulations. Yan et al. [141] in their diamond

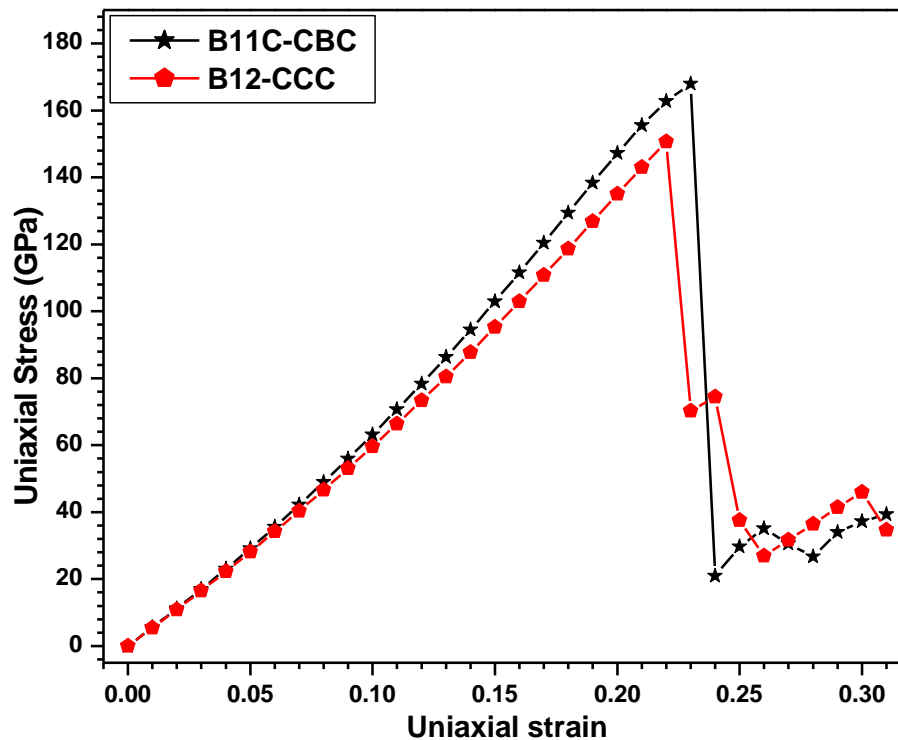


Figure 40. Uniaxial stress vs. uniaxial strain along the crystallographic c-axis in  $B_{11}C-CBC$  and  $B_{12}-CCC$  models.

cell experiment reported the minimum pressure for amorphization of about 25 GPa. It is not clear if the single crystal sample used in the experiments contain any defects or impurities which could significantly reduce the local elastic strengths. These defects may also divert the directional stress to shear stress causing the amorphization to occur at a smaller strain than that from ideal uniaxial compression along the chain direction. They have also performed a compressive MD simulation along C-B-C chain in the 15 atoms  $B_{11}C-CBC$  model and concluded that there is an elastic deformation up to 18.9 GPa and followed by a sudden reduction in volume of about 4%. Their value of 18.9 GPa is almost a factor 10 less than the maximum stress in the present result and is likely affected by the limitation of the small cell they used.

### 6.3.3 Strain-Dependent Elastic Coefficients

Elastic stiffness coefficients ( $C_{ij}$ ) are the best representation of the elastic state and the mechanical strength of crystalline materials. When a material is compressed its elastic state changes. The strain-stress curve discussed above only shows the linear elasticity along the direction of compression. On the other hand,  $C_{ij}$  give not only the linear elasticity in other directions but also provide information on how a material may behave under shear stress. The  $C_{ij}$  values of both  $B_{11}C-CBC$  and  $B_{12}-CCC$  supercell models have been calculated at different uniaxial strains up to the maximum stress before the incipient amorphization using the strain-stress analysis scheme [40]. This method is well described in chapter 3 and will not be repeated here. In general, the strain that is applied in each independent direction is -1.0% or 1.0%. In this case, elastic properties of both  $B_{11}C-CBC$  and  $B_{12}-CCC$  are calculated not only at the equilibrium structures but also at various uniaxially compressed (compressed along the c-axis) structures. Large strain, when applied along the crystallographic c-axis, reduces or increases the compression effect. For small strain, calculation noise starts to be significant, so strains of -0.5% (compression) and +0.5% (stretching) are used for each independent strain element of the crystal while calculating  $C_{ij}$  in both equilibrium structures and compressed structures.

The calculated  $C_{ij}$  values for the unconstrained  $B_{11}C-CBC$  and  $B_{12}-CCC$  supercell models are presented in Table 11. Overall,  $B_{11}C-CBC$  has considerably larger  $C_{ij}$  values than  $B_{12}-CCC$ . In  $B_{11}C-CBC$ ,  $C_{11}$  and  $C_{22}$  are significantly different and larger than  $C_{33}$ . This difference arises from the presence of a C at the polar site and a B atom in the middle of chain that breaks the symmetry. In  $B_{12}-CCC$ ,  $C_{11}$  and  $C_{22}$  are equal and smaller than  $C_{33}$ . Table 11 also lists the measured  $C_{ij}$  values [143] of a carbon deficient single crystal sample of  $B_{5.6}C$  at room temperature. The agreement with our calculated values for the stoichiometric model is reasonable. The measured  $C_{11}$  and  $C_{22}$  values are

between those of  $B_{11}C$ -CBC and  $B_{12}$ -CCC whereas the measured  $C_{33}$  is smaller than the calculated  $C_{33}$  in both models.

Table 11. Calculated elastic constants ( $C_{ij}$ ) of the equilibrium structure of  $B_{11}C$ -CBC and  $B_{12}$ -CCC models (in GPa).

Crystal	$C_{11}$	$C_{22}$	$C_{33}$	$C_{44}$	$C_{55}$	$C_{66}$	$C_{12}$	$C_{12}$	$C_{23}$
$B_{11}C$ -CBC	594.5	580.8	553.1	163.8	168.4	220.6	135.5	76.8	69.9
$B_{12}$ -CCC	521.6	521.7	549.8	137.7	137.7	194.4	133.1	80.4	80.4
B5.6C (exp.) <sup>†</sup>	542.8	542.8	534.5	164.8			130.6	63.5	

<sup>†</sup> Ref. [143]

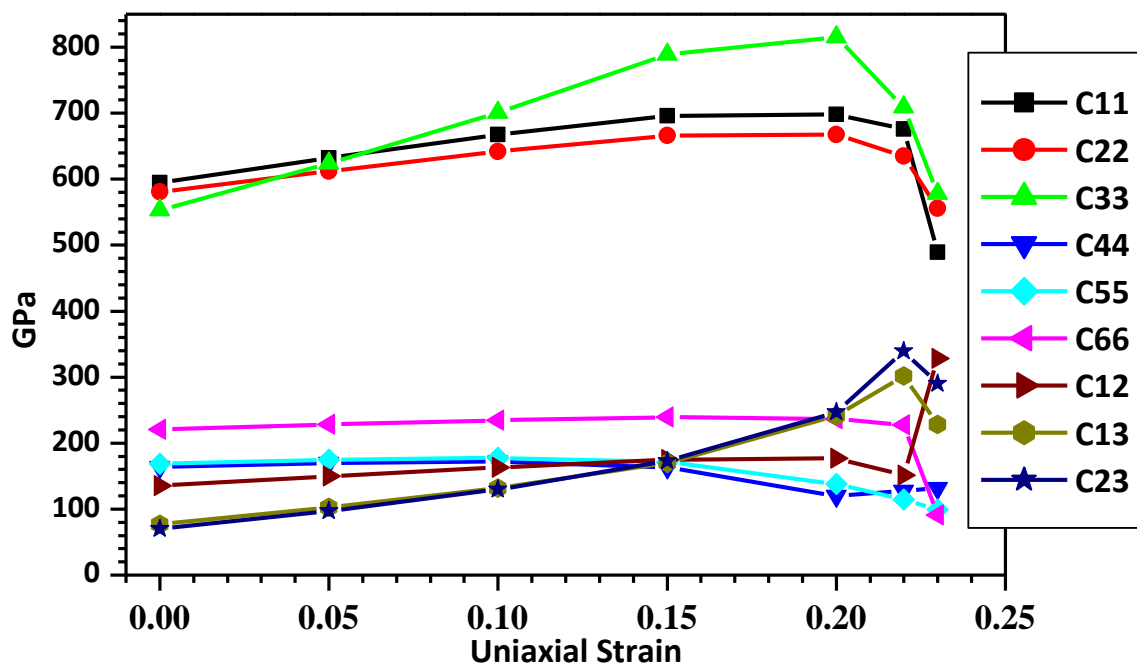


Figure 41. Calculated  $C_{ij}$  values at different uniaxial strains along the crystallographic  $c$ -axis in  $B_{11}C$ -CBC.

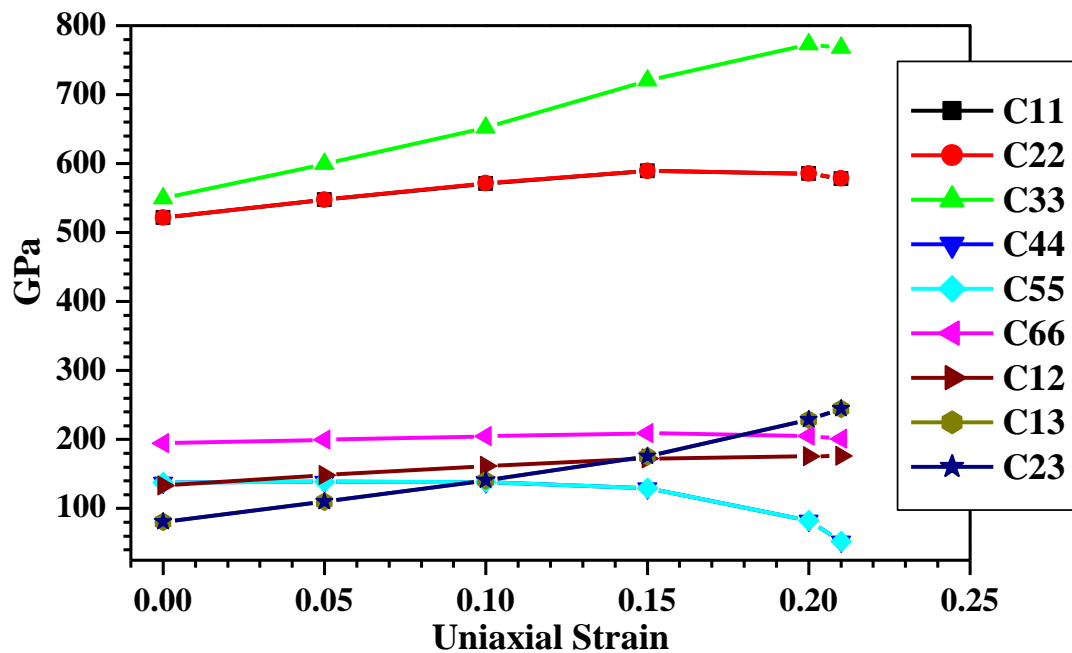


Figure 42. Calculated  $C_{ij}$  values at different uniaxial strains along the crystallographic c-axis in  $B_{12}$ -CCC.

Figure 41 and 42 show the calculated  $C_{ij}$  values of the  $B_{11}C$ -CBC and  $B_{12}$ -CCC supercell models at different uniaxial strains. As the uniaxial strain increases,  $C_{11}$ ,  $C_{22}$  and  $C_{33}$  all increase but the increase in  $C_{33}$  is much faster than others because the strain is along the crystallographic c-axis. When the uniaxial strain reaches 0.20, they start to decrease quite rapidly. On the other hand the shear elastic constants  $C_{44}$ , and  $C_{55}$  remain fairly constant up to the uniaxial strain of  $s = 0.15$ . Beyond strain 0.15, these shear elastic constants start to decrease. The shear elastic constant  $C_{66}$  is almost constant up to the failure point in both polytypes. This result shows the complicated effect of uniaxial compression on the elastic coefficients in  $B_4C$  polytypes. Reduced  $C_{44}$  and  $C_{55}$  values may lead to the failure of the structure at a strain smaller than that indicated in Figure 40. Furthermore, it also shows that both  $B_4C$  polytypes are less resistant to shear strain (stress). It is conceivable that both structures may undergo transformation at a smaller

uniaxial strain depending on stoichiometry and other factors related to the nature of the sample.

#### 6.3.4 Structural Analysis of Supercell Models under Uniaxial Strain

Following sections are used to analyze structural changes in  $B_{11}B-CBC$  and  $B_{12}-CCC$  models under uniaxial compression. The B atom in the middle of the chain in  $B_{11}C-CBC$  model has two unequal B-C bonds because of the presence of the C atom at the polar site of the icosahedra. The evolution of these two B-C bonds as a function of uniaxial strain is plotted in Figure 43. As the compression increases both bonds decrease uniformly and become equal at the strain 0.23. Beyond strain 0.23 where drastic structural change occurs, there is a sudden increase in their BLs and large differences emerge. Figure 44 shows the change in the average C-B-C chain angle with uniaxial strain. The average chain angle is almost constant (close to 180) up to  $s = 0.23$  and then a sudden decrease associated with the bending of the chain takes place. Figures 45 (a) and (b) display snapshots of  $B_{11}C-CBC$  at uniaxial strains of 0.23 and 0.24 respectively. As can be seen, at  $s = 0.23$  the C-B-C chains are almost straight along the crystallographic c-axis and the B11C icosahedra are intact. But at  $s = 0.24$ , the chains are no longer straight and they bend at different angles ranging from 105.7 to 121.7. The B atoms in the middle of the chain now make 1, 2, or 3 extra bonds with other B atoms in different deformed icosahedra. The model at  $s = 0.24$  has a slightly larger lattice constant b than a and the hexagonal structure no longer holds. The B11C icosahedra are highly deformed but not totally broken, suggesting that the bending of the 3-atom chains is the main source of amorphization under uniaxial compression. This is in agreement with the conclusion of ref. [141]. In the  $B_{12}-CCC$  model, the C-C bonds in the 3-atom chain are identical. Figure 46 shows the averages of the C-C bonds as a function of strain which decreases uniformly up to the strain of 0.22. Beyond  $s = 0.22$ , the C-C BLs

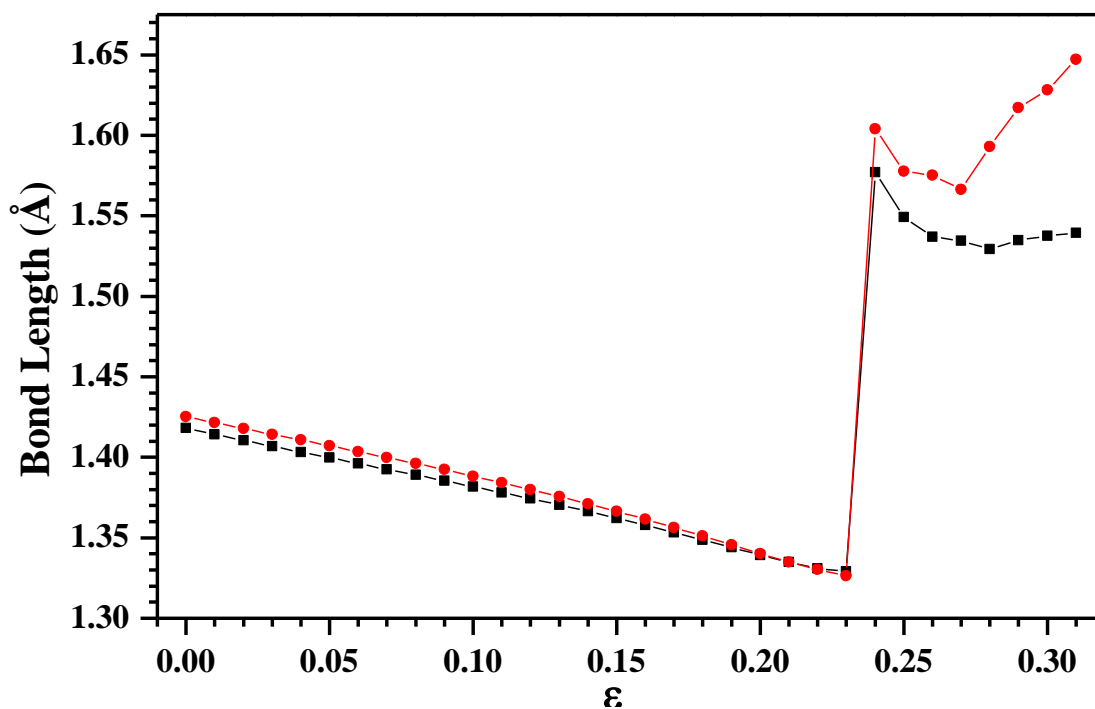


Figure 43. Average bond length in CBC chain vs. uniaxial strain ( $\epsilon$ ) in  $B_{11}C-CBC$ .

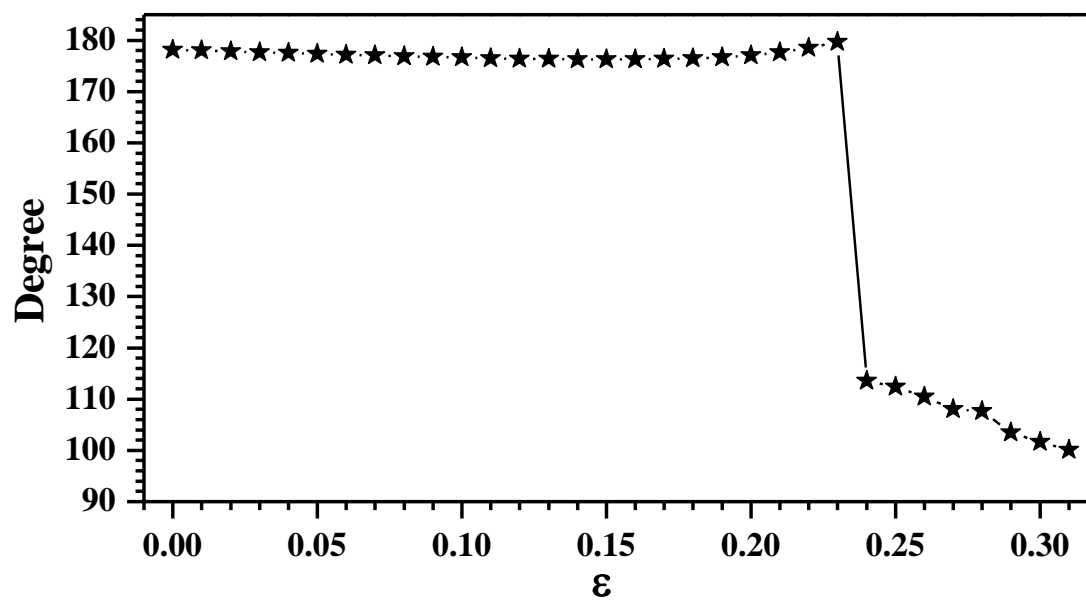


Figure 44. Average CBC chain angle vs. uniaxial strain ( $\epsilon$ ) in  $B_{11}C-CBC$ .

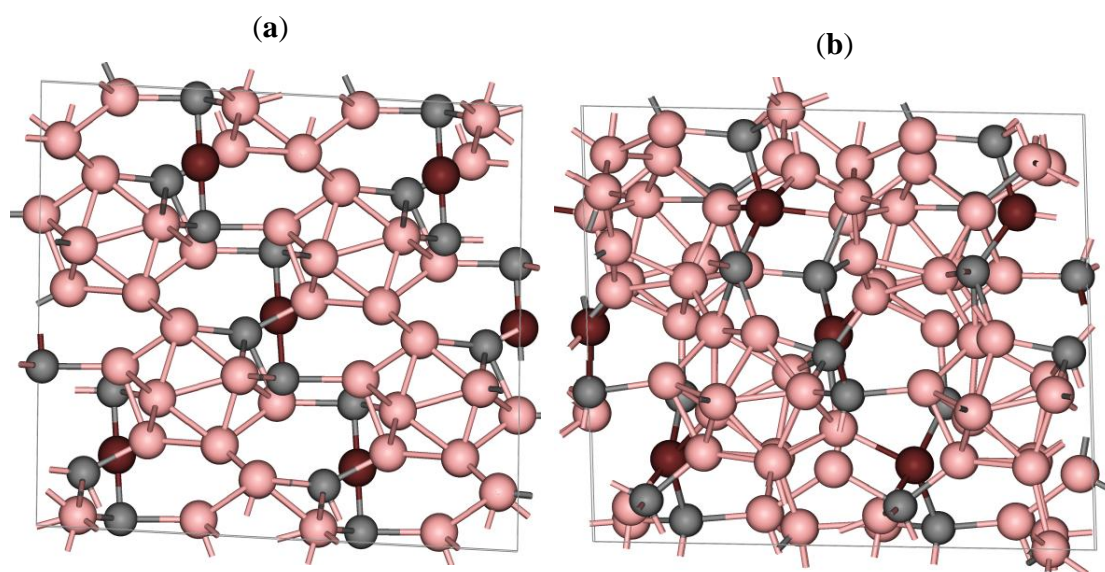


Figure 45. Atomic configurations in  $B_{11}C$ - $CBC$  model at different uniaxial strains. B atoms in the middle of chains are colored differently for easy visual distinction. (a) At strain 0.23; (b) at strain 0.24. (Pink=B in icosahedra; Grey=C; Dark Violet=B in chain)

suddenly increase and are no longer identical. Figure 47 shows the change in the average C-C-C chain angle under uniaxial compression. They are perfectly straight until the strain reaches 0.22. Beyond  $s = 0.22$  at  $s = 0.23$  and  $s = 0.24$ , some of the chains start to bend. At  $s = 0.25$  and beyond in the amorphous region, the average angle is about 60 indicating the formation of triangular carbon units. Figure 48 shows the snapshots of the  $B_{12}$ - $CCC$  model at the strains of 0.22 to 0.25. The C-C-C chains are perfectly straight along the c-axis at  $s = 0.22$  and the  $B_{12}$  icosahedra are somewhat undistorted. At  $s = 0.23$  and 0.24, some of the chains are still straight but inclined from the axial direction and the rest are bent. The average chain angle of the bent C-C-C chains at strains 0.23 and 0.24 are 117.6 and 116.3 which are close to the average angle of the bent C-B-C chains in the  $B_{11}C$ - $CBC$  model at  $s = 0.24$ . This implies that the intermediate residual elastic strength in  $B_{12}$ - $CCC$  at strains between 0.22 and 0.24 is due to the fact that some of the chains tend to incline instead of

bend. When the C-C-C chain bends, the middle C atom makes one extra bond with a B atom in the  $B_{12}$  icosahedron. When the C-C-C chain inclines, it loses one C-B bond to an icosahedron. In this process of breaking and forming new bonds,  $B_{12}$  icosahedra are distorted and the structure undergoes an irreversible change. At strain 0.25, the bent C-C-C chains form near perfect triangles with each C atom making two other C-B bonds. In this amorphous region, the icosahedra are severely deformed with some intra-icosahedral B-B bonds being broken.

A structural phase transition is always accompanied by a large change in total energy and volume. Figures 49 and 50 shows the total energy and volume changes with uniaxial compression in  $B_{11}C-CBC$  and  $B_{12}-CCC$  respectively. In both cases, total energy increases smoothly and the volume decreases linearly until they reach their respective strains needed for amorphization. In  $B_{11}C-CBC$ , there is a 12.8% volume increase and

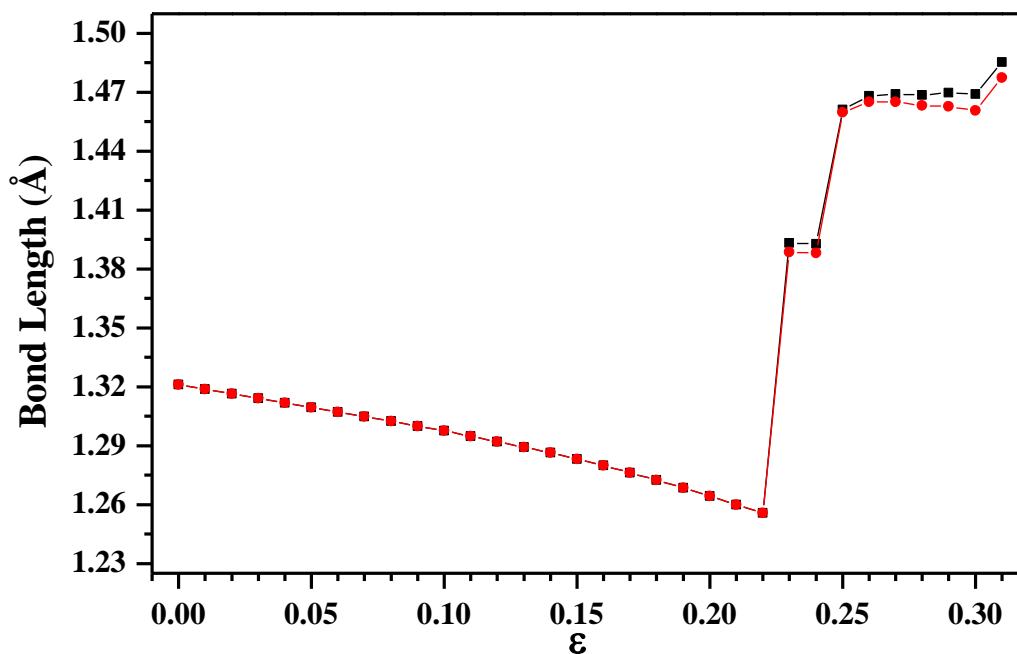


Figure 46. Average bond length in CBC chain vs. uniaxial strain ( $\epsilon$ ) in  $B_{12}-CCC$ .

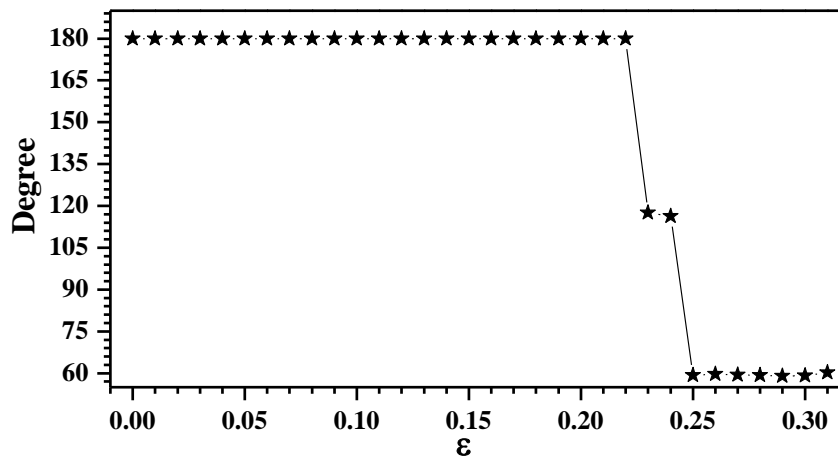


Figure 47. Average CBC chain angle vs. uniaxial strain ( $\epsilon$ ) in  $B_{12}$ - $CCC$ .

a 4.8% total energy decrease between  $s = 0.23$  and  $s = 0.24$ . These changes in volume and total energy are rather large, a manifestation of fundamental structural variation. Similarly, in  $B_{12}$ - $CCC$  there is a 4% volume increase and a 2.3% total energy decrease from  $s = 0.22$  to  $s = 0.23$ , and a further 10.6% volume increase and a 3.4% total energy decrease from  $s = 0.22$  to  $s = 0.25$ . It is generally expected that a sudden drop in the elasticity of the structure should result in an expansion in the unconstrained directions.

### 6.3.5 Evidence of Amorphization: Radial Pair Distribution Function

It is clear from the results shown above that both  $B_{11}C$ - $CBC$  and  $B_{12}$ - $CCC$  structures of  $B_4C$  suffer catastrophic structural changes beyond the uniaxial strains of 0.23 and 0.22 respectively. So the question arises, is there additional clear and unequivocal evidence for the formation of an amorphous structure. A traditional way to distinguish the crystalline and amorphous structures is to calculate their radial pair distribution function (RPDF). Figure 51 shows the RPDF plots of  $B_{11}C$ - $CBC$  model at uniaxial strains of 0.00, 0.23, and 0.24. At  $s = 0.00$  the structure is unstrained so the RPDF is that of a perfect  $B_4C$  crystal with well-defined peaks corresponding to different B-C, B-B, and C-C separations.

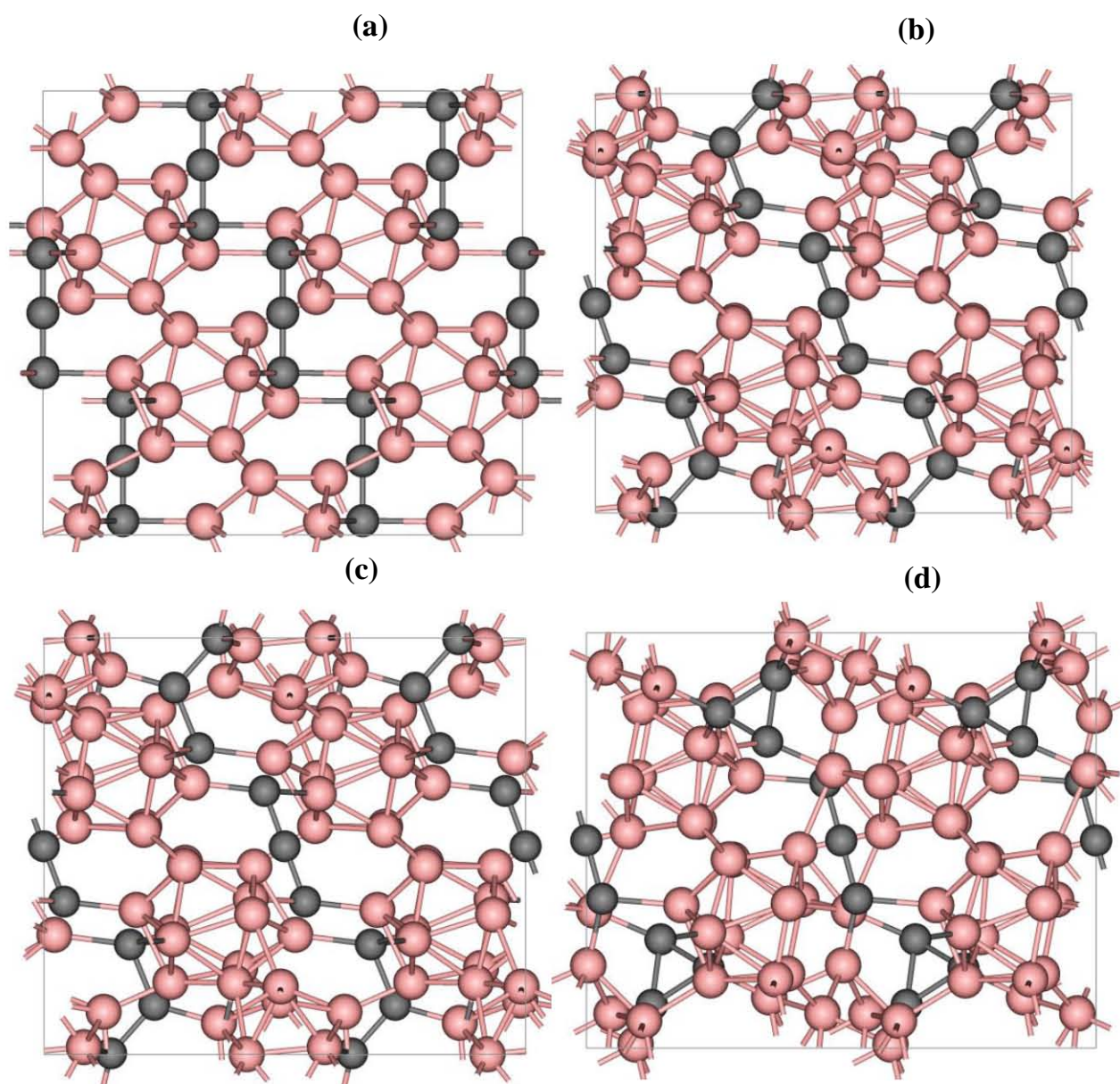


Figure 48. Atomic configurations in  $B_{12}$ - $CCC$  model at different uniaxial strains. (a) At  $s = 0.22$ , (b) at  $s = 0.23$ , (c) at  $s = 0.24$  and (d) at  $s = 0.25$ . (Pink=B; Grey=C)

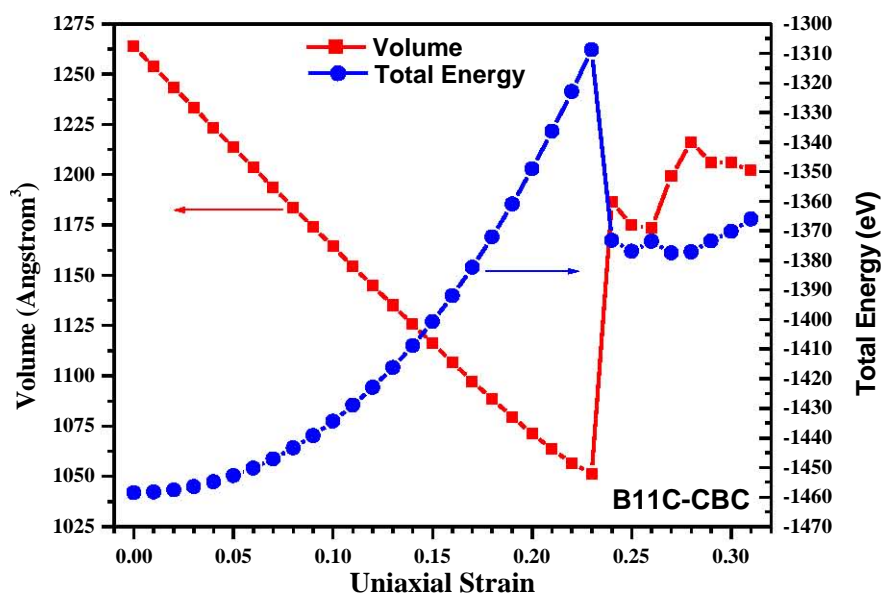


Figure 49. Change in volume and total energy with uniaxial strain along the crystallographic  $c$ -axis in  $B_{11}C-CBC$ .

At the high strain of  $s = 0.23$ , these structures in the RPDF are clearly visible showing that the long range order associated with the crystallinity of the structure has persisted. The compression resulted only in a slight broadening of the peaks. However, at  $s = 0.24$ , the distinctive sharp peaks all disappear and the resulting RPDF has highly broadened peaks characteristic of an amorphous solid. Similar trends can be observed in the RPDF plots of the  $B_{12}-CCC$  model. The RPDF plots of  $B_{12}-CCC$  at strains of 0.00, 0.22, and 0.23 are shown in Figure 52. At strains 0.00 and 0.22, the RPDF plots have well defined peak features displaying long range order in the structure. At strain 0.23, the long range order disappears. Unlike in  $B_{11}C-CBC$ , the  $B_{12}-CCC$  model shows some short range order even after amorphization due to the formation<sup>47</sup> of triangular C units discussed above.

### 6.3.6 Evidence of Amorphization: Electronic Structure and Bonding

Another very effective way to investigate the amorphization in  $B_4C$  is to calculate quantum mechanically the effective charge ( $Q^*$ ) on each atom in the model using the OL-CAO method with a minimal basis set.  $Q^*$  is the valence electronic charge associated with a particular atom in the crystal calculated according to the Mullikan scheme [38]:

$$Q_\alpha^* = \sum_i \sum_{n,occ} \sum_{j,\beta} C_{i\alpha}^{*n} C_{j\beta}^n S_{i\alpha,j\beta} \quad (6.1)$$

In Eq. 6.1,  $C_{nj}$  are the eigenvector coefficients of the  $n^{th}$  band,  $j^{th}$  orbital and  $i^{th}$  atom, and  $S_{i\alpha,j\beta}$  are the overlap integrals between the  $i^{th}$  orbital of the  $\alpha^{th}$  atom and  $j^{th}$  orbital of the  $\beta^{th}$  atom. The deviation of  $Q^*$  from the charge of the neutral atom shows the gain or loss of charge as a consequence of interatomic interaction and provides important information about the structure at the atomistic level. Figure 53 shows the effective charge

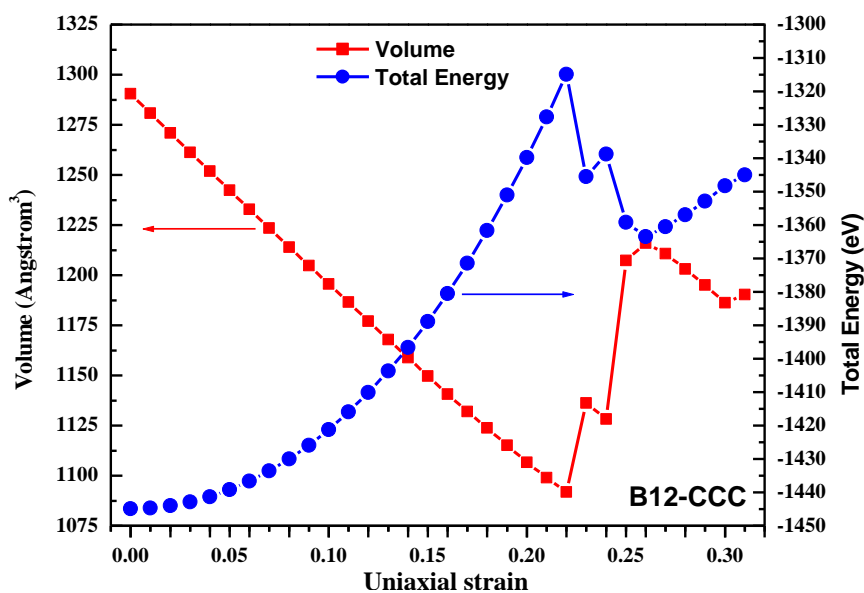


Figure 50. Change in volume and total energy with uniaxial strain along the crystallographic  $c$ -axis in  $B_{12}$ - $CCC$ .

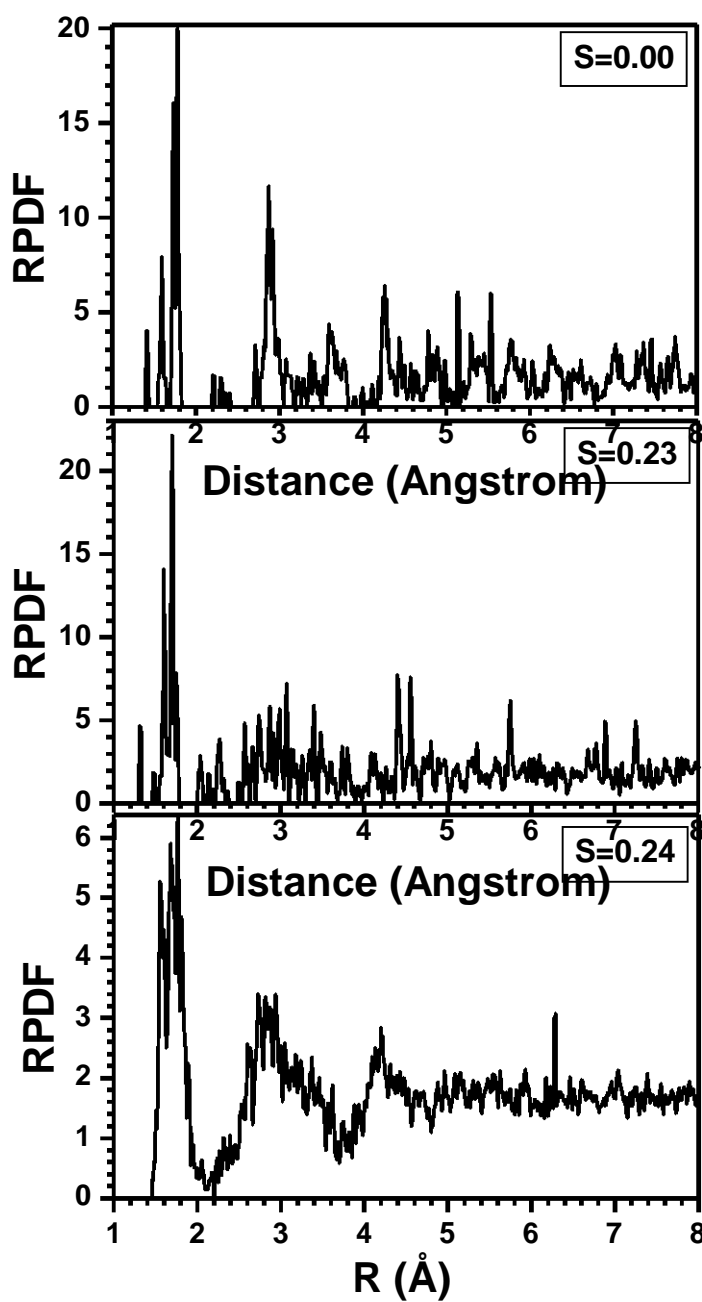


Figure 51. RPDF plots of  $B_{11}C-CBC$  model at different uniaxial strains ( $s$ ) along the crystallographic  $c$ -axis.

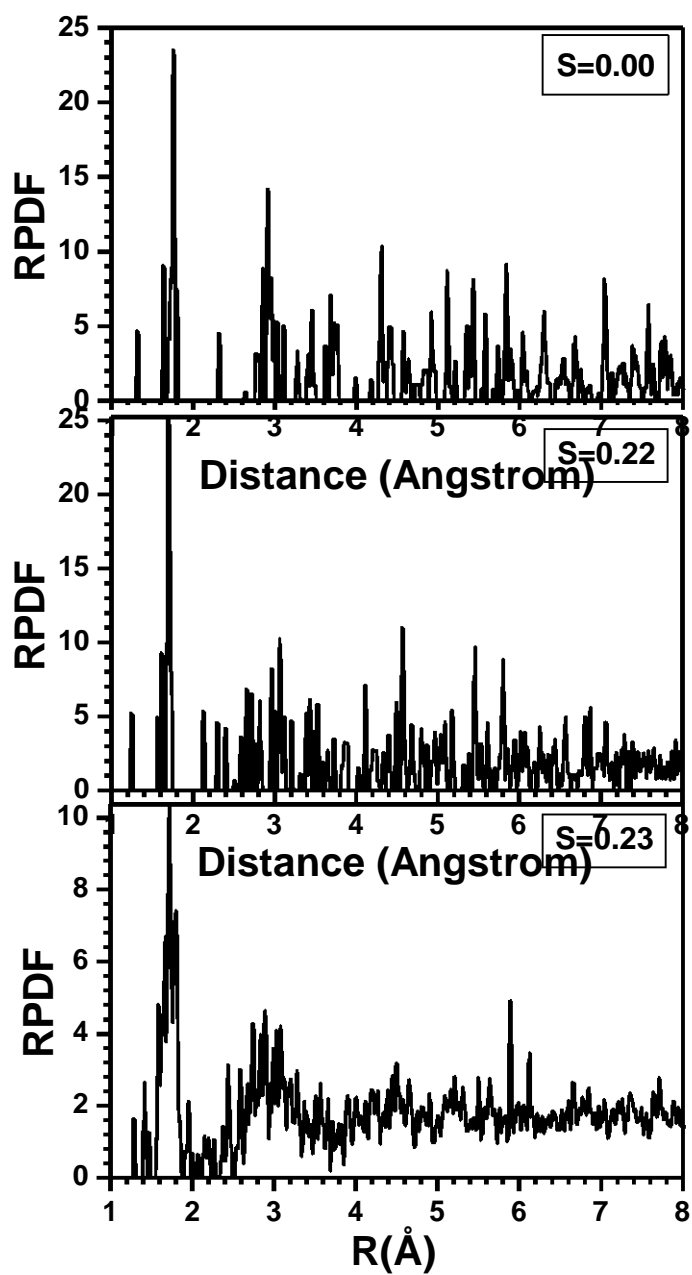


Figure 52. RPDF plots of  $B_{12}$ -CCC model at different uniaxial strains ( $s$ ) along the crystallographic  $c$ -axis.

distribution of the 180 B and C atoms in  $B_{11}C$ - $CBC$  model at different strains of  $s = 0.00$ ,  $0.23$ , and  $0.24$ . Atoms numbered 1 to 72 are the equatorial B atoms; atoms numbered 73 to 132 are polar B atoms; atoms from 133 to 144 are the B atoms in the middle of the chain; atoms 145 to 168 are C atoms in the chain and those from 169 to 180 are the C atoms at the polar sites of the icosahedra. Horizontal lines at 3 and 4 represent the electron charge of the neutral B and C atoms to facilitate in identifying charge gain or loss. On average, B atoms lose charge to C atoms. At strain 0.00, the  $Q^*$  distribution shows 4 groups for equatorial B and 3 groups for polar B. These subgroups within the equatorial or polar sites in the icosahedra occur because of the presence of a C atom in one of the polar sites which breaks the icosahedral symmetry. The process of gaining or losing charge by B atoms in  $B_{11}C$  icosahedra appears to be quite complicated. The B atoms in the middle of the chain which have short B-C bonds lose a relatively large amount of charge. Among the C atoms, the polar C atoms which have longer bonds gain a smaller amount of charge. At a strain of 0.23 before amorphization, differences in the  $Q^*$  among the B atoms within the icosahedra have widened because of increased influence of the polar C atoms. An unusual feature at  $s = 0.23$  is that the atoms numbered 61 to 84, which originate from polar and equatorial B atoms, have almost equal  $Q^*$ . This reflects a decrease in the distinction between equatorial and polar sites at higher strains. At a strain of 0.23, the B atoms in middle of the chains have gained a significant amount of charge but still retain their own identity. Furthermore, the difference in  $Q^*$  of the chain C atoms is diminished which is consistent with the observation in the average BL plots (Figure 43). The most conspicuous feature of the effective charge distribution is at strain 0.24. The  $Q^*$  of B atoms are widely scattered showing no trace of any group identity. Similarly, polar C and chain C atoms have lost their distinction. All the atoms in the structure have different and widely distributed values of  $Q^*$ , an unequivocal signature of amorphization. Similar analysis of the effective charge distribution in the

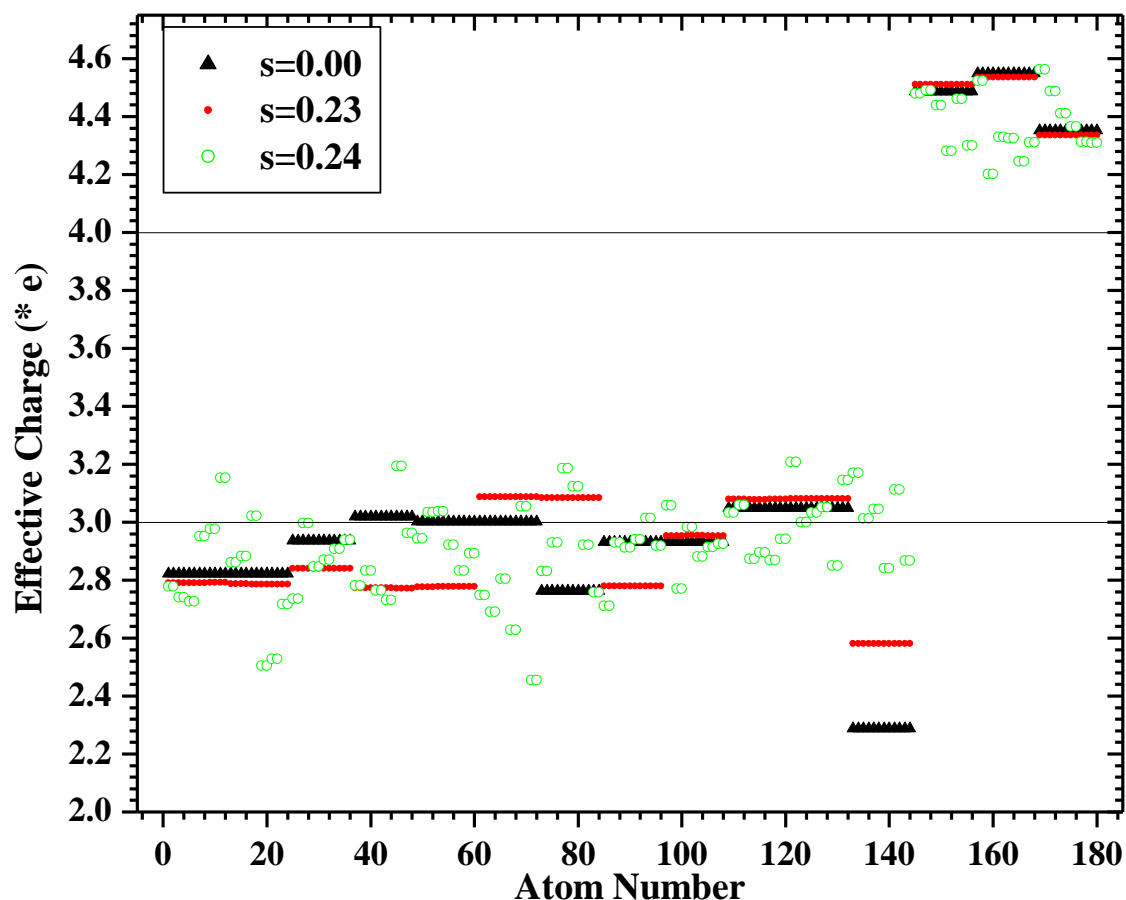


Figure 53. Distribution of effective charge  $Q^*$  at uniaxial strains ( $s$ ) of 0.00, 0.23, and 0.24 in  $B_{11}C$ - $CBC$  model. Horizontal lines at 3.0 and 4.0 represent the number of valence electrons in neutral B and C atoms respectively.

$B_{12}$ - $CCC$  supercell model at different strains is presented in Figure 54. The atoms are labeled as follows: equatorial B atoms (0 to 72), polar B atoms (73 to 144), C atoms at the ends of the chain (145 to 168) and at the center of the chain (169-180). At  $s = 0.00$ , all  $Q^*$  values are distinct and well separated. Equatorial B atoms have lost some of their charges whereas polar B atoms have gained slightly. The C atoms at the middle of the C-C-C chains, which have short bonds with other C atoms, have lost charge significantly.

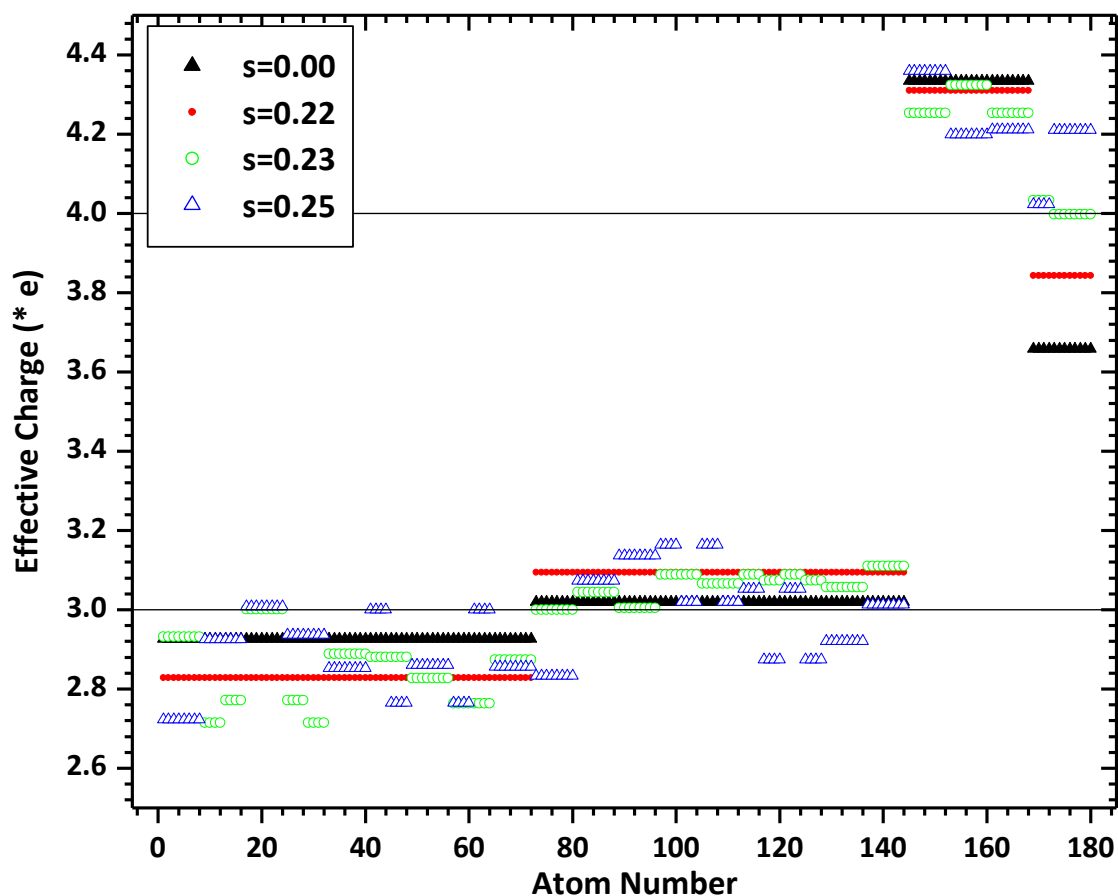


Figure 54. Distribution of effective charge  $Q^*$  at uniaxial strains ( $s$ ) of 0.00, 0.22, 0.24, and 0.25 in  $B_{12}$ - $CCC$  model. Horizontal lines at 3.0 and 4.0 represent the number of valence electrons in neutral B and C atoms respectively.

On the other hand, the C atoms at the ends of chain, which have relatively short bonds with equatorial B atoms, gain a larger amount of charge. At strain  $s = 0.22$ , the difference in  $Q^*$  between equatorial and polar B widens but they still maintain their own identity. At strains 0.23 and 0.25 all long range order in the structure is lost and one would expect the  $Q^*$  distribution to be widely scattered as in the  $B_{11}C$ - $CBC$  model. However, the calculated  $Q^*$  distribution shows that the  $B_{12}$ - $CCC$  model still maintains some kind of short range

order. This is consistent with the RPDF plots shown in Figure 52.

To further confirm the amorphization of  $B_4C$  under uniaxial compression and to observe the evolution of electronic structure, total density of states (TDOS) of both  $B_{11}C-CBC$  and  $B_{12}-CCC$  models have been calculated at different strains using the OLCAO method with a full-basis set. The results are displayed in Figures 55 and 56. The TDOS can be resolved into partial components, or PDOS, of different atomic and orbital origins (not shown here). These two models have quite different TDOS features.  $B_{12}-CCC$  has a strong peak in the middle of the band gap originating from the 2p orbitals of C atoms in the middle of chain. In both models, the upper part of the valence band (VB) is dominated by B atoms and lower part by C atoms. In the conduction band (CB) region, the TDOS features are mostly dominated by B atoms.  $B_{11}C-CBC$  and  $B_{12}-CCC$  both have indirect band gaps (The calculated band structures are not presented here). At strain 0.00,  $B_{11}C-CBC$  has a band gap of 2.76 eV which is significantly smaller than that found for  $B_{12}-CCC$  which is 4.06 eV, if the strong peak is considered to be in the middle of the gap. If the gap states are considered to be part of the unoccupied CB, a direct band gap of 1.26 eV is obtained. Previously, Li and Ching [144] calculated band structure of the  $B_{11}C-CBC$  model using an older version of the OLCAO method and reported an indirect band gap 3.03 eV. The difference is attributed to the slightly better basis set used and a more accurate potential representation in the present calculation. Also the structure of the present  $B_{11}C-CBC$  supercell model is a fully relaxed model instead of the experimental structure. There are plenty of calculations [145, 146] that report band gaps of  $B_{11}C-CBC$  or  $B_{12}-CCC$  polytypes but most of them are larger than the recently reported band gap value of about 2.1 eV [147, 148]. On the other hand, the direct band gap of 1.56 eV presented by Dekura et al.[149], taken from the top of VB to the bottom of the mid gap DOS feature, is slightly larger than our value of 1.26 eV. It should be pointed out that any measured gap value for

$B_4C$  has a large degree of uncertainty due to the defective nature and non-stoichiometric composition of the sample. Figures 55 and 56 show that as compression increases, the band gap decreases and the upper VB broadens. The band gap values of  $B_{11}C-CBC$  at strains of 0.10, 0.15, 0.20, and 0.23 are 2.30 eV, 1.95 eV, 1.20 eV, and 0.55 eV respectively.

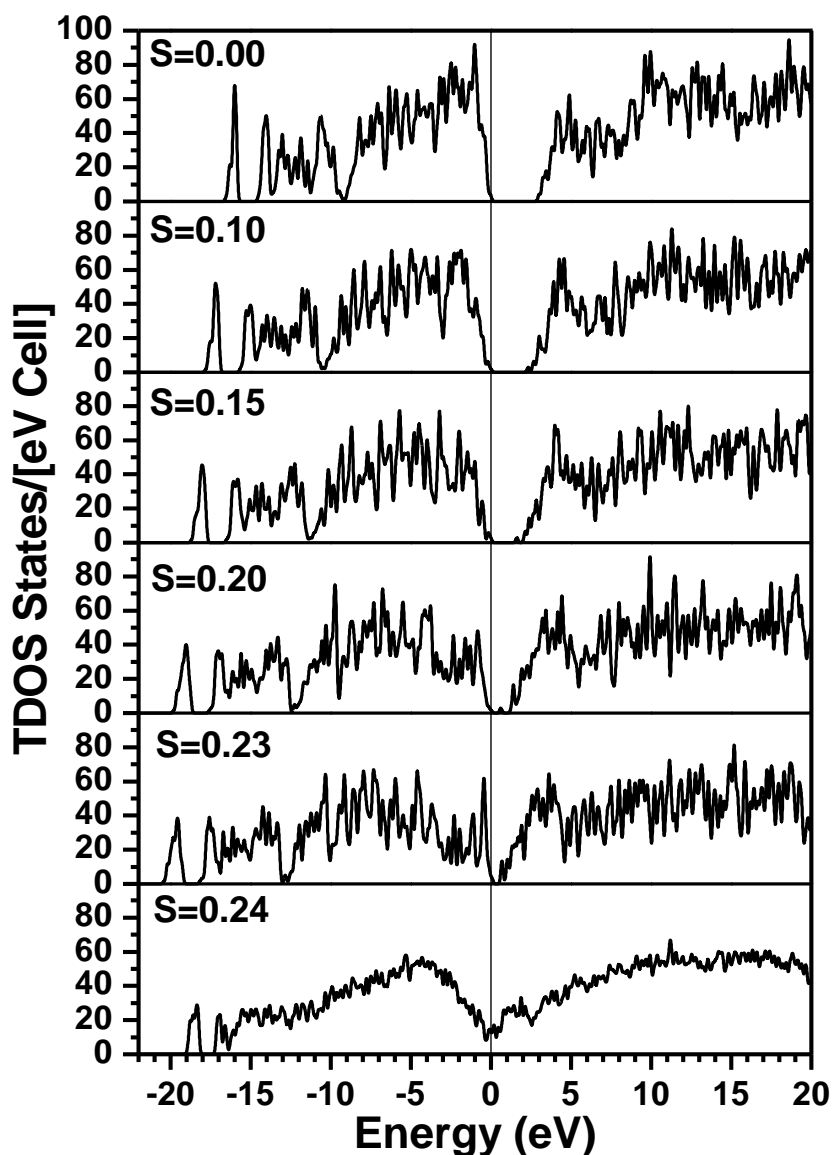


Figure 55. Calculated total density of states (TDOS) of  $B_{11}C-CBC$  model at different strains ( $s$ ). Vertical line represents top of the VB which is set to zero eV

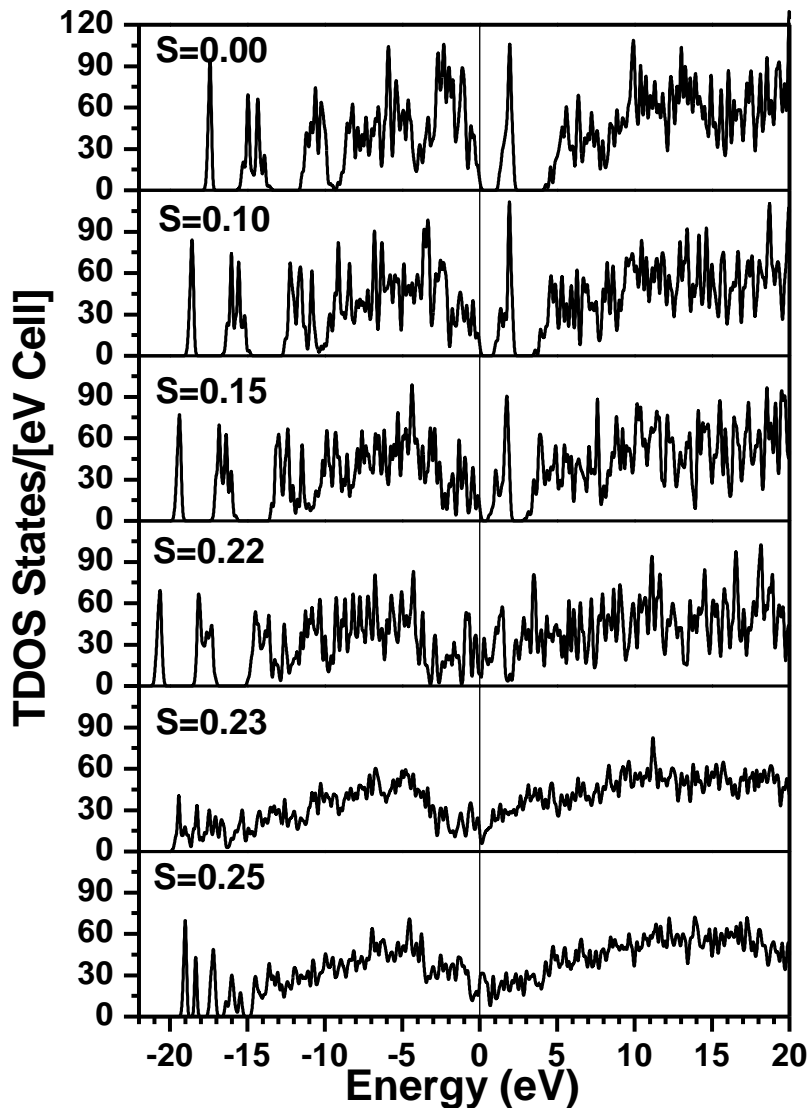


Figure 56. Calculated total density of states (TDOS) of  $B_{12}\text{-CCC}$  model at different strains ( $s$ ). Vertical line represents top of the VB which is set to zero eV

At a strain of  $s = 0.24$  the band gap completely disappears and the DOS shows the features typical of an amorphous solid. The pattern of evolution of the TDOS in the  $B_{12}\text{-CCC}$  model is similar to that of  $B_{11}\text{C-CCC}$ . Band gaps for  $B_{12}\text{-CCC}$  at strains of 0.10, and 0.15 are 3.48 eV, and 2.82 eV respectively. At a strain  $s = 0.22$ , the band gap almost

disappears but the TDOS still shows crystalline features. Beyond the strain of 0.22, the TDOS features are quite broadened and clearly show the amorphous nature of the structure.

### 6.3.7 Summary and Conclusions

*Ab initio* compression simulations are performed on large supercell models of  $B_4C$  ( $B_{11}C-CBC$  and  $B_{12}-CCC$ ) for both hydrostatic and uniaxial compressions. Under hydrostatic compression, smooth changes in pressure and total energy were observed up to a very high strain of 0.32 and there is no sign of abrupt structural change to an amorphous state. On the other hand, when compressed along the uniaxial chain direction, the structure undergoes a massive structural change to an amorphous state at a uniaxial strain of 0.23 (0.22) for the  $B_{11}C-CBC$  ( $B_{12}-CCC$ ) model. The change in total energy and volume at the point of amorphization is large and discontinuous, so it can be classified as a first order phase transition. The maximum stress that the  $B_{11}C-CBC$  ( $B_{12}-CCC$ ) model can withstand is 168 GPa (152 GPa). The  $B_{12}-CCC$  model shows some residual strength at strains 0.23 and 0.24. The amorphization of the  $B_4C$  crystal is further confirmed by detailed analysis of the evolution of the RPDF, TDOS, and the distribution of effective charges in both models. In both cases and just before amorphization, the icosahedra remain intact and all the 3-atom chains are straight along the c-axis. After amorphization, the icosahedra are still identifiable but severely distorted due to the formation of new bonds with the compressed chain atoms. These results clearly indicate that the bending of the 3-atom chain is the main starting event that leads to amorphization. Amorphization in the two  $B_4C$  models shows some discernable differences. Amorphization in the  $B_{11}C-CBC$  model is abrupt and no short range order remains whereas in the  $B_{12}-CCC$  model, it appears that some short range order remain even after amorphization, mostly in the formation of local triangular C units. This fact could partially rationalize the notion of aggregation of some short ranged

structures of B and C atoms in amorphized  $B_4C$  as suggested by Fanchini et al. [138].

This large scale *ab initio* simulations provide detailed information on amorphization at the atomic scale that was missing in most previous studies. Subtle differences in the amorphization process are revealed depending on whether the  $B_4C$  structure is  $B_{11}C-CBC$  or  $B_{12}-CCC$ . In real samples, the presence of both polytypes is probable. Our calculated maximum stress that  $B_4C$  can withstand is much larger than those reported from ballistic experiments. This is because our uniaxial compression simulation is strictly along the direction of the chain which sets the upper limit for the maximum stress. If the  $B_4C$  structures are compressed in other crystallographic directions, different failure points are expected owing to the anisotropic crystal structure. On the other hand, the calculated  $C_{ij}$  at different strains in both models show that the structure is significantly weaker in resisting shear strains. The  $B_4C$  structure may collapse under a shearing stress that is much less than uniaxial stress.

The real  $B_4C$  materials used for armor protection and subject to ballistic impact tests are either polycrystals or composites. The processed samples are usually non-stoichiometric and polycrystalline and the presence of impurities, defects and microstructures such as grain boundaries or dislocations is the norm. The failure mechanism in the real samples will be far more complex. There are many other factors in actual experiments such as impact contact area, impact duration, impact velocity, impact orientation and other unaccounted factors in the actual ballistic experiments that may cause the shear stress to reach a sufficiently high level that could result in localized amorphization within certain regions as observed experimentally. Our simulation on the idealized models provides the necessary insights in understanding such failure and set the upper limits for the failure strain. It is desirable to conduct the same uniaxial compression simulation with even larger supercells of more than 180 atoms which can reduce the constraints imposed by the

periodic boundary condition and more closely approach the characteristic length scale of the amorphous material. Similar simulations on much larger models containing different kind of imperfections or on composites materials with other ceramics such as SiC can be used to help identify promising ingredients and processing conditions for the production of armor materials with superior properties.

## CHAPTER 7

### FUTURE WORKS

This dissertation work is an extensive use of DFT method for solving different type of problems in different materials, mullite, iota-alumina and boron carbide. In each case, the problems undertaken were different so it shows a strength of modern DFT codes along with modern computing facilities.

Most of the calculations presented in this dissertation are ground state properties of materials. These calculations help to understand material properties in fundamental level. Materials in general are used in higher temperature and pressure conditions. So, calculations of high temperature and pressure properties of materials are very important in order to advance materials for their potential application. For example, mullite is refractory material and is used in high temperature environment. The importance of mullite rests on its outstanding properties such as low thermal expansion and electric conductivity, high temperature strength, thermal shock resistance and so on. A wide application of mullite, as the monolithic ceramics and also mullite coatings, and mullite matrix composites, is in high temperature conditions such as high temperature furnace window, heat shield of space re-entry vehicles, various parts in gas turbine engines etcetera. All these and many other potential applications of mullite can be better understood through the temperature-pressure dependent elastic properties. So, one of the most important and also challenging works that could be done is calculation of temperature and pressure dependent elastic constants.

Present method which is used to calculate ground state elastic tensor can be easily extended for pressure dependent elastic tensor using hydrostatic compression in the structure and also in uniaxially stressed structure as done in boron carbide in its simulation for

failure mechanism. But to extend it to the temperature dependent elastic tensor is rather complicated. In order to get temperature dependent elastic tensor one need to use phonon calculations of the structures with different volumes (hydrostatic compressions and expansions from equilibrium volume) and also calculations with different strains depending upon the symmetry of the crystal. This is computationally very expensive but the importance of results outweighs the cost.

The temperature dependent elastic tensor is also very important in many other material systems. One of the systems electronic structure group (ESG) in UMKC is involved is MAX phases. The layered, hexagonal carbides and nitrides with a general formula  $M_{n+1}AX_n$  are called MAX phases, where  $M$  is early transition metal,  $A$  is group A elements, and  $X$  is C and/or N with  $n$  varying from 1 to 3. The MAX phases are promising materials for high temperature applications. For example, MAX phases can be used as refractory materials and corrosion resistance materials at high temperature.

Mullite can incorporate a number of foreign cations. The amount of foreign ions in mullite depends upon the nature of ions and temperature. In case of transition metal ions, the radii and oxidation states of ions are important in deciding the amount of impurities. There is alot of room to explore how the controlled amount of impurity ions in mullite models affect its electronic, elastic and thermodynamic properties.

One key question that is not clear in this *ab initio* simulation of failure mechanism of boron carbide is whether the amorphisation is localized or not. In order to address this question the model should be large enough, perhaps much larger than current model, so that the model has plenty of room for isolated amorphous zones can be created. While in real high velocity impact, the impact effect transmits very fast and could be very dramatic. Using different rate of change of strains could lead to different mechanism of amorphisation.

The *ab initio* simulation on boron carbide is only along the crystallographic c-axis, which is only a case of many possibilities. This can be extended for other directions and also using shear strains which could elaborate the effect of the impact angle. Further, extending compression simulation along many directions, a three dimensional failure envelope can be constructed.

## APPENDIX

Input files required to run VASP.

There are four files that are required to run a job within VASP. These four files are INCAR, KPOINTS, POSCAR, and POTCAR. The POTCAR file contains pseudo-potentials of each species of atoms in the structure. It is a large file so is not included here.

The INCAR file is the most important file which tells what and how to calculate. It consists of large number of parameters and it is always challenging to choose them rightly and in right combination. Many of them carry a convenient default values so for most of the calculations, only a few of them in INCAR file should be enough.

### **INCAR file.**

System = Sillimanite

ISMEAR = -5 ! Use 0 for KPOINTS less than 4 otherwise -5, 1 for metals.

PREC = Accurate ! low, normal are other options. Use suitable one.

ENCUT = 700 eV ! Decide considering the crystal size and accuracy you want.

EDIFF =  $1.0E^{-7}$  ! Energy difference convergence limit for electronic optimization

EDIFFG =  $-1.0E^{-5}$  ! Energy difference convergence limit for ionic optimization.

IBRION = 2 ! 0 for MD, 1 or 2 for relaxation.

NSW = 300 ! Total number of ionic steps.

ISIF = 3 ! 2 and 4 ionic, 7 volume and 3 both.

LREAL = Auto ! use FALSE for reciprocal space projection.

NPAR = 2 ! Best  $\sqrt{NCPUs}$ . maintain  $\geq NCPUs/32$ .

ALGO = Fast ! default is Normal.

LCHARG = .FALSE. ! No writing in CHG and CHARGCR files.

LWAVE = .FALSE. ! No writing in WAVECAR file.

The KPOINTS file represents the number of k-points to be used in calculations. There are a number of ways to specify k-points in KPOINTS file. One of the simplest one is gamma-centered mesh as shown below.

### **KPOINTS** file

Automatic generation

```
0          ! 0 means automatic generation scheme.
G          ! G means gamma centered grid
4 4 6     !Subdivisions along the reciprocal lattice vectors.
0 0 0     ! Optional shift of the mesh.
```

The following is the POSCAR file of Sillimanite used in VASP calculations. The first line in the POSCAR file is system name. Second line represents scaling factor of the lattice vectors. The next three lines represent lattice vectors of the structure. The sixth line is symbols of atomic species and their order should be as in POTCAR file. The seventh line represents number of atoms according to atomic species in the structure. In this case, there are 8 Al, 4 Si, and 20 O atoms. The eighth line tells about the type of atomic coordinates, fractional or cartesian coordinates. Here Direct means fractional coordinates. All the rest of line are fractional coordinates of atomic positions in the sillimanite. Among them first eight are for Al atoms, then the next 4 are for Si atoms and the rest are for 20 O atoms.

### **POSCAR** file of Sillimanite

```
System Al8Si4O20
1.0000000000000000
7.4436075740405840 0.0000000000000000 0.0000000000000000
0.0000000000000000 7.6035320280873320 0.0000000000000000
```

0.0000000000000000 0.0000000000000000 5.7486089785349050

Al Si O

8 4 20

Direct

0.0000000000000000	0.0000000000000000	0.0000000000000000
0.5000000000000000	0.5000000000000000	0.0000000000000000
0.5000000000000000	0.5000000000000000	0.5000000000000000
0.0000000000000000	0.0000000000000000	0.5000000000000000
0.1413595746357255	0.3424982194436339	0.2500000000000000
0.6413595746357186	0.1575017805563664	0.7500000000000000
0.3586404253642745	0.8424982194436410	0.2500000000000000
0.8586404253642814	0.6575017805563590	0.7500000000000000
0.1545523575028120	0.3392676060291088	0.7500000000000000
0.6545523575028047	0.1607323939708912	0.2500000000000000
0.3454476424971878	0.8392676060291090	0.7500000000000000
0.8454476424971953	0.6607323939708910	0.2500000000000000
0.3627561323734391	0.4068598658631540	0.7500000000000000
0.8627561323734325	0.0931401341368530	0.2500000000000000
0.1372438676265678	0.9068598658631469	0.7500000000000000
0.6372438676265675	0.5931401341368531	0.2500000000000000
0.3562928631460178	0.4328506338115053	0.2500000000000000
0.8562928631460249	0.0671493661884947	0.7500000000000000
0.1437071368539822	0.9328506338115055	0.2500000000000000
0.6437071368539751	0.5671493661884945	0.7500000000000000
0.4749997466506606	0.0033420703209311	0.7500000000000000
0.9749997466506750	0.4966579296790690	0.2500000000000000
0.0250002533493393	0.5033420703209384	0.7500000000000000
0.5250002533493250	0.9966579296790616	0.2500000000000000
0.1263333933259156	0.2203000758503422	0.5147707702523860
0.6263333933259225	0.2796999241496578	0.4852292297476067
0.3736666066740845	0.7203000758503494	0.9852292297476140
0.8736666066740775	0.7796999241496506	0.0147707702523933
0.8736666066740775	0.7796999241496506	0.4852292297476067
0.3736666066740845	0.7203000758503494	0.5147707702523860
0.6263333933259225	0.2796999241496578	0.0147707702523933
0.1263333933259156	0.2203000758503422	0.9852292297476140

## BIBLIOGRAPHY

- [1] G. Kresse and J. Hafner, “*Ab initio* Molecular Dynamics for Liquid Metals,” *Phys. Rev. B* 47, 558-561 (1993).
- [2] G. Kresse and J. Furthmüller, “Efficiency of *ab initio* Total Energy Calculations for Metals and Semiconductors Using a Plane-Wave Basis Set,” *Comput. Mater. Sci.* 6, 15 (1996).
- [3] G. Kresse and J. Furthmüller, “Efficient Iterative Schemes for *ab initio* Total-Energy Calculations Using a Plane-Wave Basis Set,” *Phys. Rev. B* 54, 11169-11186 (1996).
- [4] W.Y. Ching “Theoretical Studies of the Electronic Properties of Ceramic Materials,” *J. Am. Ceram. Soc.*, 73, 3135-59 (1990).
- [5] P.A. Foster, “Nature of Alumina in Quenched Cryolite-Alumina Melts,” *J. Electrochem. Soc.*, 106, 971-975 (1959).
- [6] P. H. DuVigneaud, “Existence of Mullite Without Silica,” *J. Am. Ceram. Soc.*, 57 [5], 224 (1974).
- [7] A.J. Perrota and J.E. Young, Jr, “Silica-Free Phase with Mullite-Type Structures,” *J. Am. Ceram. Soc.*, 57[9], 406-407 (1974).
- [8] F. Thevenot, “Boron Carbide - a Comprehensive Review,” *J. Eur. Ceram. Soc.* 6, 205 (1990).
- [9] L. H. Thomas, “The Calculation of Atomic Fields,” *Proc. Cambridge Phil. Soc.* 23 (5), 542-548 (1927).
- [10] E. Fermi, “Un Metodo Statistico per la Determinazione di alcune Proprieta dell’ Atomo,” *Rend. Accad. Naz. Lincei* 6, 602-607 (1927).

- [11] D. R. Hartree, Proc. Camb. Philos. Soc. 24, 89, 111 (1928); D. R. Hartree, The Calculation of Atomic Structure (Wiley Interscience, New York, 1957).
- [12] V. A. Fock, Z. Phys. 61, 126 (1930).
- [13] C. Moller and M. S. Plesset, "Note on an Approximation Treatment from Many-Electron System" Physical Review 46 (7), 618-622 (1934).
- [14] D. Maurice, and M. H. Gordon, "Analytical Second Derivative for Excited Electronic States Using the Single Excitation Configuration Interaction Method: Theory and Application to Benzopyrene and Chalcone", Molecular Physics 96 (10) (1999).
- [15] T. V. Voorhis, and M. H. Gordon, "Two-body Coupled Cluster Expansion", J. Chem. Phys. 115 (11), 5033-5041 (2001).
- [16] P. Hohenberg and W. Kohn, "Inhomogeneous Electron Gas," Phys. Rev., Vol. 136, B864-B871 (1964).
- [17] W. Kohn and L. J. Sham, "Self-consistent Equations Including Exchange and Correlation Effects," Phys. Rev., Vol. 140, A1133-A1138 (1965).
- [18] K. Capelle, "A Bird's-Eye View of Density-Functional Theory," Brazilian Journal of Physics 36 [4A], 1318 (2006).
- [19] J. P. Perdew, and Y. Wang, "Accurate and Simple Density Functional for the Electronic Exchange Energy: Generalized Gradient Approximation," Phys. Rev. B 33, 8800 (1986).
- [20] J. P. Perdew, K. Burke, and M. Ernzerhof, "Generalized Gradient Approximation Made Simple," Phys. Rev. Lett. 77, 3865 (1996).
- [21] A. D. Becke, "Density-Functional Exchange-Energy Approximation with Correct Asymptotic Behavior," Phys. Rev. A. 38, 3098 (1988).

- [22] C. Lee, W. Yang, and R. G. Parr, "Development of the Colle-Salvetti Correlation-Energy Formula into a Functional of the Electron density," *Phys. Rev. B* 37, 785 (1988).
- [23] W.Y. Ching, and P. Rulis, "Ab-initio Calculation of the Electronic and Spectroscopic Properties of Spinel  $\gamma$ - $Sn_3N_4$ ," *Phys. Rev. B*, 73, 045202-1-9 (2006).
- [24] P. Rulis, H. Yao, L. Ouyang, and W. Y. Ching, "Electronic Structure, Bonding, Charge Distribution and X-ray Absorption Spectra of the (001) Surfaces of Fluorapatite and Hydroxyapatite," *Physical Review B* 76, 245410-1-15 (2007).
- [25] W. Y. Ching, L. Ouyang, P. Rulis, and H. Yao, "Ab initio Study of the Physical Properties of  $\gamma$ - $Al_2O_3$ : Lattice Dynamics, Bulk Properties, Electronic Structures and Bonding, Optical Properties and ELNES/XANES Spectra," *Phys. Rev. B* 78, 014106-1-13 (2008).
- [26] J. Chen, L. Ouyang, P. Rulis, A. Misra, and W. Y. Ching, "Complex Nonlinear Deformation of a Nanometer Intergranular Glassy Films in Silicon Nitride Ceramics," *Phys Rev Lett* 95, 256103-106 (2005).
- [27] W. Y. Ching, P. Rulis, L. Ouyang, and A. Misra, "Ab initio Tensile Experiment on a Model of Intergranular Glassy Film in  $\beta$ - $Si_3N_4$  with Prismatic Surfaces," *Appl. Phys. Lett.* 94, 051907-1-3 (2009).
- [28] Lei Liang, Paul Rulis and W.Y. Ching. "Mechanical Properties, Electronic Structure and Bonding of  $\alpha$ - and  $\beta$ -tri-calcium Phosphates with Surface Characterization," *Acta Biomaterialia*, 6, 3763-3771 (2010).
- [29] W.Y. Ching, Paul Rulis, Lizhi Ouyang, S. Aryal, and Anil Misra. "Theoretical Study of the Elasticity, Mechanical Behavior, Electronic Structure, Interatomic Bonding, and Dielectric Function of an Intergranular Glassy Film Model in Prismatic  $\beta$ - $Si_3N_4$ ," *Phys. Rev. B* 81, 214120-1-14. (2010).

- [30] Lei Liang, Paul Rulis, L. Ouyang, and W.Y. Ching, “*Ab initio* Investigation of Hydrogen Bonding and Network Structure in a Supercooled Model of Water,” *Phys. Rev. B* 83, 024201-1-7 (2011).
- [31] W.Y. Ching, S. Aryal, Paul Rulis, Wolfgang Schnick, “Prediction of the Electronic Structure and Physical Properties of the Spinel Phase of  $BeP_2N_4$ ,” *Phys. Rev. B* 83, 155109-1-8 (2011).
- [32] D. Vanderbilt, “Soft Self-Consistent Pseudopotential in a generalized Eigenvalue Formalism,” *Phys. Rev. B* 41, 7892 (1990).
- [33] G. Kresse and J. Hafner, “Norm-Conserving and Ultrasoft Pseudopotential for First-row and Transition-Elements,” *J. Phys.: Condens. Matter*, 6, 8245 (1994).
- [34] P.E. Blchl, “Projector Augmented-Wave Method,” *Phys. Rev. B* 50, 17953-17979 (1994).
- [35] G. Kresse, and J. Joubert, “From Ultrasoft Pseudopotentials to the Projector Augmented Wave Method,” *Phys. Rev. B* 59, 1758-1775 (1999).
- [36] Wai-Yim Ching, and Paul Rulis, “Electronic Structure Methods for Complex Materials: The Orthogonalized Linear Combination of Atomic Orbitals,” Oxford University Press. 2012.
- [37] C. Herring, “A New method for Calculating Wave Functions in Crystals,” *Phys. Rev.* 57, 1169-1177 (1940).
- [38] R.S. Mulliken, “Electronic Population Analysis on LCAO-MO Molecular Wave Functions. I,” *J. of Chem. Phys.* 23, 1833, (1955); *ibid* 23, 1841, (1955).
- [39] D. Greenwood, in *Proc. Phys. Soc., London*, Vol. 71, p. 585 (1958).
- [40] O. H. Nielsen and R. M. Martin, “First-Principles Calculation of Stress,” *Phys. Rev. Lett.* 50, 697 (1983).
- [41] W. Voigt, *Lehrbuch der Kristallphysik*. Teubner, Leipzig und Berlin, (1928).

- [42] A. Reuss, "Berchung der Fiessgrenze von Mischkristallen auf Grund der Plastizitätsbedingung fr Einkristalle, Z. Angew. Math. Mech., 9[1] 49-58 (1929).
- [43] R. Hill, "The Elastic Behavior of a Crystalline Aggregate, Proc. Phys. Soc. A 65, 349 (1952).
- [44] S. Baroni, P. Giannozzi, and A. Testa, "Green's-Function Approach to Linear Response in Solids," Phys. Rev. Lett. 58, 1861 (1987).
- [45] P. Giannozzi et al., URL: <http://www.quantum-espresso.org>.
- [46] S. Baroni, S. de Gironcoli, A. Dal Corso, and P. Giannozzi, "Phonons and Related Crystal Properties from Density-Functional Perturbation Theory," Rev. Mod. phys. 73, 515-562 (2001).
- [47] H. Schneider and Weinheim S. Komarneni (Eds.) Mullite. WILEY-VCH Verlag GmbH & Co. KGaA. 2005.
- [48] M. Martinn-Torres, T. Rohren and I.C. Freestons, "Mullite and the mystery of Hessian wares," Nature (London) 444, 437-438 (2006).
- [49] I. A. Aksay, D. M. Dabbs, and M. Sarikaya, "Mullite for Structural, Electronic, and Optical Application," J. Am. Ceram. Soc., 74 (10) 2343-58 (1991).
- [50] W.E. Cameron, "Mullite: A substituted alumina," American Mineralogist, 62, 747-755 (1977).
- [51] C. W. Burnham, "Composition Lmitis of Mullite and the Sillimanite-mullite Solid Solution Problem," Carnegie Inst., Washington, Year Book., 63, 223-227 (1964).
- [52] R. X. Fischer, H. Schneider, and D. Voll, "Formation of Aluminum Rich 9:1 Mullite and Its Transformation to Low Alumina Mullite upon Heating," J. Eur. Ceram. Soc., 16, 109-113 (1996).
- [53] N.L. Bowen, and J. W. Creig, "The system  $Al_2O_3-SiO_2$ ," J. Amer. Ceram. Soc., 7 (4) 238-254 (1924).

- [54] H. Yang, R.M. Hazen, L.W. Finger, C.T. Prewitt, and R.T. Downs, "Compressibility and crystal structure of sillimanite  $Al_2SiO_5$  at high pressure," *Phys. and Chem. of Minerals*, 25, 39-47 (1997).
- [55] H. Schneider, J. Schreuer, and B. Hildmann, "Structure and Properties of Mullite-A Review," *J. Europ. Ceram. Soc.* 28, 329-344 (2008).
- [56] L. A. Xue, I.-W. Chen, "Fabrication of Mullite Body Using Superplastic Transient Phase," *J. Am. Ceram. Soc.*, 75 [5] 1085-91 (1992).
- [57] D.R. Treadwell, D.M. Dabbs, and I.A. Aksay, "Mullite ( $3Al_2O_3-2SiO_2$ ) Synthesis with Aluminosiloxanes," *Chem. Mater.* 8, 2056-2060 (1996).
- [58] A. Caballero and M. Ocana, "Synthesis and Structural Characterization by X-ray Absorption Spectroscopy on Tin-doped Mullite Solid Solutions," *J. Am. Ceram. Soc.*, 85 [8] 1910-14 (1992).
- [59] Y. J. Chen, B. Chi, Q.X. Liu, D. C. Mahon, and Y. Chen, "Synthesis and Optical Properties of Mullite ( $Al_{5.65}Si_{0.35}O_{9.175}$ ) Nanowires," *IEEE, ICONN* 134-137 (2006).
- [60] R. Sadanaga, M. Tokonami, and Y. Takruchi, "The Structure of Mullite,  $2Al_2O_3 \bullet SiO_2$  and Relationship with the Structures of Sillimanite and Andalusite," *Acta Cryst.* 15, 65-68 (1962).
- [61] R. J. Angel and C.T. Prewitt, "Crystal Structure of Mullite: A Re-examination of the Average Structure," *American Mineralogist*, 71, 1476-1482 (1986).
- [62] M. I. Osendi, B. A. Bender, and D. Lewis, "Microstructure and Mechanical Properties of Mullite-Silicon Carbide Composites," *J. Am. Ceram. Soc.*, 72 [6] 1049-54 (1989).
- [63] H. Schneider and E. Eberhard, "Thermal Expansion of Mullite" , *J. Am. Ceram. Soc.*, 73 [7] 2073-76 (1990).

- [64] D. Sanyal, D. Banerjee, R. Bhattacharya, S. K. Patra, S. P. Chaudhari, B. N. Ganguly, and U. De, "Study of Transition Metal Ion Doped Mullite by Positron Annihilation Technique," *J. Materials Sci.* 31, 3447-3451 (1996).
- [65] P. Rehak, G. Kunath-Fandrei, P. Losso, B. Hildmann, H. Schneider, and C. Jager, "Study of the Al Coordination in Mullites with Varying Al:Si Ratio by  $^{27}\text{Al}$  NMR Spectroscopy and X-ray Diffraction," *American Mineralogist* 83, 1266-1276 (1998).
- [66] W. M. Kriven, J. W. Palko, S. Sinogeikin, J. D. Bass, A. Sayir, G. Brunauer, H. Boysen, F. Frey, and J. Schneider, "High Temperature Single Crystal Properties of Mullite," *J. Euro. Ceram. Soc.* 19, 2529-2541 (1999).
- [67] M. Schmcker, H. Schneider, K.J. D. MacKenzie, M.E. Smith and D.L. Carroll, " $\text{AlO}_4/\text{SiO}_4$  distribution in Tetrahedral Double Chains of Mullite," *J. Am. Ceram. Soc.*, 88 [10], 2935-37 (2005).
- [68] R. A. Penty, D. P. H. Hasselman, and R. M. Spriggs, "Young's Modulus of High-Density Polycrystalline Mullite," *J. Am. Ceram. Soc.*, 55 [3] 169-70 (1972).
- [69] M. G. M. U. Ismail, Z. Nakai, and S. Somiya, "Microstructure and Mechanical properties of Mullite Prepared by the Sol-Gel Method," *J. Am. Ceram. Soc.*, 70 [1] C-7 - C-8 (1987).
- [70] M. I. Osendi and C. Baudin, "Mechanical Properties of Mullite Materials," *J. Europ. Ceram. Soc.*, 16, 217-224 (1996).
- [71] N. Kawai, K. G. Nakamura, and K.-I. Kondo, "High-pressure Phases Transition of Mullite under Shock Compression," *J. Appl. Phys.* 96, 4126-4130 (2004).
- [72] B. Hildman and H. Schneider, "Thermal Conductivity of 2/1 Mullite Single Crystals," *J. Am. Ceram. Soc.*, 88 [10], 2879-82 (2005).
- [73] R. A. Howald, and I. Ellezer, "Thermodynamic Properties of Mullite," *J. Phys. Chem.* 82 (20) 2199-2204 (1978).

- [74] J. E. Fenstermacher and F. A. Hummel, "High-Temperature Mechanical Properties of Ceramic Materials: IV, Sintered Mullite Bodies," *J. Am. Ceram. Soc.*, 44 [6] 284-89 (1961).
- [75] J. B. Wachtman and D. G. Lam, "Youngs Modulus of Various Refractory Materials as a Function of Temperature," *J. Am. Ceram. Soc.*, 42[5] 254-60 (1959).
- [76] P.C. Dokko, J.A. Pask, and K.S. Mazdiyasi, "High-Temperature Mechanical Properties of Mullite Under Compression," *J. Am. Ceram. Soc.*, 60[3-4] 150-155 (1976).
- [77] P. Descamps, S. Sakaguchi, M. Poorteman, and F. Comabier, "High-Temperature Characterization of Reaction-Sintered Mullite-Zirconia Composites," *J. Am. Ceram. Soc.*, 74 (10) 2476-81 (1991).
- [78] B. Hildmann, H. Ledbetter, S. Kim and H. Schneider, "Structural Control of Elastic Constants of Mullite in Comparison to Sillimanite," *J. Am. Ceram. Soc.* 84, 24092414 (2001).
- [79] J.W. Palko, A. Sayir, S.V. Sinogeikin, W.M. Kriven and J.D. Bass, "Complete Elastic Tensor for Mullite ( $2.5Al_2O_3 \bullet SiO_2$ ) to High Temperatures Measured from Textured Fibers," *J. Am. Ceram. Soc.* 85, 20052012 (2002).
- [80] H. Ledbetter, S. Kim, D. Balzer, S. Crudele, and W. Kriven, "Elastic Properties of Mullite," *J. Am. Ceram. Soc.* 81 [4], 1025-28, (1998).
- [81] J. Schreuer, B. Hildman, and H. Schneider, "Elastic Properties of Mullite Single Crystals up to 1400°C," *J. Am. Ceram. Soc.* 89 [5], 1624-1631, (2006).
- [82] J. F. Wygant, "Elastic and Flow Properties of Dense, Pure Oxide Refractories," *J. Am. Ceram. Soc.*, 34 [12] 374-80 (1951).
- [83] M. Schmcker, H. Schneider, and W. M. Kriven, "Indentation-Induced Amorphization in Mullite Single Crystal," *J. Am. Ceram. Soc.*, 86[10] 1821-22 (2003).

- [84] D. Voll, C. Lengauer, A. Beran, H. H. Schneider, "Infrared Band Assignment and Structural Refinement of Al-Si, Al-Ge, and Ge-Ge Mullites," *Euro. J. Mineral.* 13, 591-604 (2001).
- [85] H. K. Seong, U. Kim, M. Kim, and H. Choi, "Synthesis and Optical Properties of Mullite Nanowires," *J. Am. Ceram. Soc.*, 90 (6) 1937-1939 (2007).
- [86] W. H. Kelly, A. N. Palazotto, R. Ruh, J. K. Heuer, and A. Zangvil, "Thermal Shock Resistance of Mullite and Mullite- $ZrO_2$ - $SiC$  Whisker Composites," *Ceram. Eng. Sci. Proc.*, 18 [3] 195-203 (1997).
- [87] S. Aryal, P. Rulis and W. Y. Ching, "Density Functional Calculation of the Electronic Structure and Optical Properties of Aluminosilicate Polymorph ( $Al_2SiO_5$ )," *American Mineralogist*, 93, 114-123 (2008).
- [88] J.-C. Chen, C. S. Chen, H. Schneider, C.C. Chou, and W.-C. J. Wei, "Atomistic Calculations of Lattice Constants of Mullite with Its Compositions," *J. of the European Ceramic Society*, 28, 345-351 (2008).
- [89] D. Balzar, and H. Ledbetter, "Crystal Structure and Compressibility of 3:2 Mullite," *American Mineralogist* 78, 1192-1196 (1993).
- [90] R. J. Angel, R. K. McMullan, and C. T. Prewitt, "Substructure and Superstructure of Mullite by Neutron Diffraction," *American mineralogist* 76, 332-342 (1991).
- [91] R. X. Fischer, H. Schneider, and M. Schmucker, "Crystal Structure of Al-rich Mullite," *American Mineralogist* 79, 983-990 (1994).
- [92] H. Saalfeld; pp. 71-74 in *Transactions of the VIIIth International Ceramic Congress, Copenhagen, 1962. The Organizing Committee of the VIIIth International Ceramic Congress, Copenhagen, (1962).*

- [93] J.D. Bass, V. S. V. Sinogeikin, and B. Li, "Elastic Properties of Materials: A Key for Understanding the Composition and Temperature of Earth's Interior," *ELEMENTS*, 4, 165-170 (2008).
- [94] L. D. Landau and E.M. Lifshitz, *Theory of Elasticity*; pp104. Pergamon Press, London, U.K. (1954); Robert E. Newnham, *Properties of Materials, Anisotropy, Symmetry, Structure*. (Oxford University Press, Oxford, (2005).
- [95] J.A. Hudson, "Wave Speeds and Attenuation of Elastic Waves in Material Containing Cracks," *Geophys. J. Royal Astr. Soc.*, 64, 133-150 (1981).
- [96] Wai-Yim Ching and Paul Rulis, *Electronic Structure Methods for Complex Materials: The Orthogonalized Linear Combination of Atomic Orbitals*, Oxford University Press, Oxford (2012).
- [97] W.E. Tröger, *Optische Bestimmung der gesteinsbildenden Minerale. Teil 1: Bestimmungstabellen*, 5 Aufl. Schweizerbarth, Stuttgart (1982).
- [98] C. Klein and C.S. Hurlbut, jr. in *Manual of Mineralogy*, 20th Edition, Wiley, Inc, New York. (1993).
- [99] A.J. Wojtowicz, W. Meng, A. Lempicki, G. H. Beall, D.W. Hall, and T. C. Chin, "Spectroscopic Characteristics of Chromium Doped Mullite Glass-ceramics," *IEEE J. Quantum Electronics*, 24 [6] 1109-1113 (1988).
- [100] S. Prochazka and F.J. Klug, "Infrared-transparent Mullite Ceramic," *J. Am. Ceram. Soc.*, 66 [12], 874-880 (1983).
- [101] H. Saalfeld and H. Gerlach, "Solid Solution and Optical Properties of (Al, Ge)-Mullites," *Zeitschrift für Kristallographie* 195, 65-73 (1991).
- [102] S. Aryal, Paul Rulis and W.Y. Ching. "Mechanism for Amorphization in Boron Carbide  $B_4C$  Under Uniaxial Compression," *Phys. Rev. B* 84, 184112-1-12. (2011).

- [103] M. Korenko, M. Kucharik, and D. Janickovic, "Rapid Solidification Processing in Molten Salts Chemistry: X-ray Analysis of Deeply Undercooled Cryolite-Alumina Melts," *Chemical papers* 62 (2), 219-222 (2008).
- [104] T. Ebadzadeh, and L. Sharifi, "Synthesis of  $\iota$ - $Al_2O_3$  from a Mixture of Aluminum Nitrate and Carboxymethyl Cellulose," *J. Am. Ceram. Soc.*, 91 (10), 3408-3409 (2008).
- [105] R.X. Fischer and H. Schneider, "The Mullite-Type Family of Crystal Structures," In: H. Schneider and S. Komarneni, Editors, *Mullite*, Wiley-VCH, Weinheim pp. 146.
- [106] P. Lamparter, and R. Kniep, Structure of Amorphous  $Al_2O_3$ , *Physica B* 234, 405-406 (1997).
- [107] G. Gutierrez and B. Johanson, Molecular Dynamics Study of Structural Properties of Amorphous  $Al_2O_3$ , *Phys. Rev. B* 65, 104202 (2002).
- [108] R. Lizarraga, E. Holmstrom, S. C. Parker, and C. Arrouvel, Structural Characterization of Amorphous Alumina and its Polymorphs from First-Principles XPS and NMR calculations, *Phys. Rev. B* 83, 094201 (2011).
- [109] Werner Kraus and Gert Nolze, "Powder Cell 2.3 for Windows" Accessed at (2011). URL: [http://www.ccp14.ac.uk/ccp/web-mirrors/powdcell/a\\_v/v\\_1/powder/e\\_cell.html](http://www.ccp14.ac.uk/ccp/web-mirrors/powdcell/a_v/v_1/powder/e_cell.html).
- [110] K. Wefers, and C. Misra, "Oxides and Hydroxides of Aluminum," ALCOA technical paper No. 19 (revised), Alcoa Laboratory, Pittsburgh (1987).
- [111] W. Voigt, *Lehrbuch der Kristallphysik*. Taubner, Leipzig, (1928).
- [112] S. F. Pugh, "Relations between the Elastic Moduli and the Plastic Properties of Polycrystalline Pure metal," *Phil. Mag.* 45, 823 (1954).

- [113] W. Y. Ching and Y-N Xu, "First-Principles Calculation of Electronic, Optical, and Structural Properties of  $\alpha$ - $Al_2O_3$ ", J. Am. Ceram. Soc. 77, 404-411 (1994).
- [114] Shang-Di Mo and W.Y. Ching, "Electronic and Optical Properties of  $\gamma$ - $Al_2O_3$  with Comparison to  $\alpha$ - $Al_2O_3$ ," Phys. Rev. B 57, 15219-28 (1998).
- [115] Y. N. Xu and W. Y. Ching, "Self-Consistent Band Structures, Charge Distributions, and Optical-Absorption Spectra in  $MgO$ ,  $\alpha$ - $Al_2O_3$ , and  $MgAl_2O_4$ ," Phys. Rev. B 43, 4461 (1991).
- [116] Shang-Di Mo, and W. Y. Ching, "*Ab initio* Calculation of the Core-Hole Effect in the Electron Energy-Loss Near-Edge Structure," Phys. Rev. B 62, 7901 (2000).
- [117] W.Y. Ching, P. Rulis, A. Misra. "*Ab initio* Elastic Properties and Tensile Strength of Crystalline Hydroxyapatite," Acta Biomaterial. 5, 3067-3075 (2009).
- [118] W.-Y. Ching, S.-D. Mo, and Y. Chen, "Calculation of XANES/ELNES Spectra of All Edges in  $Si_3N_4$  and  $Si_2N_2O$ , J. Am. Ceram. Soc. 85, 11 (2002).
- [119] T. Mizoguchi, I. Tanaka, S. Yoshioka, M. Kunisu, T. Yamamoto, and W. Y. Ching, Phys. Rev. B 70, 045103 (2004).
- [120] W.Y. Ching, and P. Rulis, "*Ab initio* Calculation of the O-K, N-K, Si-K, Si-L3, Y-K, Y-L3 Edges in the Y-Si-O-N System: A New Strategy for ELNES/XANES Spectral Modeling in Complex Materials," Phys. Rev. B. 77, 035125/1-17 (2008).
- [121] Paul Rulis, Liaoyuan Wang and W.Y, Ching, "Prediction of the XANES/ELNES Spectra of  $\gamma$ - $B_{28}$  and comparison with  $\alpha$ - $B_{12}$ ," Phys. Status Solidi RRL 3, 133-135 (2009).
- [122] A. Altay, C.B. Carter, P. Rulis, W.Y. Ching, I. Arslan and M.A. Glgun, "Characterizing CA2 and CA6 using ELNES," J. Solid State Chem, 183(8) ,1776-1784 (2010).

- [123] Paul Rulis and W.Y. Ching, "Theoretical XANES Spectra of Si-K, Si-L, N-K and O-K Edges of a Prismatic Model of Intergranular Glassy Films in  $\beta$ - $Si_3N_4$ ," J. of Materials Science, 46 (12), 4191-4198 (2011).
- [124] I. Tanaka, T. Mizoguchi, M. Matsui, S. Yoshioka, H. Adachi, T. Yamamoto, T. Okajima, M. Umesaki, W. Y. Ching, Y. Inoue, M. Mizuno, H. Araki and Y. Shirai. "Identification of Ultradilute Dopants in Ceramics". Nature Materials 2, [8] 541-545 (2003).
- [125] P. Rulis, W. Y. Ching, and M. Kohyama, "Ab initio ELNES/XANES Spectral Calculation of Polar and Non-polar Grain Boundaries in  $\beta$ - $SiC$ ," Acta Materialia 52, 3009 (2004).
- [126] D. Emin, T. Aselage, A. C. Switendick, B. Morosin, and C. L. Beckel. AIP Conference Proceedings 231. Boron-rich Solids. Albuquerque, New Mexico p195 (1990).
- [127] R. Lazzari, N. Vast, J. M. Besson, S. Baroni, and A. Dal Corso, "Atomic Structure and Vibrational properties of Icosahedral  $B_4C$  Boron Carbide," Phys. Rev. Lett. 8, 3(16), 3230 (1999).
- [128] J. E. Saal, S. Shang, and Z.-K. Liu, "The Structural Evaluation of Boron Carbide Via *ab initio* Calculations," Appl. Phys. Lett., 91, 2319115 (2007).
- [129] D. E. Grady, Dynamic properties of Ceramic Materials: Sandia National Laboratories Report, SAND 94-3266 (Sandia National Laboratories, Albuquerque, NM) (1995).
- [130] M. W. Chen, J. W. McCauley, and K. J. Hemker, " Shock-Induced Localized Amorphization in Boron Carbide," Science 299, 1563 (2003).
- [131] D. P. Dandekar, Army Research Laboratory, Aberdeen Proving, Aberdeen, MD, ARL-TR-2456 (2001).

- [132] T. J. Volgler, W. D. Reinhart, and L. C. Chhabildas, "Dynamic Behavior of Boron Carbide," *J. Appl. Phys.* 95, 4273 (2004).
- [133] V. Domnich, Y. Gogotsi, M. Trenary, and T. Tanaka, "Nanoindentation Spectroscopy Studies of Boron Carbide Single Crystal," *Appl. Phys. Lett.* 81 (20), 3783 (2002).
- [134] D. Ge, V. Domnich, T. Juliano, E. A. Stach, and Y. Gogotsi, "Structural Damage in Boron Carbide under Contact Loading," *Acta Materialia*, 52, 3921-3927 (2004).
- [135] D. Ghose, G. Subahash, C. H. Lee, and Y. K. Yap, "Strain-induced Formation of Carbon and Boron Clusters in Boron Carbide during Dynamic Indentation," *Appl. Phys. Lett.* 91, 061910 (2007).
- [136] G. Fanchini, V. Gupta, A. B. Mann, and M. Chhowalla, "In Situ Monitoring of Structural Changes in Boron Carbide Under Electric Fields," *J. Am. Ceram. Soc.* 91 (8), 2666-2669 (2008).
- [137] X. Q. Yan, W. J. Li, T. Goto, and M. W. Chen, "Raman Spectroscopy of Pressure-Induced Amorphous Boron Carbide," *Appl. Phys. Lett.* 88, 131905 (2006).
- [138] G. Fanchini, J. W. McCauley, and M. Chhowalla, "Behavior of Disordered Boron Carbide Under Stress," *Phys. Rev. Lett.* 97, 035502 (2006).
- [139] R. J. Nelmes et al, *Phys. Rev. Lett.* 74, 2268 (1995).
- [140] T. J. Holmquist and G. R. Johnson, "Characterization and evaluation of Boron Carbide for Plate-Impact Condition," *J. Appl. Phys.* 100, 093525 (2006).
- [141] X. Q. yan, Z. Tang, L. Zhang, J. J. Guo, C. Q. Jin, Y. Zhang, J. W. McCauley, and M. W. Chen, "Pressurization Amorphization of Single-Crystal Boron Carbide," *Phys. Rev. Lett.* 102, 075505 (2009).
- [142] Y. Zhang et. al, "Shock Compression Behaviors of Boron Carbide," *J. Appl. Phys.* 100, 113536 (2006).

- [143] K. J. McClellan, F. Chu, J. M. Roper, and I. Shindo, "Room Temperature Single Crystal Elastic Constants of Boron Carbide," *J. of Mat. Sci.*, 36, 3403 (2001).
- [144] D. Li, W. Y. Ching, "Fundamental Studies on the Structures and Properties of Some B<sub>12</sub>-based Crystals," *Phys. Rev. B* 52, 17073 (1995).
- [145] D. M. Bylander, L. Kleinman, "Self-Consistent Calculation of the Energy Bands and Bonding Properties of B<sub>12</sub>C<sub>3</sub>," *Phys. Rev. B* 42, 1394 (1990).
- [146] D. W. Bullet, "Structure and Bonding in Crystalline Boron and B<sub>12</sub>C<sub>3</sub>," *J. Phys. C* 15, 415 (1982).
- [147] H. Werheit, M. Laux, U. Kuhlmann, R. Telle, "Optical Interband Transition of Boron Carbide," *Phys. Stat. Sol. B* 172, K81 (1992).
- [148] H. Werheit, H. W. Rotter, S. Shalamberdze, A. Leith-Jasper, and T. Tanaka, "Gap-State Related Photoluminescence in Boron Carbide," *Phys. Stat. Sol. B* 248 (5), 1275-1279 (2011).
- [149] H. Dekura, K. Shirai, and A. Yanase, "Metallicity of Boron Carbides at High Pressure," *J. of Physics: Conference Series* 215, 012117 (2010).

## VITA

Sita Ram Aryal was born on August 29, 1971 in Palpa, Nepal. He finished his schooling from local public school. Mr. Aryal studied at the Tri-Chandra Multiple Campus of Tribhuban University for his two year bachelor's degree (B.Sc.) majoring in physics. He got his master's degree (M. Sc.) in Physics from the Tribhuban University, Kathmandu, Nepal.

In August 2004, Mr. Aryal came to the United States as a graduate student in the Department of Physics at the University of Missouri - Kansas City. He got his master's degree (MS) in 2008 from the University of Missouri-Kansas City. While studying for master's degree, Mr. Aryal worked as a teaching assistant in department of physics.

Immediately after he finished his master's degree in 2008, Mr. Aryal started his interdisciplinary Ph. D. program with physics as coordinating discipline and geosciences as co-discipline.

Mr. Aryal has authored and co-authored eight scientific papers in peer reviewed journals. He has presented three posters and three talks in different conference.